Dissertation

submitted to the

Combined Faculty of Mathematics, Engineering and Natural Sciences

of Heidelberg University, Germany

for the degree of

Doctor of Natural Sciences

Put forward by
M. Sc. Marc Oliver MERSTORF
born in Göppingen, Germany
Oral examination: 28.07.2022

A spectroscopic approach to nuclear decay by electron capture

Marc Oliver Merstorf

Referees: Prof. Dr. Maurits W. Haverkort
Prof. Dr. Christian Enss

Abstract

Within this thesis, we provide a theoretical description of nuclear decay by electron capture. We discuss the influence of nuclear degrees of freedom and the coupling to the continuous spectrum of the electromagnetic field on the decay rate. Although these contributions are small, we will show that they are important for metrology and high-precision measurements. Our calculations predict that hyperfine interaction affects the decay rate on the Rydberg energy scale and changes the lifetime on the permille level. As we will show, this highly surprising result originates from selection rules related to the conservation of total angular momentum. In addition, we demonstrate that the coupling of local states to the continuous spectrum of the electromagnetic field leads to an increase of the decay rate at high energies. By direct calculations of the second-order decay rate including the decay by electron capture and subsequent fluorescence decay, we describe the process referred to as radiative electron capture. The accurate theoretical description of nuclear decay rates also requires detailed knowledge of the involved nuclear many-body wave functions. We present an iterative scheme to determine optimized single-particle states based on natural orbitals. Our developed numerical methods are applied to calculate the electron capture decay rate of several isotopes such as ^{55}Fe, ^{65}Zn, ^{71}Ge, ^{118}Te, ^{131}Cs, ^{140}Nd, ^{163}Ho and ^{165}Er.

Zusammenfassung

In dieser Arbeit liefern wir eine theoretische Beschreibung des Kernzerfalls durch Elektroneneinfang. Wir diskutieren den Einfluss der nuklearen Freiheitsgrade und die Kopplung an das kontinuierliche Spektrum des elektromagnetischen Feldes auf die Zerfallsrate. Obwohl diese Beiträge klein sind, werden wir zeigen, dass sie für die Metrologie und hochpräzise Messungen wichtig sind. Unsere Berechnungen sagen voraus, dass die Hyperfeinwechselwirkung die Zerfallsrate auf der Rydberg-Energieskala beeinflusst und zu Änderungen der Lebensdauer im Promillebereich führt. Wie wir zeigen werden, resultiert dieses höchst überraschende Ergebnis aus Auswahlregeln, die mit der Erhaltung des Gesamtdrehimpulses zusammenhängen. Darüber hinaus zeigen wir, dass die Kopplung lokaler Zustände an das kontinuierliche Spektrum des elektromagnetischen Feldes zu einer Erhöhung der Zerfallsrate bei hohen Energien führt. Durch direkte Berechnungen der Zerfallsrate zweiter Ordnung, die den Zerfall durch Elektroneneinfang und anschließenden Fluoreszenzzerfall umfasst, beschreiben wir den Prozess, der als strahlender Elektroneneinfang bezeichnet wird. Die genaue theoretische Beschreibung der nuklearen Zerfallsraten erfordert außerdem eine detaillierte Kenntnis der beteiligten nuklearen Vielteilchenwellenfunktionen. Wir stellen ein iteratives Schema zur Bestimmung optimierter Einzelteilchenzustände auf der Grundlage natürlicher Orbitale vor. Die von uns entwickelten numerischen Methoden werden zur Berechnung der Elektroneneinfang-Zerfallsrate verschiede-ner Isotope wie ^{55}Fe, ^{65}Zn, ^{71}Ge, ^{118}Te, ^{131}Cs, ^{140}Nd, ^{163}Ho und ^{165}Er angewendet.

Contents

1 Introduction

Radioactivity describes the process in which an unstable atomic nucleus, the so-called radioisotope or radionuclide, undergoes a spontaneous decay accompanied by the emission of radiation [1]. Since its discovery by Bécquerel in 1896 [2], radioactivity has been of great importance for life on earth. In fact, this is closely related to the great scientific progress, both experimental and theoretical, which has led to the application of radioactivity in various scientific and technologically highly relevant fields.

For example, radioactivity is widely used in medical applications, geology, energy production or metrology [1, 3]. In this context, detailed knowledge of the decay properties of a radionuclide is crucial for several reasons. On the one hand, to continue to benefit from their practical applications. On the other hand, to control or prevent the potential damage that the released ionizing radiation can cause. This is best illustrated by the example of radionuclides used for cancer treatment. In new treatment methods, the radionuclides are transported directly to the tumor cell. In order to minimize damage to healthy tissue, it is essential to know the exact amount of ionizing radiation released in the decay and its characteristics [4, 5].

In addition to the numerous practical applications, radioactive decays also play an outstanding role in the search of new or in the testing of established physical theories. A prominent example where the prediction of current theoretical models is wrong, concerns the neutrino. While the Standard Model of particle physics predicts the neutrino to be massless, there has been convincing experimental evidence, i.e. neutrino oscillations [6], that the neutrino's mass is finite. The neutrino is the only elementary particle whose mass is still unknown. Hence, its knowledge is of great significance for particle physics guiding to physics beyond the Standard Model [7]. Based on current estimates [8], the neutrino mass is less than 1 eV and therefore several orders of magnitude smaller than the mass of all other elementary particles. Because its mass is so small and, moreover, the neutrino interacts only via gravity and the weak force, its determination poses a big challenge. One possible, model-independent approach to determine the neutrino

mass are high-precision measurements of electron capture (EC) decay rates. A more detailed discussion on how these measurements can be used to derive the neutrino mass is given in section 1.2.

Nuclear decay by EC is a weak interacting process, in which a parent nucleus ${}^{A}_{Z}X$ absorbs a core electron while simultaneously a proton inside the nucleus is transformed into a neutron and an electron-neutrino is released

$$ {}^{A}_{Z}X + e^{-} \longrightarrow {}^{A}_{Z-1}Y^{*} + \nu_{e}. \tag{1.1} $$

After EC, the daughter atom ends up in an excited state ${}^{A}_{Z-1}Y^{*}$ which subsequently de-excites into the ground state by filling the created core hole. The total amount of energy released in the decay corresponds to the so-called Q-value, which is defined as the ground state energy difference of parent and daughter atom

$$ Q = m({}^{A}_{Z}X) - m({}^{A}_{Z-1}Y). \tag{1.2} $$

However, as the EC decay leads to the production of a neutrino, the energy released in the de-excitation process of the excited daughter atom ${}^{A}_{Z-1}Y^{*}$ does not correspond to the Q-value. Due to energy conservation, Q is shared between the energy stored in terms of electronic excitations ω and the energy taken away by the neutrino E_{ν}. Hence, only the fraction $\omega = Q - E_{\nu}$ is measured in the de-excitation process. The quantity probed in experimental measurements is the so-called differential decay rate or EC spectrum. The explanation of this highly non-trivial quantity requires an accurate theoretical description of the atomic relaxation process which is one of the major goals of this work.

In section 1.1, we introduce the different decay channels driving the atomic relaxation process and furthermore motivate the level of theory necessary for their precise description.

1.1 Differential decay rate – discrete meets continuous

As we have already indicated in the previous section and will discuss in more detail in sections 1.2 and 1.3, the precise knowledge of the spectrum describing the atomic relaxation is of great importance. On the one hand for the use of radionuclides in practical applications like in cancer treatment, on the other hand for the determination of the neutrino mass. In the case of nuclear decay by EC

the total amount of released energy corresponds to the Q-value which is shared between the energy taken away by the neutrino E_ν and the energy stored in terms of electronic excitations ω measured in the experiment.

The differential decay rate $\frac{\mathrm{d}\Gamma}{\mathrm{d}\omega}(\omega)$ corresponds to the number of decays per unit of time within the energy interval $[\omega, \omega + \mathrm{d}\omega]$ divided by the size of the interval $\mathrm{d}\omega$. Although atomic relaxation happens within an atom characterized by a discrete set of energy levels, the differential decay rate is a continuous function, i.e. one observes spectral weight at all energies from zero up to the Q-value. Furthermore, the EC spectrum exhibits several interesting features like multiplets or asymmetric line-shapes. To understand the underlying mechanisms leading to these features, various different effects must be taken into account in the theoretical description.

The EC decay for ^{163}Ho is very well studied, in particular since ^{163}Ho is the ideal candidate for determining the neutrino mass. A more detailed discussion is given in the following section. Fig. 1.1 shows the differential decay rate for the example of ^{163}Ho which decays by EC into an excited daughter ^{163}Dy* atom plus an electron-neutrino. The blue curve illustrates the calculated spectrum on a basis of bound states based on the theory developed in [9]. A comparison with the experimental spectrum plotted in grey reveals that the most simple spectral features can already be understood on this level of theory. This includes the main resonances as well as the satellite structures close to the 4*s* edge .

As we will see in chapter 3, hyperfine interaction can have a considerable impact on the observed resonances. Although several orders of magnitude smaller than the energy scale at which nuclear decay takes place, different initial hyperfine states can lead to a shift of spectral weight on the Rydberg energy scale. A change in the initial hyperfine state may even cause some resonances to completely disappear, while others are significantly enhanced. To account for these effects, the simplest level of theory presented in [9] must be extended by the non-spherical part of the interaction between nuclear and electronic degrees of freedom.

At this level of theory, one typically assumes the spectral line-shapes to be described by Lorentzians. However, a comparison of the blue curve in Fig. 1.1 with the experimental data shown in grey reveals that far away from a resonance the agreement is not good. To accurately describe the spectrum at these energies, additional decay channels have to be included in the calculations. As has been shown on the example of ^{163}Ho [11], the scattering of electrons into unbound

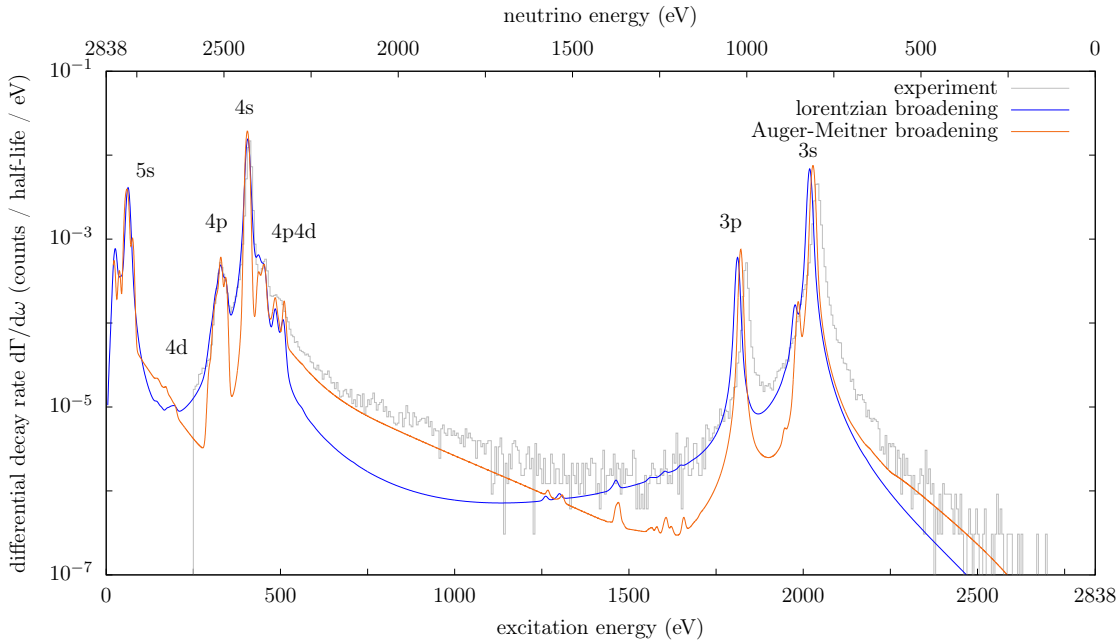

Figure 1.1: Differential decay rate $\frac{d\Gamma}{d\omega}(\omega)$ for the EC decay in ^{163}Ho as a function of the neutrino energy (top scale) or the electronic excitation energy (bottom scale). In grey we show the experimental spectrum measured within ECHo [10]. The blue spectrum shows a theoretical calculation including only bound states. The calculated orange spectrum in addition allows core excited states to de-excite via Auger-Meitner decay into the continuum. The labeling indicates the core hole in one of the shells of the excited Dy atom. The figure is taken from [11] where further details regarding the calculations can be found.

states plays a crucial role for the line-shape. The important discovery that an excited atom can also emit electrons was made independently by Meitner in 1922 [12] and by Auger one year later [13], and has since been referred to as Auger-Meitner decay. If the excitation energy of the atom after EC exceeds the atom's auto-ionization threshold, electrons can be transferred into the continuum. In this process, an electron from one of the outer shells fills the created core hole, thereby transferring its energy to a second electron. If the transferred energy is larger than its binding energy, the electron can eventually escape the atom. Since the energy of an Auger-Meitner electron can assume all values up to the Q-value, its energy spectrum is continuous. Hence, Auger-Meitner decay affects the spectral line-shape on the full energy window. The orange curve displayed in Fig. 1.1 shows the calculated differential decay rate including Auger-Meitner

decay. Compared to the blue curve we observe a pronounced energy-dependent, asymmetric broadening of the resonances in very good agreement with the experiment.

While Auger-Meitner decay dominates the atomic relaxation at lower excitation energies, fluorescence decay becomes particularly important for energies starting from the K-edge. Due to a Q-value of only about 2.8 keV, the K-edge is not apparent in the ^{163}Ho spectrum. However, for most other EC isotopes the Q-value is of the order of several hundred keV, such that the K-edge becomes visible in the spectrum.

Fluorescence decay describes the coupling of a core excited state to the continuous spectrum of the electromagnetic field leading to the emission of photons. As the photon's energy plus that of the neutrino does not necessarily have to correspond to Q, additional energy can be stored in terms of electronic excitations. Therefore, a photon produced during the de-excitation process can assume all energies from zero up to the Q-value, thus exhibiting a continuous energy spectrum. Consequently, the differential decay rate has non-vanishing spectral weight at all electronic excitation energies. A detailed discussion of fluorescence decay and its impact on the spectral line-shape will be discussed in chapter 4.

1.2 Neutrinos – A door to physics beyond the Standard Model

In the years following the discovery of radioactivity in 1896, spectra of numerous radionuclides were measured. One very important measurement, the result of which remained a mystery for almost three decades, was performed by Chadwick in 1914 [14]. He could show experimentally that the energy spectrum of the electron emitted in the beta decay is continuous. At that time an unexpected and puzzling result, since it was assumed that the total released energy is shared between two particles, the atomic nucleus and the emitted electron. This, however, would imply due to energy and momentum conservation the electron's energy to be discrete.

In 1930, after numerous attempts to explain the continuous beta spectrum failed, Pauli came up with the idea of postulating a new particle, the neutrino [15]. Four years later, in 1934, it was Fermi who provided the theoretical framework describing the beta decay [16], which paved the way for the development of the theory

of weak interaction in the 1960s. Shortly after the theoretical formulation of the beta decay, Wick, one of Fermi's collaborators, extended his theory to the case of electron capture. It took another 22 years until Cowan and Reines in 1956 finally could prove the existence of the neutrino [17].

In the following years, the theories of the weak and the strong interaction were developed, which finally led to the formulation of the Standard Model (SM) of particle physics. Since then, the SM has proved as an extremely successful theory. According to the SM, neutrinos are massless fermions and occur in three so-called flavors: the electron-neutrino ν_e, the muon-neutrino ν_μ and the tau-neutrino ν_τ asscociated to the charged leptons (electron, muon and tauon). However, as we will see, the assumption of massless neutrinos turned out to be wrong.

The journey towards experimental evidence of massive neutrinos by the discovery of neutrino oscillations, started in 1968 with the Homestake experiment [18]. A large number of electron-neutrinos is produced in nuclear fusion reactions in the sun. As neutrinos are not charged, they only interact via gravity and the weak force. Consequently, the neutrino's interaction cross section with other particles is very small, such that practically all produced neutrinos can escape the sun and finally arrive on earth. The goal of the Homestake experiment was to determine the solar neutrino flux. The basic idea was to count the number of ^{37}Ar produced in the inverse beta-decay $\nu_e + {}^{37}_{17}\mathrm{Cl} \rightarrow e^- + {}^{37}_{18}\mathrm{Ar}$ induced by the incoming solar neutrinos. However, the measured neutrino flux turned out to be much smaller than theoretically predicted by the solar standard model [19]. This deficiency could be confirmed by numerous other experiments including SAGE [20], GALLEX [21] and Super-Kamiokande [22] and since then is known as the solar neutrino problem.

More than three decades after the discovery of the solar neutrino problem, so-called neutrino flavor transformations were observed in the Sudbury Neutrino Observatory (SNO) experiment [23]. Electron-neutrinos, the only neutrino flavor produced in solar fusion reactions, transform over large distances into tau- and muon-neutrinos. This observation could be explained by a quantum mechanical effect known as neutrino oscillations [6] which can only take place if the neutrino's three eigenmasses are finite, or more precisely, at least two of them are finite. Notably, it was Pontecorvo who discussed the possibility of neutrino oscillations already in 1967 [24], long before these were finally confirmed in the SNO experiment in 2001. Up to today, however, only differences of the squared masses are known. The knowledge of the absolute neutrino mass constitutes one of the

big unsolved problems in modern physics opening the door to physics beyond the Standard Model [7].

Neutrino mass determination by electron capture

One approach to determine the neutrino mass in a model-independent way is the measurement of the EC decay spectrum. In an EC decay the total released energy Q is shared between the energy stored in electronic excitations ω, which eventually is released in terms of Auger-Meitner electrons and photons, and the energy taken away by the neutrino E_ν. Thus, the neutrino's energy can be written as $E_\nu = Q - \omega$. Assuming the neutrino to be massless as predicted by the SM, the minimal energy it can assume is zero. In this case, the EC spectrum has non-vanishing intensity ranging from zero up to Q. The minimal energy of a massive neutrino, on the other hand, just corresponds to its rest-mass m_ν, such that the EC spectrum extends only up to an maximal energy of $\omega_{\max} = Q - m_\nu$. Therefore, the impact of a finite neutrino mass on the spectrum is largest close to its endpoint.

To determine the neutrino mass in this way, two measurements are required: First, a very precise measurement of the Q-value achievable with Penning-trap mass spectroscopy [25]. Second, a high statistics de-excitation spectrum with very high energy resolution. Here the favorable approach is a calorimetric measurement first proposed by De Rújula and Lusignoli in 1982 [26]. The basic idea is to measure the total energy released in terms of photons, Auger-Meitner electrons (and nuclear recoil) using low temperature metallic magnetic calorimeters (MMC) [27] which is possible with a quantum efficiency of practically 100% when the decaying nuclide is directly implanted in the detector [28].

Once these two measurements are performed, the theoretical line-shape (obtained for the measured Q-value) can be fitted to the experimental data using the neutrino mass (or masses) as free parameter(s). In order to achieve a very high accuracy for the neutrino mass, this requires besides the precise measurements of the Q-value and spectrum, also a very accurate theoretical description of the spectral line-shape. The level of theory required and the challenges associated with it were discussed in section 1.1.

The best sensitivity to the neutrino mass is achieved for EC isotopes with very small Q-values, since here the relative number of data points in the vicinity of the endpoint is largest. The nuclide with the smallest possible Q-value of about 2.8 keV is ^{163}Ho [10] which is investigated in the 'Electron Capture in ^{163}Ho - ECHo -

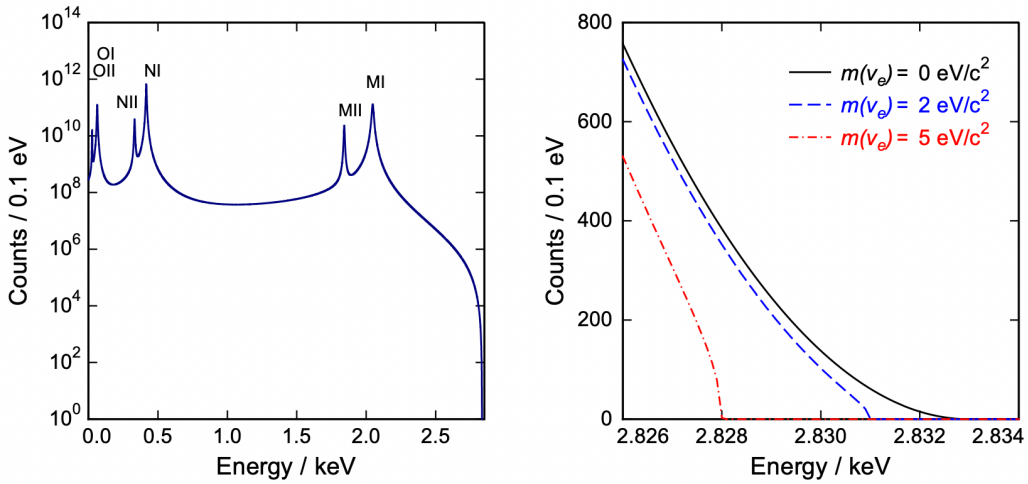

Figure 1.2: Left: EC spectrum of ^{163}Ho calculated for $Q = 2.833$ keV assuming a zero neutrino mass. Right: EC spectrum of ^{163}Ho close to the endpoint calculated for different neutrino masses ($m_{\nu_e} = 0, 2$ and 5 eV/c^2). The figure is taken from [28].

Experiment' [28], HOLMES [29] and NuMECS ('Neutrino Mass via Electron Capture Spectroscopy) [30]. All three experiments are based on the aforementioned calorimetric measurement with the aim of determining the neutrino mass with sub-eV accuracy.

Fig. 1.2 displays the calculated EC spectrum on the full energy domain (left), i.e. from zero up to Q, and close to the endpoint (right) for three different neutrino masses ($m_{\nu_e} = 0, 2$ and 5 eV/c^2). The resonances labeled in the full spectrum on the left correspond to states with one core hole in the 3s (M I), 3p (M II), 4s (N I), 4p (N II), 5s (O I) and 5p (O II) shell. For a finite neutrino mass the spectrum's endpoint is shifted to smaller excitation energies compared to the case of a massless neutrino, as can be inferred from the right plot of Fig. 1.2.

1.3 Electron capture in radiotherapy

Radionuclides including those that undergo alpha-, beta- and EC decays, are widely used in medical applications, especially in cancer therapy, and have been established as an effective method in this field over the past decades [31, 32]. Nevertheless, the search for novel therapeutic approaches based on radionuclides not yet in use continues [33, 34].

In general, the method of treatment depends on the nature of the tumor, i.e. its shape, location and, most importantly, its size. Large tumors are usually detected by common imaging techniques such as computer tomography (CT) or magnetic resonance imaging (MRI). Once detected, they are either surgically removed, or irradiated from the outside. For smaller tumors, however, these methods are not applicable, since the tumor's size is often so small to be detected with the available imaging methods [4].

A favorable approach to destroy very small tumors is to transport the radionuclide directly to the cancer cell by using small molecules or nanoparticles. Currently, even subcellular localization approaches in which the radionuclide is directly brought into the DNA of the cancer cell are under investigation [35]. In order to damage only as little as possible of the normal tissue surrounding the cancer cell, it must be ensured that the tumor tissue absorbs most of the radiation dose which in turn requires a highly localized dose-deposition [35].

This can be achieved with the help of radionuclides releasing the main part of their energy in the form of Auger-Meitner electrons, most of which decay by EC. Once a core electron has been captured, the resulting vacancy is filled from electrons populating outer shells leading to the emission of photons and Auger-Meitner electrons. For all shells except the K shell, the latter typically dominates leading to the emission of Auger-Meitner electrons of relatively low kinetic energy ($\leq$ 25 keV) [32]. This is advantageous for the irradiation of small tumors, since electrons at such low energies exhibit a very high linear energy transfer (LET) in human tissue and therefore lead to severe damage when brought close to the cancer cell.

Whether a radionuclide is suitable for medical applications is often based on theoretical radiation spectra including both, the fluorescence and electron yield spectrum. These spectra provide information about the number and energy of photons or electrons released in the decay [5]. However, as the International Atomic Energy Agency (IAEA) stated back in 2011 [5, 36], it is necessary to determine "[...] the energies and emission probabilities of the low-energy X-rays and Auger electrons to a higher degree of detail and consistency than is available at present." Chapter 4 of this work is devoted to this problem and deals with the accurate description of the fluorescence decay including the yield spectrum.

Outline

The thesis is structured as follows. In chapter 2, the theoretical fundamentals necessary to describe nuclear decay by EC and subsequent atomic relaxation are introduced. First, the concept of density functional theory is described. Then, the most relevant parts of the Hamiltonian including Dirac's Hamiltonian, the mutual Coulomb interaction between bound electrons and the weak interaction are briefly introduced. Subsequently, it is shown how to calculate EC spectra. At the end of this chapter, EC spectra for selected radionuclides which undergo *allowed* transitions are presented.

Chapter 3 deals with the investigation of the influence of hyperfine interaction on the nuclear decay by EC. Using a simple model the underlying mechanism is illustrated. Then, the EC spectrum for different initial hyperfine states is presented for the example of atomic ^{163}Ho. Afterwards, the impact on the isotope's lifetime is investiagted. In the last part of this chapter, a realistic experimental setup found in the ECHo experiment [28] is discussed. In this context, the non-spherical chemical environment and finite temperatures are included in the calculations.

In chapter 4, the impact of fluorescence decay on the spectral line-shape is investigated. Starting from a multipole expansion of the (relativistic) light-matter interaction, expressions for the fluorescence self-energy and the fluorescence yield spectrum are derived. Finally, the results are applied to the example of ^{55}Fe. The EC spectrum employing the derived fluorescence self-energy and the fluorescence yield spectrum is calculated.

In chapter 5, an iterative approach to determine an optimized single-particle basis set for the quantum nuclear many-body problem is presented. The benefits of the resulting *generalized* natural orbitals are outlined and possible implications for *ab initio* nuclear many-body calculations are discussed.

Chapter 6 is dedicated to the study of resonant and nonresonant inelastic x-ray scattering off matter. Two spectroscopic techniques describing the respective processes, Resonant (RIXS) and Nonresonant Inelastic X-ray Scattering (NIXS), are introduced. The interference between these two scattering channels is investigated. Using the example of $d - d$ excitations in Nickel oxide, a systematic analysis of the underlying energy and angular dependence of the interference is provided.

A summary of this thesis including an outlook can be found in chapter 7.

2 The theory of electron capture spectroscopy

In this chapter we discuss the theoretical fundamentals necessary to describe the nuclear decay by EC and subsequent atomic relaxation, which constitutes a major part of this work. Essentially, the description of the EC process can be separated into two main parts: The first part is to determine the ground state of the parent atom $|\Psi_0\rangle$. Typical atoms that undergo EC reactions are made of up to ~ 100 interacting electrons moving in the spherical symmetric Coulomb potential of the atomic nucleus. Therefore, the first task is to solve a correlated many-particle problem. Once the ground state has been found, the second problem is to determine the dynamics following EC.

We obtain the parent ground state $|\Psi_0\rangle$ by diagonalization of the Hamiltonian comprising the kinetic energy of the electrons and their mutual Coulomb interaction. Before this can be done, the Hamiltonian is expanded on a single-particle basis obtained from density functional theory. For the diagonalization we employ Lanczos' algorithm [37, 38], which is briefly introduced in appendix A.1. Once the parent ground state has been found, one can focus on the second part of the problem, the calculation of the atom's response to EC. As the weak interaction is small compared to the Coulomb repulsion between the electrons, it is treated in fist-order perturbation theory. Moreover, EC can be considered as a low-energy weak process, which allows us to use an expression of the weak interaction for this limiting case.

In the time domain we start at time $t = 0$ by annihilating a core electron, transforming a proton inside the nucleus into a neutron and simultaneously create an electron-neutrino. The atom ends up in an excited state and starts to evolve in time. During this relaxation process, energy is released in terms of photons and Auger-Meitner electrons. The de-excitation spectrum corresponds to a Fourier transform of the time evolution. A favorable method to experimentally determine the de-excitation spectrum is a calorimetric measurement which we briefly outlined in the introduction (see section 1.2). The result of such a measurement is the so-called differential decay rate $\frac{\mathrm{d}\Gamma}{\mathrm{d}\omega}(\omega)$ or (the more frequently used de-

nomination) EC spectrum. The EC spectrum corresponds to the number of decays per energy and unit of time. To determine this quantity theoretically, we choose an approach in terms of Green's functions which is well established in field of core-level spectroscopy [39, 40] and has been further developed by Braß and Haverkort to describe the EC spectrum of ^{163}Ho [9]. Here the main problem in the determination of the EC spectrum is to calculate the resolvent $\frac{1}{\omega - H}$. The Hamiltonian H governing the dynamics subsequent to EC comprises besides the kinetic energy of the electrons all interactions except the weak interaction, i.e. the mutual Coulomb repulsion between bound electrons, the coupling to the electromagnetic field as well as the scattering of bound electrons into the continuum.

In the remainder of this chapter we start with an introduction to density functional theory, a self-consistent mean-field method, from which a set of single-particle states, the so-called Kohn-Sham orbitals, is extracted. Then, in sections 2.2 and 2.3, we provide expressions for the Dirac Hamiltonian and the Coulomb interaction expanded on a basis of Kohn-Sham orbitals. Section 2.4 briefly outlines the Hamiltonian describing the neutrino. In section 2.5, an effective low-energy expression of the weak interaction in second quantized form is discussed. Finally, we provide the main equations necessary to compute the EC spectra focusing on the most simple case of so-called *allowed* transitions and in addition, present calculated EC spectra for some selected isotopes.

Throughout this thesis we will employ natural units, i.e. Planck's constant $\hbar$, the speed of light c and the vacuum permittivity are ϵ_0 are unity.

2.1 Density functional theory

Throughout this thesis, the starting point of every many-body calculation is density functional theory (DFT) [41, 42], a self-consistent mean field method, from which a set of single-particle states is extracted. On this set of states, the underlying single- and many-particle parts of the Hamiltonian are expanded.

DFT is based on two theorems formulated by Hohenberg and Kohn in 1964 [43]. The first theorem states that for a system of interacting electrons in an external potential $v_{\text{ext}}(\mathbf{r})$ (which can be the Coulomb potential of the nucleus as well as external electromagnetic fields), is uniquely determined by the ground state density $n_0(\mathbf{r})$. The statement of the second theorem is that there exists a universal

functional for the energy in terms of the density $n(\mathbf{r})$ [44],

$$E[n] = F[n] + \int \mathrm{d}^3 r \; v_{\text{ext.}}(\mathbf{r}) n(\mathbf{r}) \tag{2.1}$$

$$F[n] = T[n] + W[n] \tag{2.2}$$

and the correct ground state density can be found by minimizing $E[n]$ via the variational principle. However, the minimization of the energy is very impracticable, because Hohenberg and Kohn do not provide an explicit expression of $E[n]$.

In 1965 Kohn and Sham proposed to replace the interacting many-body system by a virtual one of non-interacting particles with the same ground state density [42]. The energy functional of this auxiliary system is given by [44]

$$E_{\text{KS}}[n] = T_{\text{s}}[n] + E_{\text{H}}[n] + \int \mathrm{d}^3 r \; v_{\text{ext}}(\mathbf{r}) n(\mathbf{r}) + E_{\text{xc}}[n]. \tag{2.3}$$

Here $T_{\text{s}}[n]$ denotes the kinetic energy of the non-interacting system (the subscript s stands for single-particle), $E_{\text{H}}[n] = \frac{1}{2} \int \mathrm{d}^3 r \mathrm{d}^3 r' \; \frac{n(\mathbf{r}) n(\mathbf{r}')}{|\mathbf{r}-\mathbf{r}'|}$ the Hartree potential energy and $v_{\text{ext}}(\mathbf{r})$ the external potential due to the atomic nucleus as well as potential external electromagnetic fields. The exchange-correlation energy functional $E_{\text{xc}}[n]$ corresponds to the difference of the exact energy functional $E[n]$ and the known part of the auxiliary system which comprises the kinetic energy, the Hartree term and the contributions from external potential [44]

$$E_{\text{xc}}[n] = E[n] - T_{\text{s}}[n] - E_{\text{H}}[n] - \int \mathrm{d}^3 r \; v_{\text{ext}}(\mathbf{r}) n(\mathbf{r}). \tag{2.4}$$

$E_{\text{xc}}[n]$ takes into account all the quantum effects and is the same for all classes of materials. The variation of the Kohn-Sham energy functional with respect to the density leads to

$$\frac{\delta E_{\text{KS}}[n]}{\delta n} = \frac{\delta T_{\text{s}}[n]}{\delta n} + v_{\text{ext}}(\mathbf{r}) + \int \mathrm{d}^3 r' \; \frac{n(\mathbf{r}')}{|\mathbf{r}-\mathbf{r}'|} + \frac{\delta E_{\text{xc}}[n]}{\delta n} \tag{2.5}$$

where it is used that $\frac{\delta E_{\text{H}}[n]}{\delta n} = \int \mathrm{d}^3 r' \; \frac{n(\mathbf{r}')}{|\mathbf{r}-\mathbf{r}'|}$. The Kohn-Sham potential is defined by the sum of all terms except the one originating from the kinetic energy

$$v_{\text{KS}}[n](\mathbf{r}) = v_{\text{ext}}(\mathbf{r}) + \int \mathrm{d}^3 r' \; \frac{n(\mathbf{r}')}{|\mathbf{r}-\mathbf{r}'|} + v_{\text{xc}}[n](\mathbf{r}) \tag{2.6}$$

where $v_{\text{xc}}[n](\mathbf{r}) = \frac{\delta E_{\text{xc}}[n]}{\delta n(\mathbf{r})}$ is the functional derivative of the exchange-correlation energy with respect to the density. The problem of an interacting many-body system is finally transformed to a single-particle one where the particles are moving

in the effective potential $v_{\mathrm{KS}}[n](\mathbf{r})$. The resulting Schrödinger equations for the single-particle orbitals $\phi_\tau(\mathbf{r})$ with quantum numbers τ read

$$\left(-\frac{\nabla^2}{2m} + v_{\mathrm{KS}}[n](\mathbf{r})\right)\phi_\tau(\mathbf{r}) = \epsilon_\tau \phi_\tau(\mathbf{r}) \tag{2.7}$$

and are called the Kohn-Sham equations. The corresponding density is obtained by

$$n(\mathbf{r}) = \sum_{i=1}^{N} |\phi_\tau(\mathbf{r})|^2 \tag{2.8}$$

where N is the number of particles. In order to solve the Kohn-Sham equation, one first has to make a choice (different possibilities) for the exchange-correlation functional. As the Kohn-Sham potential $v_{\mathrm{KS}}[n](\mathbf{r})$ itself is a functional of the density, the solution must be found self-consistently. The calculation starts by assuming an initial density for which $v_{\mathrm{KS}}[n](\mathbf{r})$ is calculated. Then the single-particle Schrödinger equation is solved and a new density calculated via (2.8). This process is reiterated until the change in density falls below a predefined threshold. Once the convergence criterion is fulfilled, the calculation stops and one obtains an approximated ground state energy as well as a set of single-particle Kohn-Sham orbitals which define a basis set for the single-particle Hilbert space.

An extension of non-relativistic to relativistic DFT including the mathematical background is discussed in [41]. The main difference compared to the non-relativistic framework is that the kinetic energy is described by Dirac's Hamiltonian, such that the relativistic Kohn-Sham equations take the form [41]

$$H_{\mathrm{KS}}\phi_\tau(\mathbf{r}) = \left(-i\boldsymbol{\alpha}\cdot\boldsymbol{\nabla} + \beta m + v_{\mathrm{KS}}[n](\mathbf{r})\right)\phi_\tau(\mathbf{r}) = \epsilon_\tau\phi_\tau(\mathbf{r}). \tag{2.9}$$

The quantities $\boldsymbol{\alpha}$ and β are the 4×4 dimensional Dirac matrices [45]

$$\boldsymbol{\alpha} = \begin{pmatrix} 0 & \boldsymbol{\sigma} \\ \boldsymbol{\sigma} & 0 \end{pmatrix} \qquad \beta = \begin{pmatrix} \mathbb{1} & 0 \\ 0 & -\mathbb{1} \end{pmatrix} \tag{2.10}$$

where $\boldsymbol{\sigma}$ is the vector of Pauli matrices.

Assuming that the potential $v_{\mathrm{KS}}[n](\mathbf{r})$ is spherical symmetric, the solutions $\phi_\tau(\mathbf{r})$ are characterized by the quantum numbers $\tau = \{n, l, j, m\}$. Here n denotes the principal quantum number, l and j are the angular- and total angular momentum quantum numbers, respectively, whereas m is the magnetic quantum number related to j. These states are conveniently labeled by the relativistic quantum number κ

$$\kappa(l, j) = (-1)^{(l+j+1/2)}\,(j + 1/2) \tag{2.11}$$

which enables us to write the single-particle states as [45]

$$\phi_\tau(\mathbf{r}) = \begin{pmatrix} G_{n\kappa}(r)\Omega_{\kappa m}(\theta,\phi) \\ \mathrm{i}F_{n\kappa}(r)\Omega_{-\kappa m}(\theta,\phi) \end{pmatrix} \tag{2.12}$$

where $\tau = \{n, \kappa, m\}$. $G_{n\kappa}(r)$ is the large and $F_{n\kappa}(r)$ the small component of the radial wave function, where $\Omega_{\kappa m}(\theta,\phi)$ represents a spherical spinor. Spherical spinors are eigenstates of $\boldsymbol{J}^2$ and J_z and can be constructed by combing spherical harmonics $Y_{lm_l}(\theta,\phi)$, the eigenstates of $\boldsymbol{L}^2$ and L_z, with two-component spinors χ_{m_s}, which are eigenstates of $\boldsymbol{S}^2$ and S_z [46]:

$$\Omega_{\kappa m}(\theta,\phi) = \sum_{m_l=-l(\kappa)}^{l(\kappa)} \sum_{m_s=-1/2}^{1/2} C^{j(\kappa)m}_{l(\kappa)m_l\frac{1}{2}m_s} Y_{l(\kappa)m_l}(\theta,\phi)\chi_{m_s} \tag{2.13}$$

Here, $C^{jm}_{lm_l\frac{1}{2}m_s}$ is a Clebsch-Gordan coefficient [47].

All calculations presented in this work are based on Kohn-Sham orbitals obtained from a DFT calculation using the full-potential local-orbital minimum-basis code FPLO [48].

2.2 Central-field Dirac Hamiltonian

Since most EC isotopes exhibit a large nuclear charge number Z and, in addition, EC involves a core hole close to the nucleus, a relativistic description of the kinetic energy is necessary. Therefore, we employ Dirac's Hamiltonian H_D. For an electron bound in the spherical symmetric Coulomb potential of a point-like nucleus with charge number Z, the Dirac Hamiltonian takes the form [45]

$$H_D = -i\boldsymbol{\alpha}\cdot\boldsymbol{\nabla} + \beta m - \frac{\alpha Z}{r}. \tag{2.14}$$

Here, $-\frac{\alpha Z}{r}$ denotes the spherical symmetric Coulomb potential with fine-structure constant α and $\boldsymbol{\alpha}$, β are the Dirac matrices introduced in (2.10). Once we have found a single-particle basis set given by the Kohn-Sham orbitals $\{\phi_\tau(\mathbf{r})\}$ obtained from a DFT calculation, Dirac's Hamiltonian is expanded on this basis. In second quantization, it can be written as

$$H_D = \sum_{\tau_e\tau_e'} t_{\tau_e\tau_e'} e^\dagger_{\tau_e} e_{\tau_e'} \tag{2.15}$$

where $e^\dagger_{\tau_e}$ $(e_{\tau_e'})$ creates (annihilates) an electron with quantum numbers τ_e (τ_e'). The matrix elements $t_{\tau_e\tau_e'}$ on a basis of Kohn-Sham orbitals (2.12) are given by an angular part times a radial part as is shown in [45]

$$t_{\tau_e\tau_e'} = \delta_{\kappa_e\kappa_e'}\delta_{m_e m_e'} \int_0^\infty (g_{\tau_e}(r), f_{\tau_e}(r)) \begin{pmatrix} m - \alpha\frac{Z}{r} & -\partial_r + \frac{\kappa}{r} \\ \partial_r + \frac{\kappa}{r} & -m - \alpha\frac{Z}{r} \end{pmatrix} \begin{pmatrix} g_{\tau_e'}(r) \\ f_{\tau_e'}(r) \end{pmatrix} \mathrm{d}r \tag{2.16}$$

where $g_{n\kappa}(r) := rG_{n\kappa}(r)$ and $f_{n\kappa}(r) := rF_{n\kappa}(r)$.

2.3 Coulomb interaction

The Hamiltonian used to determine the ground state before EC, as well as the Hamiltonian governing the dynamics afterwards, both include a single- and a two-particle part. The single-particle part is described by Dirac's Hamiltonian. The two-particle part is given by the Coulomb interaction between the electrons. Coulomb interaction plays an outstanding role in particular during the atomic relaxation process subsequent to electron capture, as it is responsible for most features visible in the spectra. Two electrons bound in an atom may scatter into two (not necessarily different) bound orbitals or into unbound states.

In the following, we introduce the Coulomb interaction involving solely bound states and present the associated two-particle matrix elements. In second quantization the Coulomb interaction can be written as

$$H_C = \frac{1}{2} \sum_{\tau_a'\tau_b'\tau_a\tau_b} U_{\tau_a'\tau_b'\tau_a\tau_b} e^\dagger_{\tau_a'} e^\dagger_{\tau_b'} e_{\tau_b} e_{\tau_a} \tag{2.17}$$

where the sum extends over all single-particle quantum numbers τ. The prefactor of $\frac{1}{2}$ takes care of double counting as each pair of electrons only repels once. $U_{\tau_a'\tau_b'\tau_a\tau_b}$ denote the two-particle matrix elements which on a basis of Kohn-Sham orbitals $\phi_\tau(\mathbf{r})$ calculated by DFT take the form

$$U_{\tau_a'\tau_b'\tau_a\tau_b} = \int \phi^\dagger_{\tau_a'}(\mathbf{r}_1)\phi_{\tau_a}(\mathbf{r}_1) \frac{e^2}{|\mathbf{r}_1 - \mathbf{r}_2|} \phi^\dagger_{\tau_b'}(\mathbf{r}_2)\phi_{\tau_b}(\mathbf{r}_2)\, \mathrm{d}r_1^3 \mathrm{d}r_2^3. \tag{2.18}$$

In order to perform numerical calculations, it is convenient to expand the Coulomb potential $\frac{e^2}{|\mathbf{r}_1-\mathbf{r}_2|}$ between two electrons at positions $\mathbf{r}_1$ and $\mathbf{r}_2$ in terms of spherical tensor operators [49]

$$\frac{e^2}{|\mathbf{r}_1 - \mathbf{r}_2|} = e^2 \sum_{k=0}^\infty \frac{r_<^k}{r_>^{k+1}} \sum_{q=-k}^k (-1)^q C^{(k)}_{-q}(\hat{r}_1) C^{(k)}_q(\hat{r}_2) \tag{2.19}$$

where $r_< = \min[r_1, r_2]$ and $r_> = \max[r_1, r_2]$ and where $C_m^{(k)}(\hat{r})$ represents a renormalized spherical harmonic defined by $C_m^{(k)}(\hat{r}) = \sqrt{4\pi/(2k+1)}Y_m^{(k)}(\hat{r})$. Employing the spherical tensor expansion (2.19), the matrix elements $U_{\tau_a'\tau_b'\tau_a\tau_b}$ decompose into products of radial and angular integrals. The latter can be solved analytically by means of Wigner-Eckart's theorem leading to [49]

$$U_{\tau_a'\tau_b'\tau_a\tau_b} = e^2 \sum_{k=0}^{\infty} \sum_{q=-k}^{k} (-1)^{(j_a'+j_b'-m_a'-m_b'-q)} \begin{pmatrix} j_a' & k & j_a \\ -m_a' & q & m_a \end{pmatrix} \begin{pmatrix} j_b' & k & j_b \\ -m_b' & -q & m_b \end{pmatrix} \times \langle \Omega_{\kappa_a'} || C^{(k)} || \Omega_{\kappa_a} \rangle \langle \Omega_{\kappa_b'} || C^{(k)} || \Omega_{\kappa_b} \rangle R_k(\tau_a'\tau_b'\tau_a\tau_b). \quad (2.20)$$

Here the expression in round brackets with six entries denotes the Wigner 3-symbol. A comprehensive description of all its properties can be found in [47, 50]. The expression $\langle \Omega_{\kappa_a'} || C^{(k)} || \Omega_{\kappa_a} \rangle$ is a so-called reduced matrix element which vanishes if $l_a' + k + l_a$ is odd and takes the value

$$\langle \Omega_{\kappa_a'} || C^{(k)} || \Omega_{\kappa_a} \rangle = (-1)^{j_a'+1/2} \sqrt{(2j_a'+1)(2j_a+1)} \begin{pmatrix} j_a' & j_a & k \\ -1/2 & 1/2 & 0 \end{pmatrix} \quad (2.21)$$

if $l_a' + k + l_a$ is even. The peculiarity of reduced matrix elements is that they are independent of the magnetic quantum numbers.

The radial integrals of the Coulomb matrix elements are given by the (relativistic) Slater-integrals $R_k(\tau_a'\tau_b'\tau_a\tau_b)$ which explicitly are given by [49]

$$R_k(\tau_a'\tau_b'\tau_a\tau_b) = \int_0^\infty \int_0^\infty \mathrm{d}r_1 \mathrm{d}r_2 \frac{r_<^k}{r_>^{k+1}} \Big(g_{n_a'\kappa_a'}(r_1) g_{n_a\kappa_a}(r_1) + f_{n_a'\kappa_a'}(r_1) f_{n_a\kappa_a}(r_1) \Big) \times \Big(g_{n_b'\kappa_b'}(r_2) g_{n_b\kappa_b}(r_2) + f_{n_b'\kappa_b'}(r_2) f_{n_b\kappa_b}(r_2) \Big) \quad (2.22)$$

where $g_{n\kappa}(r) = rG_{n\kappa}(r)$ and $f_{n\kappa}(r) = rF_{n\kappa}(r)$. In all calculations performed throughout this thesis, the Slater integrals are evaluated numerically using the quantum many-body script language Quanty [51, 52].

2.4 Neutrino masses

The neutrino oscillations detected in the SNO experiment [23] are a clear indication that the eigenstates of the weak interaction, i.e. the electron-neutrino, the muon-neutrino and the tau-neutrino periodically transform into each other as they propagate over large distances. A quantum mechanical description of this

phenomenon was first discussed by Pontecorvo in 1967 [24] and is based on the relation between the three mass eigenstates, i.e. the eigenstates of the free Hamiltonian, and the aforementioned weak eigenstates. These two sets of eigenstates are related to each other by a unitary 3×3 matrix, the so-called Pontecorvo-Maki-Nakagawa-Sakata (PMNS) matrix U [53]. Hence, an electron-neutrino, for instance, can be written as a superposition of the three mass eigenstates ν_1, ν_2 and ν_3

$$|\nu_e\rangle = \sum_{a=1}^{3} U_{ea}^{*} |\nu_a\rangle. \tag{2.23}$$

As the Standard Model assumes the neutrino to be massless, this requires a description beyond the Standard Model. Irrespective of whether neutrinos are Dirac or Majorana particles, which up to today is an open question in particle physics [54], neutrinos are fermions of finite mass, such that their mass-diagonal Hamiltonian is given by [55]

$$H_\nu = \sum_{a=1}^{3} \int \psi_{\nu_a}^{\dagger}(\mathbf{x}) \left(-\mathrm{i}\boldsymbol{\alpha} \cdot \boldsymbol{\nabla} + \beta m_a\right) \psi_{\nu_a}(\mathbf{x}) \mathrm{d}^3 x \tag{2.24}$$

where $(\psi_{\nu_a})_{a=1,2,3}$ are the neutrino fields of the mass state a which are related to the flavor fields by

$$\psi_{\nu_a} = \sum_{l \in \{e,\mu,\tau\}} U_{al} \psi_{\nu_l}. \tag{2.25}$$

2.5 Weak interaction

Nuclear decay by EC is a process which is governed by the weak interaction. A core electron is captured while a proton in the nucleus is transformed into a neutron and an electron neutrino is emitted as shown in the Feynman-diagram Fig.2.1. This process is mediated by massive exchange bosons $W^{\pm}$. In contrast to QED, where the exchange interaction is mediated by massless photons, the $W^{\pm}$ have a mass of $m_W = 80.385 \pm 0.015$ GeV [53]. On the other hand, the maximal energy released in an EC decay is of the order of $\sim 10^3$ keV and is therefore at least three orders of magnitude smaller than m_W. Hence, it is justified to consider the low-energy limit where the four-momentum transferred by the $W^{\pm}$ bosons is small compared to its mass, i.e. $q^2 \ll m_W^2$. In this case, the momentum-dependence of the propagator mediating the weak interaction can be approximated by [53]

$$\frac{1}{q^2 - m_W^2} \approx \frac{1}{m_W^2} \tag{2.26}$$

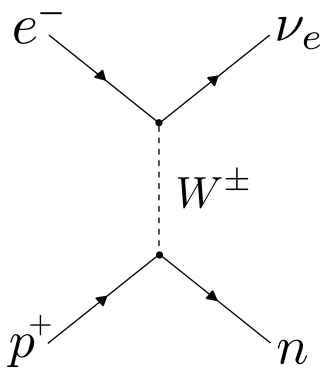

Figure 2.1: Feynman-diagram for the EC process.

such that the effective interaction no longer has a q^2-dependence. From a physical point of view, this means that the interaction occurs at a single point in space-time [53]. Within this approximation the effective low-energy weak interaction is described by a current-current interaction with Hamiltonian density [56]

$$\mathcal{H}_W = -\frac{G_W}{\sqrt{2}}\left[J_\mu(x)L_\mu^\dagger(x) + \text{h.c.}\right] \tag{2.27}$$

where $J_\mu(x)$ and L_μ are the hadron and lepton current, respectively, and weak coupling constant G_W. Under the assumption of point-like nucleons, the currents can be written as

$$\begin{aligned} J_\mu(x) &= i\bar{\psi}_n\gamma_\mu\left(1+\lambda\gamma^5\right)\psi_p \\ L_\mu(x) &= i\bar{\psi}_{\nu_e}(x)\gamma_\mu\left(1+\gamma^5\right)\psi_e(x) \end{aligned} \tag{2.28}$$

where λ denotes a constant and where the adjoint fields are defined as $\bar{\psi}_{\nu_e}(x) = \psi_{\nu_e}^\dagger(x)\gamma_4$ and $\bar{\psi}_n = \psi_n^\dagger\gamma_4$. Here, the $\left(\gamma_\mu\right)_{\mu=1,\ldots,4}$ denote the Dirac γ-matrices and $\gamma_5 = \gamma_1\gamma_2\gamma_3\gamma_4$. The fields $\psi_p(x)$, $\psi_n(x)$, $\psi_e(x)$ and $\psi_{\nu_e}(x)$ describe the proton, neutron, electron and neutrino, respectively, which are either annihilated (proton, electron) or created (neutron, neutrino) in the EC process. Note that we employ the same conventions as in [56].

In the next step, we express the effective low-energy Hamiltonian describing weak interaction H_W associated to the density $\mathcal{H}_W$ in second quantized form. As the neutron, proton and electron are bound particles, their corresponding fields can be expanded on a basis of local orbitals. The neutrino, on the other hand, is regarded as a free particle and thus is expanded on spherical Bessel functions. Following the detailed derivation presented in [55], the final form of H_W expanded

on these orbitals is given by

$$H_W = \sum_{q_\nu,\tau_\nu} \sum_{\tau_e} \sum_{\tau_{\mathrm{nuc}}(i)} \sum_{\tau_{\mathrm{nuc}}(f)} \sum_{JM} (-1)^{j_\nu - m_\nu + I_f - M_{I_f} + M} \begin{pmatrix} I_f & J & I_i \\ -M_{I_f} & -M & M_{I_i} \end{pmatrix} \times \begin{pmatrix} j_\nu & J & j_e \\ -m_\nu & M & m_e \end{pmatrix} p_J^{I_i I_f}(\tau_\nu, q_\nu; \tau_e)\ \nu^\dagger_{\tau_\nu} e_{\tau_e} \otimes |\tau_{\mathrm{nuc}}(f), I_f, M_f\rangle \langle \tau_{\mathrm{nuc}}(i), I_i, M_i| \,. \tag{2.29}$$

Here the sum extends over all quantum numbers of the captured electron (τ_e), the created neutrino (q_ν, τ_ν) and over all additional quantum numbers besides the total nuclear angular momentum and its projection onto the z-axis which are necessary to characterize the initial ($\tau_{\mathrm{nuc}}(i)$) and final ($\tau_{\mathrm{nuc}}(f)$) nuclear state. J is the transferred total angular momentum with projection M, whereas $p_J^{I_i I_f}(\tau_\nu, q_\nu; \tau_e)$ denotes the capture probability which involves besides the wavefunctions of electron and neutrino also that of the initial/final nuclear state. An explicit expression for the capture probability can be found in [55].

From the first 3j-symbol in (2.29), involving the nuclear total angular momenta I_i and I_f, one can infer that in a weak decay the exchanged total angular momentum J is determined by $|I_i - I_f| \leq J \leq I_i + I_f$. Since J is also related to the total angular momentum of the captured electron and the created neutrino, it enters the second 3j-symbol describing the leptonic part thereby determining the total angular momentum of the captured electron j_e and that of the created neutrino j_ν.

Allowed transitions

In this work, we are in particular interested in so-called *allowed* transitions in which the exchanged total angular momentum amounts to $J = 0, 1$, while the parity of the initial and final nuclear wavefunction remains unchanged, i.e. $\pi_i = \pi_f$. *Allowed* transitions are the most simple weak decays for which several approximations of the general expression of the low-energy weak interaction H_W are applicable. In the following, we discuss these in more detail. For this purpose, let us assume an exchanged angular momentum of $J = 1$. Then, the second 3j-symbol vanishes unless $|j_\nu - j_e| \leq 1 \leq j_\nu + j_e$ which implies that, at least in principle, capture is possible from all shells as long as this condition is fulfilled. However, the corresponding capture probabilities for some shells are much bigger than for others.

Therefore, the first common approximation is to consider capture only from those shells which have a large overlap with the nucleus, i.e. from shells with s-character. In a relativistic calculation the single-particle states are described by four-spinors $\phi_{\tau_e}(\mathbf{r})$ and are characterized by the quantum numbers $\tau_e = \{n_e, \kappa_e, m_e\}$. States with $\kappa_e = -1$ have a large component with angular momentum $l_e = 0$, i.e. s-character, and a small component with $l_e = 1$, i.e. p-character. The same is true for orbitals with $\kappa_e = 1$, except that here the small component has s-character and the large p-character. Orbitals with other quantum numbers have no s-character, which is why their capture probability is strongly reduced with respect to that of $\kappa_e = \pm 1$.

The second approximation we want to employ refers to the capture probability $p_J^{I_i I_f}(\tau_\nu, q_\nu; \tau_e)$ itself. In general, the calculation of capture probabilities is very complicated, in particular due to the dependence on the nuclear wave function of the parent and daughter nucleus. As we will discuss in chapter 5, solving the many-nucleon problem from first principles is very challenging and up to now only possible for lighter nuclei, such that approximations become indispensable. Motivated by the different spatial extent of the nucleus $\left(\sim 10^{-15}\mathrm{m}\right)$ and the electrons bound in an atom $\left(\sim 10^{-10}\mathrm{m}\right)$, a common way [56] to overcome the lack of knowledge of the nuclear wave function is to consider relative capture probabilities. Instead of using the probabilities introduced in (2.29), the idea is to replace them by the relative capture probability with respect to the K shell which can be written as [55]

$$\begin{aligned} p_J(\tau_\nu, q_\nu; \tau_e) &:= \frac{p_J^{I_i I_f}(\tau_\nu, q_\nu; \tau_e)}{p_J^{I_i I_f}(\tau_\nu, q_\nu; 1s)} \\ &\approx \int_0^{R_{\mathrm{nuc}}} \left(g_{\tau_\nu} g_{\tau_e} + f_{\tau_\nu} f_{\tau_e}\right) \langle \Omega_{\kappa_\nu} || Y_J || \Omega_{\kappa_e} \rangle - \mathrm{i} \left(g_{\tau_\nu} g_{\tau_e} - f_{\tau_\nu} f_{\tau_e}\right) \langle \Omega_{\kappa_\nu} || Y_J || \Omega_{-\kappa_e} \rangle \mathrm{d}r \end{aligned} \tag{2.30}$$

with nuclear radius R_{nuc}. The advantage here is that $p_J(\tau_\nu, q_\nu; \tau_e)$ is rather insensitive to the exact nuclear wavefunction.

The third approximation to further simplify the theoretical description of *allowed* transitions is to assume the neutrino's wavefunction to be constant in the relevant spatial domain $r \in [0, R_{\mathrm{nuc}}]$. As the radial wavefunction of the neutrino is proportional to a spherical Bessel function $j_{l_\nu}(q_\nu r)$, this may be motivated as follows: Considering the fact that its momentum q_ν is bounded by Q from above, the argument of its radial wavefunction, $q_\nu r$, is small for typical Q-values such

that one can set $j_{l_\nu}(q_\nu r) \approx$ const. In this case, the relative capture probability is solely determined by the overlap of the electron's radial wavefunction with s-character, i.e. either the large component if $\kappa_e = -1$ or the small one if $\kappa_e = 1$, which we label by $R_{\tau_e}(r)$, such that

$$p_J(\tau_e) \approx \int_0^{R_{\text{nuc}}} R_{\tau_e}(r)\mathrm{d}r. \tag{2.31}$$

Note that those contributions in (2.30) involving at least one wavefunction with p-character are neglected.

We are now in a position to replace the complicated general expression of the weak interaction (2.29) by a much simpler transition operator, with the help of which the calculation of the EC spectrum is considerably facilitated. To motivate the form of the transition operator, recall that nuclear decay by EC involves three different parts: the nucleus, the electrons and the neutrino. Due to the weakness of the interaction, the total wavefunction $|\Psi_0\rangle$ of the parent nuclide (which also has to involve these three parts) can approximately be written as a product of a nuclear wavefunction $|\Phi_Z\rangle$, an electronic wavefunction $|\psi_0\rangle$ and the neutrino vacuum $|0_\nu\rangle$, i.e.

$$|\Psi_0\rangle \approx |\Phi_Z\rangle \otimes |\psi_0\rangle \otimes |0_\nu\rangle. \tag{2.32}$$

This state transforms by EC into a state of the form $|\Psi_f\rangle \approx |\Phi_{Z-1}\rangle \otimes |\psi_{\tau_e}(f)\rangle \otimes |q_\nu, \tau_\nu\rangle$. Here $|\Phi_{Z-1}\rangle$ denotes the nuclear wave function after EC where one proton inside the nucleus is transformed into a neutron. $|\psi_{\tau_e}(f)\rangle$ is the (excited) electronic wave function in the modified nuclear potential, whereas the produced neutrino is characterized by its momentum q_ν and the quantum numbers $\tau_\nu = \{\kappa_\nu, m_\nu\, a\}$. Hence, the transition from $|\Psi_0\rangle \to |\Psi_f\rangle$ is mediated by an operator which can be written as a product of nuclear, electronic and neutrino part, respectively,

$$T_{\text{EC}} = T_n T_e T_\nu \tag{2.33}$$

where $p(\tau_e) := p_{J=1}(\tau_e)$ and

$$\begin{aligned} T_e &= \sum_{\tau_e} p(\tau_e) e_{\tau_e} \\ T_\nu &= \sum_{q_\nu, \tau_\nu} \nu^\dagger_{q_\nu, \tau_\nu} \\ T_n \Phi_Z &\propto \Phi_{Z-1} \end{aligned} \tag{2.34}$$

Here e_{τ_e} annihilates a core electron with $\tau_e = \{n_e, \kappa_e, m_e\}$, $\nu^\dagger_{q_\nu,\tau_\nu}$ creates a neutrino with q_ν and $\tau_\nu = \{\kappa_\nu\, m_\nu, a\}$, while T_n transforms the parent nuclear wavefunction of definite I_i and M_{I_i} into the daughter's wavefunction with I_f and M_{I_f}. Note it is assumed that both the parent and daughter nuclear ground state can be described in terms of a single total angular momentum quantum number I and projection M_I.

It is important to realize that for so-called *forbidden* transitions [56], which are characterized by larger exchanged angular momenta J (and a possible change of nuclear parity, i.e. $\pi_i \neq \pi_f$), T_{EC} is generally not applicable to calculate the EC spectrum, such that the general expression (2.29) must be used. A decomposition of the transition operator into a product of nuclear, electronic and neutrino part is also no longer possible if hyperfine interaction is included in the calculations. However, as we will see in chapter 3, one can nevertheless find a simple transition operator describing the most important parts similar to (2.33).

2.6 How to calculate the electron capture spectrum

As we mentioned at the beginning of this chapter, the weak interaction is small compared to the electromagnetic interactions between the atomic electrons, such that H_W is treated in first-order perturbation theory. In the time domain, H_W acts at $t = 0$ on the parent ground state $|\Psi_0\rangle$, annihilates a core electron, transforms a proton inside the nucleus into a neutron and creates a neutrino. The resulting state ends up in an excited state and starts to evolve in time due to the electromagnetic interactions between the remaining electrons. During this de-excitation process, energy is released in form of photons or electrons until the atom finally arrives at the daughter's ground state. An experimental measurement probes the so-called differential decay rate or EC spectrum $\frac{\mathrm{d}\Gamma}{\mathrm{d}\omega}(\omega)$ which corresponds to the number of decays per unit of time within the energy interval $[\omega, \omega + \mathrm{d}\omega]$ divided by the size of the interval $\mathrm{d}\omega$.

Fermi's golden rule

A common approach used by several authors, like for instance De Rújula [26, 57], Faessler [58–60] or Robertson [61], to theoretically describe the differential decay

rate is Fermi's golden rule

$$\frac{\mathrm{d}\Gamma}{\mathrm{d}\omega}(\omega) \propto \sum_f \left|\left\langle \Psi_f \left| H_W \right| \Psi_0 \right\rangle\right|^2 \delta(E_f - \omega - E_0). \tag{2.35}$$

Here the sum extends over all final states, including the nucleus, electrons and neutrino, whereas the delta-function guarantees energy conservation between initial and final state.

Atoms that undergo EC decays consist of many electrons which interact with each other due to the Coulomb forces between them. Thus, we have to deal with a correlated many-particle system, i.e. the atom's electrons cannot be treated independently from each other, leading to a ground state which is usually not representable by a single Slater-determinant. If this atom now decays by EC, a core hole is created and all the remaining electrons react to this perturbation, i.e. Coulomb interaction couples the core hole to all the other shells. Hence, the spectrum does not only involve resonances which correspond to single core hole excitations directly accessible after EC, but also to core holes in shells from which capture was neglected or to two core hole excitations with one additional electron in the valence shell [9]. Assuming a parent ground state given by a superposition of several Slater-determinants, it then becomes evident that these resonances are also given by multi-Slater-determinant-states.

In calculations based on Fermi's golden rule a set of final states included in (2.35) must be found. Here the problem is that there are infinitely many final states each carrying an infinitesimal amount of spectral weight [9]. Despite the simple form of Fermi's golden rule, it exhibits a major drawback, since it is a priori not possible to determine these multi Slater-determinant states with largest weight representing the peaks observed in the experiment. Calculations by Faessler [59] and Robertson [61] for ^{163}Ho assuming final states given by single Slater-determinants with one and two core holes, for example, predict too little spectral weight in particular for those resonances which are not directly accessible after EC.

Green's functions

A computationally more practical approach to calculate the EC spectrum, which also enables one to solve the problems associated with Fermi's golden rule, are Green's functions. It has been shown on the example of ^{163}Ho that by using

Green's functions it is not only possible to accurately determine the EC spectrum on a basis of bound states [9], but also to include unbound states [11].

One possible way to derive an expression for the EC spectrum in terms of Green's functions is to start from the causal response to H_W, which in time domain is defined by the retarded Green's function [62]

$$\begin{aligned} G(t) &= -i\Theta(t)\langle\Psi_0|[H_W^\dagger(t), H_W(0)]|\Psi_0\rangle \\ &= -i\Theta(t)\left(\langle\Psi_0|H_W^\dagger(t)H_W(0)|\Psi_0\rangle - \langle\Psi_0|H_W(0)H_W^\dagger(t)|\Psi_0\rangle\right). \end{aligned} \tag{2.36}$$

At time $t = 0$ the parent's ground state $|\Psi_0\rangle$ is subject to a perturbation, i.e. the weak interaction H_W. This perturbed state then evolves in time, until at time t it is projected on $(H_W(t)\,|\Psi_0\rangle)^\dagger$. Physically, the expression $\left\langle\Psi_0\left|H_W^\dagger(t)H_W(0)\right|\Psi_0\right\rangle$ corresponds to amplitude of finding the atom in state $H_W\,|\Psi_0\rangle$ at time t after a perturbation by H_W at $t = 0$. Applying a Fourier transform, the corresponding expression in frequency domain is given by [62]

$$\begin{aligned} G(\omega) &= \langle\Psi_0|H_W^\dagger\frac{1}{\omega - H + E_0 + \mathrm{i}\eta^+}H_W|\Psi_0\rangle - \langle\Psi_0|H_W\frac{1}{\omega + H - E_0 + \mathrm{i}\eta^+}H_W^\dagger|\Psi_0\rangle \\ &\equiv G^-(\omega) - G^+(\omega) \end{aligned} \tag{2.37}$$

where E_0 is the ground state energy of the parent atom. The positive, infinitesimal imaginary part η^+ is introduced to make the Fourier transform converge. The Hamiltonian governing the dynamics subsequent to EC is given by

$$H = H_D + H_C + H_\nu + H_P + H_A \tag{2.38}$$

and comprises besides the Dirac (H_D) and the Coulomb (H_C) part also parts describing the neutrino (H_ν) and the additional photons (H_P) as well as Auger-Meitner electrons (H_A) produced during the relaxation process. Here H_P contains the kinetic energy of the photons as well their interaction with the electrons. H_A, on the other hand, comprises the kinetic energy of the Auger-Meitner electrons and their Coulomb interaction with bound electrons. It is important to note that the difference compared to the Hamiltonian used to calculate the ground state is that the electrons move in a modified nuclear potential with charge number $Z - 1$, i.e. in the Coulomb potential of the daughter atom. After the EC decay, the neutrino can be considered as a free particle, which allows us to decouple it from the relaxation process, i.e. the Hamiltonian relevant for the dynamics takes the form

$$H \approx H_D + H_C + H_P + H_A. \tag{2.39}$$

In section 2.7 and chapter 3, H_P and H_A are neglected and the calculations are restricted to a set of bound states involving neither photons nor Auger-Meitner electrons. Chapter 4 is devoted to investigate the influence of fluorescence decay on the spectral line-shape, while the impact of Auger-Meitner decay is discussed in detail in [11, 55].

Starting from (2.37), the analog of Fermi's golden rule is obtained by employing

$$\frac{1}{\omega + \mathrm{i}\eta^+} = \mathcal{P}\frac{1}{\omega} - \mathrm{i}\pi\delta(\omega) \tag{2.40}$$

where $\mathcal{P}$ denotes the Cauchy principal value which enables us to express the differential decay rate as the negative imaginary part of the Green's function

$$\frac{\mathrm{d}\Gamma}{\mathrm{d}\omega}(\omega) \propto -\lim_{\eta^+\to 0} \mathrm{Im}\left[G^-(\omega) - G^+(\omega)\right]. \tag{2.41}$$

Note that, in order to take into account the finite lifetime of the resonances, η^+ is typically replaced by a larger (and optionally energy-dependent) number $\frac{\gamma}{2}$ thereby transforming the delta-peaks into Lorentzians. In the literature γ is usually treated as a free parameter, but can, as we will see in chapter 4 for the case of fluorescence decay, also be calculated from first principles.

If we compare (2.41) with (2.35), we immediately realize one fundamental difference: While Fermi's golden rule involves a sum over final states, this sum is transformed into the calculation of the resolvent of H projected on the parent ground state $|\Psi_0\rangle$. The resolvent is determined by expressing H on a finite many-particle basis using Lanczos algorithm [37, 38]. Here the resonances are naturally given by multi-Slater-determinants.

Another difference of the Green's function approach compared to Fermi's golden rule is that the latter resonates only at positive energy, while $G(\omega)$ has in addition to poles at positive, also poles at negative energies which correspond to so-called virtual excitations. Although experimentally not directly accessible, these excitations have tails which may extend into the positive energies thereby affecting in particular the low-energy resonances.

EC spectrum for allowed transitions

As we have discussed before, for *allowed* transitions the complicated general expression of the weak interaction (2.29) can be replaced by the simple transition operator T_{EC}, such that $G^-(\omega)$ takes the form

$$G^-(\omega) = \langle\Psi_0|T_{\mathrm{EC}}^\dagger \frac{1}{\omega - H + E_0 + \mathrm{i}\frac{\gamma}{2}} T_{\mathrm{EC}}|\Psi_0\rangle \tag{2.42}$$

where we assume $H = H_D + H_C$. By inserting unity $\mathbb{1} = \sum_f |\Psi_f\rangle \langle\Psi_f|$ where $H|\Psi_f\rangle = E_f|\Psi_f\rangle$, we obtain

$$G^-(\omega) = \sum_f \langle\Psi_0|T_{\mathrm{EC}}^\dagger \frac{|\Psi_f\rangle\langle\Psi_f|}{\omega - E_f + E_0 + \mathrm{i}\frac{\gamma}{2}} T_{\mathrm{EC}}|\Psi_0\rangle. \tag{2.43}$$

Here, the sum $\sum_f$ includes all possible neutrino and electronic final states. Note, however, that it contains no sum over all nuclear final states, since we assume the parent and daughter nucleus to be characterized by a single total angular momentum quantum number I and projection M. As the neutrino can be regarded as a free particle, we separate the sum over the neutrino's degrees of freedom from the rest

$$G^-(\omega) = \sum_{q_\nu,\tau_\nu} \delta(Q - \omega - E_\nu) \sum_{\psi_{\tau_e}(f)} \langle\Psi_0|T_{\mathrm{EC}}^\dagger \frac{|\Psi_f\rangle\langle\Psi_f|}{\omega - E_f + E_0 + \mathrm{i}\frac{\gamma}{2}} T_{\mathrm{EC}}|\Psi_0\rangle \tag{2.44}$$

where it is used that Q is shared between the neutrino and electronic excitations, such that $E_\nu = Q - \omega$. Due to the weak coupling of the individual sectors, the final states can be written as a product of nuclear, electronic and neutrino part $|\Psi_f\rangle \approx |\Phi_{Z-1}\rangle \otimes |\psi_{\tau_e}(f)\rangle \otimes |q_\nu, \tau_\nu\rangle$. Thus, the nuclear and neutrino matrix elements for an initial state of the form (2.32) are explicitly given by

$$\begin{aligned} &\langle\Phi_{Z-1}|T_n|\Phi_Z\rangle \propto 1 \\ &\langle q_\nu, \tau_\nu|T_\nu|0_\nu\rangle = \sum_{q'_\nu,\tau'_\nu} \underbrace{\langle q_\nu, \tau_\nu|q'_\nu, \tau'_\nu\rangle}_{=\delta_{q_\nu q'_\nu}\delta_{\tau_\nu\tau'_\nu}} = 1 \end{aligned} \tag{2.45}$$

where $T_\nu = \sum_{q'_\nu,\tau'_\nu} \nu^\dagger_{q'_\nu,\tau'_\nu}$. In consequence, nuclear and neutrino parts can be fully decoupled from the dynamics subsequent to EC and the calculation of $G(\omega)$ is reduced to the determination of the resolvent solely involving the electronic degrees of freedom. As a next step, we transform the sum over the neutrino's momentum into an integral

$$\sum_{q_\nu} \propto \int_0^\infty \mathrm{d}E_\nu E_\nu \sqrt{E_\nu^2 - m_\nu^2}. \tag{2.46}$$

Employing the delta function $\delta(Q - \omega - E_\nu)$ in (2.44) this integral is easily evaluated such that the differential decay rate can be expressed in the following form

$$\begin{aligned} \frac{\mathrm{d}\Gamma}{\mathrm{d}\omega}(\omega) \propto -\mathrm{Im} \sum_{a=1}^{3} |U_{ae}|^2 (Q - \omega) \sqrt{(Q-\omega)^2 - m_a^2} \\ \times \left[\langle\psi_0|T_e^\dagger \frac{1}{\omega - H + E_0 + \mathrm{i}\frac{\gamma}{2}} T_e|\psi_0\rangle - \langle\psi_0|T_e^\dagger \frac{1}{\omega + H - E_0 + \mathrm{i}\frac{\gamma}{2}} T_e|\psi_0\rangle \right]. \end{aligned} \tag{2.47}$$

Hence, the EC spectrum can be written as the product of neutrino phase-space factor and resolvent projected on the state after EC, $T_e|\psi_0\rangle$. The EC spectrum is calculated using the Lanczos algorithm implemented in the quantum many-body script language Quanty [51, 52].

2.7 Electron capture spectra for some selected isotopes

We now apply the derived expression for the Green's function (2.47) and calculate EC spectra for some selected isotopes (^{55}Fe, ^{65}Zn, ^{71}Ge, ^{118}Te, ^{131}Cs, ^{140}Nd, ^{165}Er) that undergo *allowed* transitions.

Some of the listed isotopes are already accepted or potential candidates for medical applications (^{55}Fe [63], ^{71}Ge [36], ^{131}Cs [64], ^{140}Nd [36], ^{165}Er [33]), while others (^{118}Te, ^{65}Zn) are interesting from a metrological point of view. ^{65}Zn, for instance, has been investigated in the MetroMMC project [65] which pursued the main goal to determine the fundamental decay data of some EC isotopes.

According to [66] all presented isotopes (except ^{65}Zn) decay solely by EC. For ^{65}Zn an additional β^+ transition has been observed [65] leading to a continuous background spectrum. Furthermore, some of these isotopes involve different decay branches including besides the nuclear ground-to-ground-state transition also transitions into excited nuclear states which subsequently decay by emitting γ-rays. The spectra displayed below include only the nuclear ground-to-ground-state branch.

All spectra displayed in Fig. 2.2 are normalized to their corresponding half-lives, i.e. the integral after normalization amounts to $\frac{1}{2}$. The corresponding Q-values are taken from [67].

The spectral features can be understood by the different decay channels into bound states following the decay by EC. These have been discussed in detail on the example of ^{163}Ho [9] and can be transferred one-to-one to the spectra displayed in Fig. 2.2. In the following, we briefly explain the essential spectral features as well as the corresponding relaxation channels. For a more detailed explanation we refer to [9].

Since we are looking at *allowed* decays, electrons can be captured from the $ns_{1/2}$ or $np_{1/2}$ orbitals. If we would turn off the atomic relaxation directly after the capture of an electron, the resulting EC spectrum would be solely given by the main

resonances, i.e. the many-particle states with one core hole in the orbital from which an electron has been captured. Some of these resonances with single core hole in the $1s, 2s, 2p$ and $3s$ shells are indicated in the spectra presented below.

If atomic relaxation is allowed, different decay processes occur. The most simple relaxation channel originates from the modified nuclear potential. As the $ns_{1/2}$ ($np_{1/2}$) orbitals of the parent atom are not orthogonal in the nuclear potential of the daughter atom, different $ns_{1/2}$ ($np_{1/2}$) can mix. However, due to angular momentum conservation, these scattering processes do not lead to additional states, but only affect the intensity and position of the resonances already accessible directly after EC.

More complicated decay processes involving different orbitals occur as soon as the Coulomb interaction couples the created core hole to all the other atomic shells. As the Coulomb interaction conserves total angular momentum and parity on a many-particle level, but not necessarily for individual electrons, additional resonances with core holes in shells from which no capture was possible, appear. Typically, these resonances are lower in intensity than the main peaks and are found at the excitation energies of $np_{3/2}$, $nd_{3/2}$, ... orbitals. As there are various possible configurations at different energies compatible with the angular momentum and parity selection rules, the resonances are split into multiplets.

In addition to the single core hole excitations, double core hole excitations emerge where one additional electron is scattered into the valence shell. Double core hole excitations are typically prominent to the right of a main resonance.

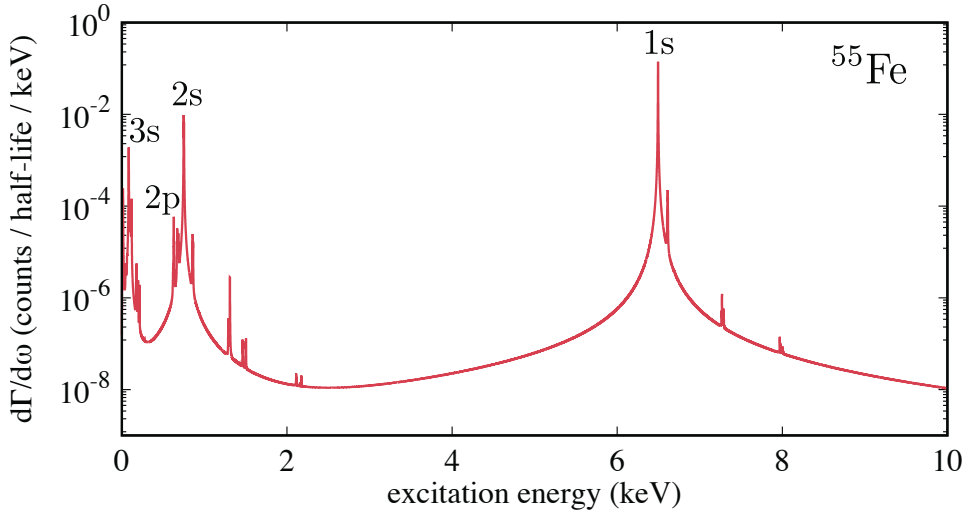

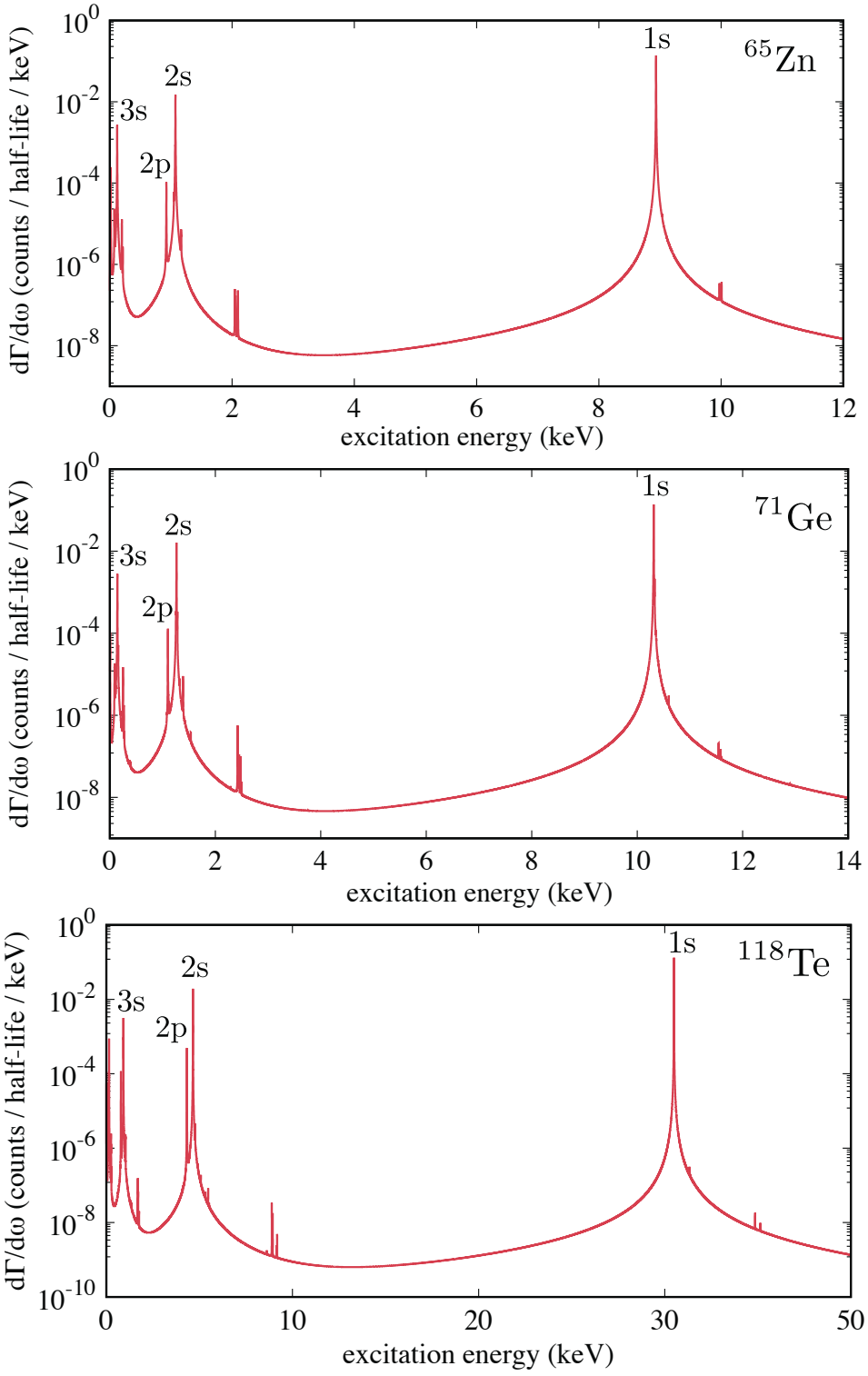
dΓ/dω (counts / half-life / keV)
excitation energy (keV)
1s
2s
3s
2p
65Zn
71Ge
118Te

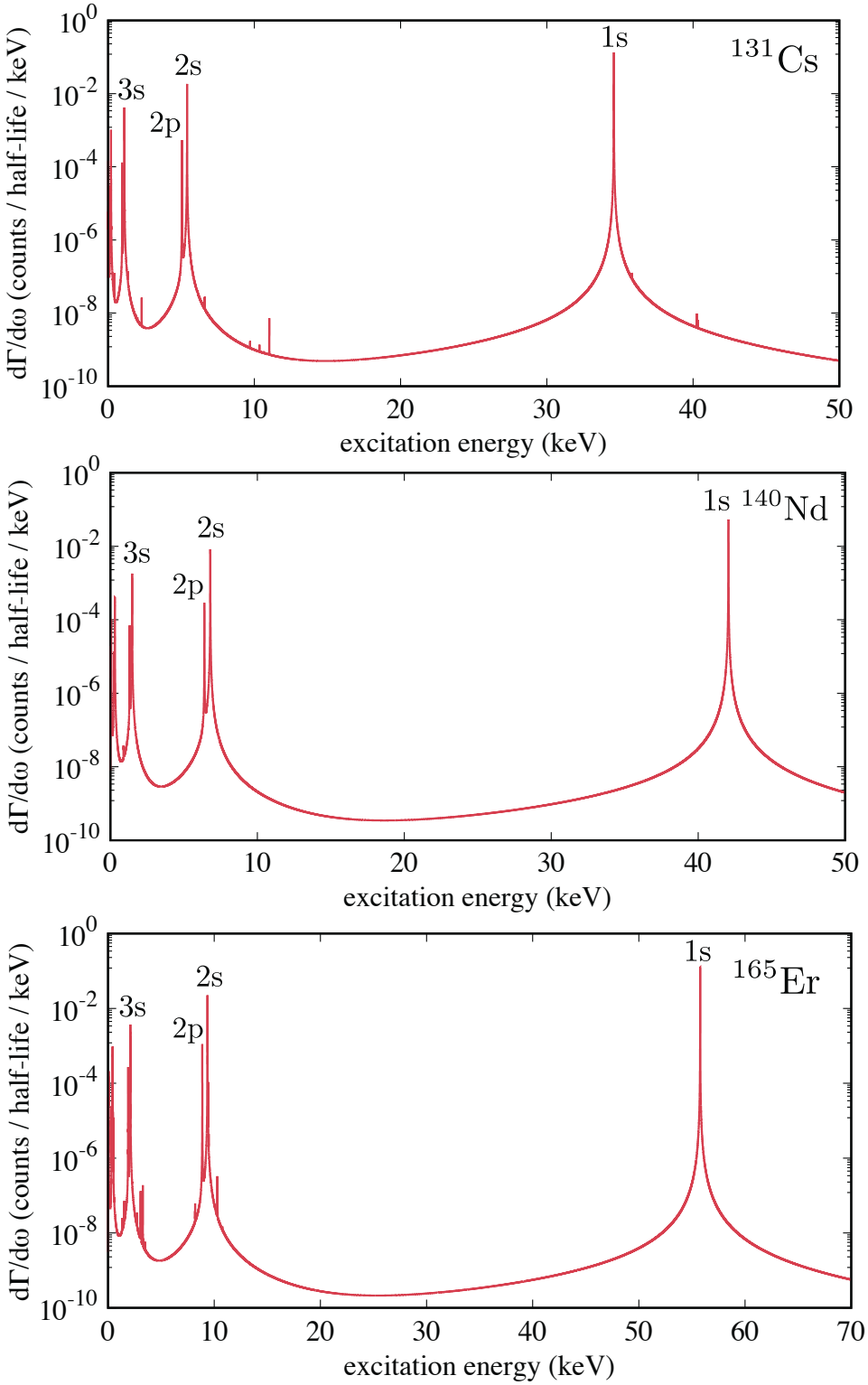

Figure 2.2: Nuclear ground-to-ground-state EC decay spectra of ^{55}Fe, ^{65}Zn, ^{71}Ge, ^{118}Te, ^{131}Cs, ^{140}Nd and ^{165}Er calculated by using (2.47) for a Lorentzian broadening of $\gamma = 2$ eV. The labeling indicates some of the main resonances with single core holes in the $1s$, $2s$, $2p$ and $3s$ shell.

3 How hyperfine interaction affects the nuclear decay by electron capture

For a long time starting from the discovery of radioactivity by Becquerel in 1896 [2], nuclear decay rates were assumed to be constant, i.e. independent of the chemical and physical environment they are exposed [68]. However, this was predominantly based on studies of alpha- and beta-decays which do not exhibit a significant dependence on environmental factors [68]. Nuclear decay by EC, on the other hand, constitutes a special case, since the nuclear decay rate here is proportional to the electronic density at the nucleus. This, in turn, is affected by several external factors like the chemical environment, temperature or pressure the atom is exposed to. Therefore, a change of these factors has an impact on the nuclear decay rate. First ideas of this kind were originally developed by Segré [69] and Daudel [70] in the late 1940s and have since been further developed by many scientists not only to gain better understanding of nuclear decays in general, but also to more accurately describe explicit reactions.

Since then, ^{7}Be has established, in particular due to its simple electronic structure ($1s^2 2s^2$), as the most prominent example on which the impact of environmental effects of different host materials, temperature and pressure on the nuclear decay rate have been investigated both experimentally and theoretically [68, 69, 71–74]. A particularly large effect on the decay rate/half-life in the case of Be has been observed for ^{7}Be encapsulated in the fullerene C_{60} (^{7}Be@C_{60}). At room temperature the half-life of ^{7}Be embedded in metallic Be is 0.83% faster than the one in ^{7}Be@C_{60} [72]. The authors assigned the origin of this effect to the modified electron density at the nucleus. Due to the delocalization of the 2s electrons in the case of ^{7}Be in metallic Be, the electron density at the nucleus is slightly reduced compared to ^{7}Be@C_{60} where the 2s electrons are assumed to be localized. If ^{7}Be@C_{60} is cooled down to 5 K, the radioactive speedup is even enhanced and amounts to 1.5% [73].

An intriguing alternative to the aforementioned options to manipulate nuclear decay rates is to change the initial hyperfine state of the atom. This possibility has to our knowledge first been discussed by Folan and Tsifrinovich [75]. The authors

could show using a simple model consisting of an atomic nucleus and an unfilled (valence) *s*-shell that the decay rate strongly depends on the relative orientation of nuclear and valence spins, i.e. on the initial hyperfine state, at temperatures small compared to the hyperfine splitting. Furthermore, they addressed the origin of this effect to conservation of total angular momentum. A realistic physical system best resembling this simple model are hydrogenlike ions. On the example of hydrogen- and heliumlike ^{140}Pr ions the hyperfine interaction dependence of the decay rate has been investigated experimentally [76]. Although hydrogenlike ^{140}Pr ions have only a single electron, i.e. one electron less than heliumlike ^{140}Pr ions, their decay rate is enhanced by about 50%. This is a quite surprising observation, since one would naively expect that in the case of two electrons being captured, the decay rate would be larger than in the case of only a single electron. A theoretical description by Patyk et al. [77] could confirm the experimental observation and attribute the origin of this effect to hyperfine interaction and the associated conservation of total angular momentum.

However, both the simple model by Folan and Tsifrinovich [75] as well as the more general theoretical description by Patyk et al. [77] discuss only the effect of hyperfine interaction on the decay rate in the context of hydrogen- and/or heliumlike ions. An extension to the general case of charge neutral atoms is missing. Its development is the goal of this chapter.

In section 3.1, we start by introducing the hyperfine interaction Hamiltonian. Then, in section 3.2, we briefly discuss an effective transition operator which allows us to describe *allowed* EC decays where nucleus and electrons are initially coupled by hyperfine interaction. Afterwards, the mechanism leading to the hyperfine interaction dependent decay rate is explained using a simple model which resembles that of Folan and Tsifrinovich [75]. In section 3.4, we consider the impact of hyperfine interaction on the nuclear decay by EC in atomic ^{163}Ho and ^{163}Ho embedded in Gold, respectively. The latter reflects the experimental situation realized in the ECHo experiment [28]. For atomic ^{163}Ho, which is the content of section 3.4.1, the EC spectra and lifetimes of all possible initial hyperfine states are calculated. In the case of ^{163}Ho embedded in Gold, discussed in section 3.4.2, we outline an approach capable of experimentally resolving the spectral differences that result from the different hyperfine states. In this context, we present EC spectra and lifetimes calculated for different temperatures. The chapter ends with an conclusion including a summary of the main results.

3.1 Hyperfine interaction

Hyperfine interaction describes the electromagnetic interaction of the atomic electrons with the higher-order nuclear multipole moments and is typically an effect on the sub-meV scale [78]. It is convenient to express the hyperfine interaction Hamiltonian in terms of a scalar product of two spherical tensor operators [46]:

$$H_{\mathrm{HF}} = \frac{e}{4\pi} \sum_{k} \sum_{\lambda=-k}^{k} (-1)^{\lambda} T^{k}_{\lambda} \mathcal{T}^{k}_{-\lambda} \tag{3.1}$$

Here, T^{k}_{λ} and $\mathcal{T}^{k}_{-\lambda}$ are the components of rank-k irreducible tensor operators acting on the electronic and nuclear spin and spatial degrees of freedom, respectively. Multipoles with even k correspond to electric interactions, while those with odd k to the magnetic ones. The term with $k = 0$ represents the electric monopole part and is not included in the hyperfine interaction Hamiltonian, because it equally shifts the levels within a given configuration.

The dominant part in (3.1) originates from the dipole interaction of the electric and magnetic moment ($k = 1$) and from the interaction of the electric field gradient with the nuclear quadrupole charge distribution ($k = 2$). Higher-order multipoles are usually neglected, as they are about eight orders of magnitude smaller with respect to the dipole and quadrupole [78]. Restricting the multipole expansion to these two multipoles we explicitly find [46]

$$\begin{aligned} H_{\mathrm{HF}} &= H_{\mathrm{M}} + H_{\mathrm{E}} \\ &= \frac{e}{4\pi} \left\{ \sum_{\lambda=-1}^{1} (-1)^{\lambda} \underbrace{\frac{i\sqrt{2}\left[\boldsymbol{\alpha} \cdot \mathbf{C}^{(0)}_{1\lambda}(\hat{r})\right]}{r^2} \mu_{-\lambda}}_{= T^{1}_{\lambda} \mathcal{T}^{1}_{-\lambda}} + \sum_{\lambda=-2}^{2} (-1)^{\lambda} \underbrace{\frac{C^{2}_{\lambda}(\hat{r})}{r^3} Q_{-\lambda}}_{= T^{2}_{\lambda} \mathcal{T}^{2}_{-\lambda}} \right\}. \end{aligned} \tag{3.2}$$

The first term corresponds to the magnetic dipole and is given by the scalar product of two rank-1 irreducible tensor operators, $\boldsymbol{\alpha} \cdot \mathbf{C}^{(0)}_{1\lambda}(\hat{r})$ and $\mu_{-\lambda}$. The former acts on the electronic part and is composed of a renormalized vector spherical harmonic $\mathbf{C}^{(0)}_{1\lambda}(\hat{r})$ and the Dirac matrix $\boldsymbol{\alpha}$ (2.10). A definition of the (renormalized) vector spherical harmonic $\mathbf{C}^{(0)}_{1\lambda}(\hat{r})$ can be found in [47]. The operator $\mu_{-\lambda}$ acts on the nuclear degrees of freedom and characterizes the nuclear magnetic moment.

The second term in the above expression describes the electric quadrupole part of the hyperfine interaction. It is determined by the scalar product of the nuclear

quadrupole tensor Q_λ and the renormalized spherical harmonic $C^2_\lambda(\hat{r})$. As this part is proportional to r^{-3}, it is very sensitive to the electronic density close to the nucleus. Therefore, quadrupole interactions are large and typically exceed the magnetic dipole for atoms with an open s-shell where the radial wavefunction is large at the origin.

The presence of a non-vanishing hyperfine interaction leads to the coupling of the electronic **J** and nuclear **I** angular momentum to a conserved total angular momentum $\mathbf{F} = \mathbf{J} + \mathbf{I}$. Eigenstates of defined **F** are found by coupling the states $|J, M_J\rangle$ and $|I, M_I\rangle$ to $|F, M_F\rangle$

$$|F, M_F\rangle = \sum_{M_J, M_I} C^{FM_F}_{JM_J IM_I} |J, M_J\rangle \otimes |I, M_I\rangle \tag{3.3}$$

with Clebsch-Gordan coefficients $C^{FM_F}_{JM_J IM_I}$. Here, J, I and F denote the quantum numbers of the total electronic, nuclear and coupled angular momentum, respectively. Their corresponding magnetic quantum numbers are labeled by M_J, M_I and M_F.

To determine the relative size of the magnetic dipole and electric quadrupole part, we evaluate the expectation value of $H_{\mathrm{HF}} = H_{\mathrm{M}} + H_{\mathrm{E}}$ in the state $|F, M_F\rangle$ for each term separately, i.e.

$$\Delta E_F = \langle F, M_F | H_{\mathrm{M}} | F, M_F \rangle + \langle F, M_F | H_{\mathrm{E}} | F, M_F \rangle \tag{3.4}$$

which corresponds to the energy shifts due to the magnetic dipole and electric quadrupole, respectively. Following the steps presented in [46], the energy corrections can finally be written as

$$\Delta E_F = \frac{1}{2} aK + \frac{1}{2} \frac{3K(K+1) - 4J(J+1)I(I+1)}{2I(2I-1)2J(2J-1)} b \tag{3.5}$$

where $K = F(F+1) - I(I+1) - J(J+1)$. Here a and b denote the magnetic dipole and electric quadrupole hyperfine constants which are explicitly given by [46]

$$\begin{aligned} a &= \frac{\mu}{I \cdot J} \langle JJ | T^1_0 | JJ \rangle \\ b &= 2Q \langle JJ | T^2_0 | JJ \rangle \end{aligned} \tag{3.6}$$

where μ and Q are the nuclear magnetic and quadrupole moment, respectively. For ^{163}Ho, the experimental values of μ and Q amount to $a_{\mathrm{exp}} = (3.35 \pm 0.03) \cdot$

10^{-6} eV and $b_{\text{exp}} = (-7.14 \pm 1.32) \cdot 10^{-6}$ eV [79] which enables us to estimate the respective energy splittings. For Holmium (implanted in Gold) which will be discussed later on (see sections 3.4.1 and 3.4.2), the energy splitting due to the magnetic dipole is $\sim 10^{-4}$ eV while that of the electric quadrupole amounts to $\sim 10^{-6}$ eV. Thus, the latter is reduced by roughly two orders of magnitude which justifies to neglect the electric quadrupole part and to set $H_{\text{HF}} \equiv H_{\text{M}}$.

Compared to the electronic states of an atom, the energy difference between two nuclear states typically is very large ($\sim 10^3$ keV). As a result, the mixing of configurations with different I becomes very unlikely such that the total nuclear angular momentum can be regarded as a good quantum number. Due to the smallness of the hyperfine interaction, we can in a first approximation also assume J to be a good quantum number [80]. Within this approximation the magnetic dipole term is given by the effective interaction

$$H_{\text{HF}} = a\mathbf{I} \cdot \mathbf{J}. \tag{3.7}$$

This expression leads to the same energy splitting as shown in (3.5) for $b = 0$.

3.2 An effective transition operator

In section 2.7, we presented EC spectra for selected isotopes that *allowed* decays. In this case, the application of a very simple transition operator (2.33) given by a product of nuclear, electronic and neutrino part was possible. Including hyperfine interaction, however, nuclear and electronic sector can exchange angular momentum, such that this decoupling is not allowed any more. In the following, we therefore introduce an effective transition operator capable of describing this angular momentum exchange. Using this transition operator instead of the complicated general form of the weak interaction (2.29) allows us to describe the EC spectrum for different initial hyperfine states in a very simple fashion.

As the nuclear decay by EC involves not only single nucleons but the nucleus as a whole, we seek for a transition operator acting on the many-nucleon states characterized by the total nuclear angular momentum I and z-component M_I. In the case of ^{163}Ho, the nucleus is described a total angular momentum of $I_{\text{Ho}} = 7/2$ and negative parity [81]. ^{163}Ho undergoes an *allowed* EC transition to ^{163}Dy with nuclear angular momentum $I_{\text{Dy}} = 5/2$ and negative parity. As we have seen in chapter 2, the total angular momentum exchanged in an EC decay is determined by the nuclear total angular momenta of the participating nuclei and can take the

values $|I_{\mathrm{Ho}} - I_{\mathrm{Dy}}|, \ldots, I_{\mathrm{Ho}} + I_{\mathrm{Dy}} = 1, \ldots, 6$. Restricting the decay to the lowest possible value $|I_{\mathrm{Ho}} - I_{\mathrm{Dy}}| = 1$, generally the most important contribution, and neglecting neutrinos with $l_\nu > 0$, a suitable effective transition operator is given by:

$$T = \mathbf{I} \cdot \mathbf{J}_{\mathrm{lep}} \tag{3.8}$$

Here, $\mathbf{I}$ and $\mathbf{J}_{\mathrm{lep}}$ are the total angular momentum vectors of nucleus and leptons, respectively. Note that $\mathbf{J}_{\mathrm{lep}}$ is a composite operator creating an electron-neutrino while simultaneously annihilating a core electron. Further note that the action of $\mathbf{I}$ is restricted to the part which transfers the initial many-nucleon state $|I, M_I\rangle_{\mathrm{Ho}}$ into the final state characterized by $|I, M_I\rangle_{\mathrm{Dy}}$.

Expressing T in terms of ladder operators we find:

$$T = \frac{1}{2}\left(I^+ J^-_{\mathrm{lep}} + I^- J^+_{\mathrm{lep}}\right) + I^z J^z_{\mathrm{lep}} \tag{3.9}$$

As the weak interaction conserves the total angular momentum, the change of nuclear angular momentum is compensated by the leptonic part which takes the form

$$\begin{aligned} J^+_{\mathrm{lep}} &= \frac{1}{2}\sum_{\tau_e, q_\nu} p(\tau_e) e_{\tau_e,\downarrow} \nu^\dagger_{q_\nu,\uparrow} \\ J^-_{\mathrm{lep}} &= \frac{1}{2}\sum_{\tau_e, q_\nu} p(\tau_e) e_{\tau_e,\uparrow} \nu^\dagger_{q_\nu,\downarrow} \\ J^z_{\mathrm{lep}} &= \frac{1}{2}\sum_{\tau_e, q_\nu} p(\tau_e)\left(e_{\tau_e,\uparrow}\nu^\dagger_{q_\nu,\uparrow} - e_{\tau_e,\downarrow}\nu^\dagger_{q_\nu,\downarrow}\right). \end{aligned} \tag{3.10}$$

Here $e_{\tau_e,\uparrow/\downarrow}$ annihilates an electron with quantum numbers $\tau_e = \{n_e, l_e, j_e\}$ and corresponding (relative) capture probability $p(\tau_e)$ defined by (2.30). For an exchanged angular momentum of $|I_{\mathrm{Ho}} - I_{\mathrm{Dy}}| = 1$ and $l_\nu = 0$ we can infer from conservation of total angular momentum that electron capture is only possible from the $ns_{1/2}$ and $np_{1/2}$ orbitals with non-vanishing overlap at the nucleus. For ^{163}Ho, this are the ten orbitals with $\{n_e, l_e, j_e\} \in \{1s_{1/2}, \ldots, 6s_{1/2}, 2p_{1/2}, \ldots, 5p_{1/2}\}$ [9]. Explicit values of the capture probabilities $p(\tau_e)$ can be found in the appendix of [9]. To keep notation short, the z-component of total angular momentum is abbreviated by $\uparrow$ and $\downarrow$ for $\pm 1/2$, respectively. The operator $\nu^\dagger_{q_\nu,\uparrow/\downarrow}$, on the other hand, creates a neutrino with momentum q_ν, quantum numbers $l_\nu = 0$, $j_\nu = 1/2$ and spin-up or spin-down. Note that we omit the mass-eigenstates in the description of the neutrino to keep the notation compact. Hence, the full transition operator

equivalent to the compact version (3.8) can finally be written as

$$T = \frac{1}{2} \sum_{\tau_e, q_\nu} p(\tau_e) \Big[I^+ e_{\tau_e,\uparrow} \nu^\dagger_{q_\nu,\downarrow} + I^- e_{\tau_e,\downarrow} \nu^\dagger_{q_\nu,\uparrow} + I^z \left(e_{\tau_e,\uparrow} \nu^\dagger_{q_\nu,\uparrow} - e_{\tau_e,\downarrow} \nu^\dagger_{q_\nu,\downarrow} \right) \Big]. \tag{3.11}$$

In contrast to the case for which we neglected hyperfine interaction, the transition operator T can no longer be written as a product of nuclear, electronic and neutrino part. Therefore, it is necessary to discuss its action on an initial state coupled by hyperfine interaction and the implications for the form of the equations we use to describe the EC spectrum. Let us assume a parent ground state of the form $|\Psi_0\rangle = |\Psi_0'\rangle \otimes |0_\nu\rangle$ where $|\Psi_0'\rangle$ comprises the coupled nuclear and electronic part and where $|0_\nu\rangle$ denotes the neutrino vacuum. After nuclear decay by EC, the neutrino can be regarded as a free particle, such that the final states are given by $|\Psi_f\rangle \approx |\Psi_f'\rangle \otimes |\tau_\nu, q_\nu\rangle$. Hence, the matrix element $\langle \Psi_f | T | \Psi_0 \rangle$ can be written as

$$\begin{aligned} \langle \Psi_f | T | \Psi_0 \rangle &\propto \langle \Psi_f' | \otimes \langle \tau_\nu, q_\nu | \left(I^+ e_{\tau_e,\uparrow} | \Psi_0' \rangle \otimes \nu^\dagger_{q_\nu',\downarrow} | 0_\nu \rangle + \dots \right) \\ &= \langle \Psi_f' | I^+ e_{\tau_e,\uparrow} | \Psi_0' \rangle \underbrace{\langle \tau_\nu, q_\nu | \nu^\dagger_{q_\nu',\downarrow} | 0_\nu \rangle}_{= \delta_{q_\nu q_\nu'} \delta_{m_{s_\nu}\downarrow}} + \dots \end{aligned} \tag{3.12}$$

where we assume a fixed set of quantum numbers τ_e and a neutrino with momentum q_ν and spin-component m_{s_ν}. Similar expressions are found for the matrix elements of the remaining two terms in the above sum. Consequently, the neutrino can be decoupled from the atomic relaxation process similar to the case where hyperfine interaction has been neglected. Following the steps presented in section 2.6, the EC spectrum for an initial state $|\Psi_0\rangle = |F, M_F\rangle \otimes |0_\nu\rangle$ coupled by hyperfine interaction takes the form:

$$\begin{aligned} \frac{\mathrm{d}\Gamma}{\mathrm{d}\omega} \propto -\mathrm{Im}\,(Q-\omega) \sqrt{(Q-\omega)^2 - m_\nu^2} \Big[&\langle F, M_F | T^\dagger \frac{1}{\omega - H_{\mathrm{Dy}} + E_{\mathrm{Ho}} + \mathrm{i}\frac{\gamma}{2}} T | F, M_F \rangle \\ &- \langle F, M_F | T^\dagger \frac{1}{\omega + H_{\mathrm{Dy}} - E_{\mathrm{Ho}} + \mathrm{i}\frac{\gamma}{2}} T | F, M_F \rangle \Big] \end{aligned} \tag{3.13}$$

Here, $H_{\mathrm{Dy}} = H_D + H_C$ comprises the Dirac Hamiltonian and the Coulomb interaction in the nuclear potential of the Dy atom. Note that T is understood as the part of the transition operator acting only on the nuclear and electronic degrees of freedom.

3.3 Simple model

The simultaneous presence of an open core and valence shell, an atomic nucleus and a neutrino makes the nuclear decay by EC an overall complicated process. To gain better understanding it is essential to disentangle the interplay of all participating angular momenta.

Vanishing hyperfine interaction

For this reason, let us start with a simple model consisting of a half-filled valence s-shell with one spin-up electron and a completely filled core s-shell as is shown in Fig. 3.1 on the left. The atomic nucleus is regarded as a spectator, i.e. the coupling of its angular momentum to that of the valence due to hyperfine interaction is neglected. As the angular momentum of the valence shell is zero, the initial state is solely characterized by its spin, i.e. $S_{\mathrm{val}} = 1/2,\ M_{\mathrm{val}} = 1/2$, where M_{val} denotes the magnetic quantum number associated to S_{val}.

After capture of one core electron, the atom ends up in a state with two open shells. To stay simple, we restrict our considerations to the sub-space of singly occupied core- and valence shells. The Coulomb repulsion between the two shells can be divided into a direct and an exchange part. While the latter depends on the spin-direction of the captured electron, the former leads to the same repulsion irrespective of the spin and thus will be neglected. In this case the Coulomb interaction between the (remaining) core and valence electron can be expressed as [82]

$$H_{\mathrm{SM}} = -J_{\mathrm{H}}\, \mathbf{S}'_{\mathrm{core}} \cdot \mathbf{S}'_{\mathrm{val}}. \tag{3.14}$$

Here, $J_{\mathrm{H}} > 0$ is the Hund's exchange constant and $\mathbf{S}'_{\mathrm{core}}$ and $\mathbf{S}'_{\mathrm{val}}$ are the spin (vectors) of core and valence shell, respectively. Here and in the following, all primed angular momenta and their corresponding quantum numbers refer to the final states, i.e. the states after EC.

Imagine that only the electron with spin anti-parallel to the spin of the valence electron is captured. Then, the final state is given by the spin-triplet ($S' = 1,\ M'_S = 1$)

$$\psi_{1,1} = |\uparrow'_{\mathrm{val}}\rangle \otimes |\uparrow'_{\mathrm{core}}\rangle \tag{3.15}$$

resulting in a single peak at energy $E_{\mathrm{T}} = -1/4\ J_{\mathrm{H}}$ as is shown in Fig. 3.1. If, on the other hand, only the electron with spin parallel with respect to the valence is captured, the atom ends up in a state with anti-parallel core- and valence spin.

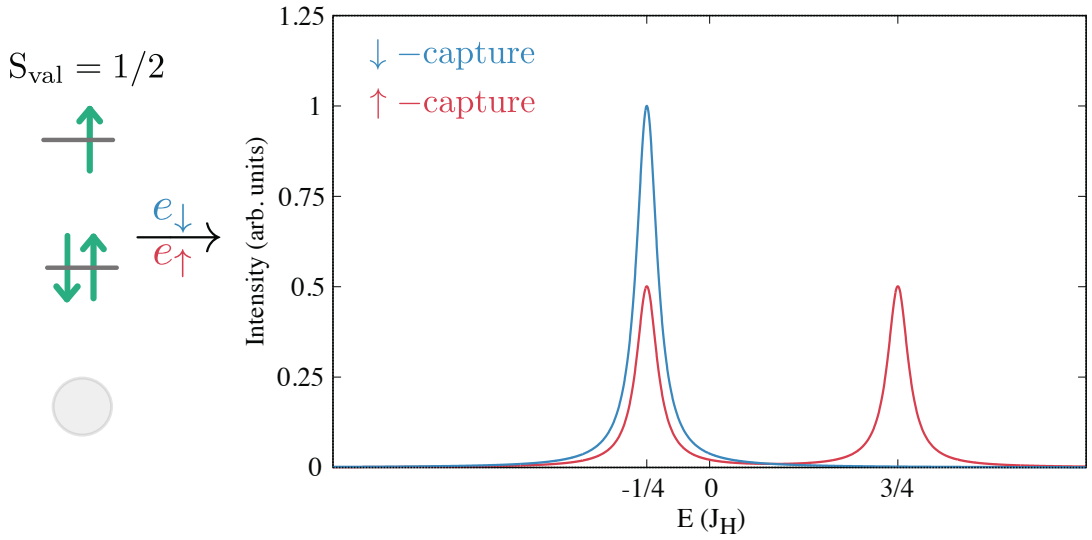

Figure 3.1: Spectra for capture of spin parallel (spin-up) and anti-parallel (spin-down) with respect to the valence spin as a function of the Hund's exchange constant J_H. The capture of a spin-down electron results in a final state given by a superposition of spin-triplet at energy $E_T = -1/4\ J_H$ and spin-singlet at energy $E_S = 3/4\ J_H$. The capture of an spin-down electron, on the other hand, results in a pure spin-triplet state. The nucleus is regarded as a spectator.

This state, however, is not an eigenstate of H_{SM} resulting in a final state which is given by a superposition of spin-triplet ($S' = 1,\ M'_S = 0$)

$$\psi_{1,0} = \sqrt{\frac{1}{2}} \left(|\uparrow'_{val}\rangle \otimes |\downarrow'_{core}\rangle + |\downarrow'_{val}\rangle \otimes |\uparrow'_{core}\rangle \right) \tag{3.16}$$

and spin-singlet ($S' = 0,\ M'_S = 0$)

$$\psi_{0,0} = \sqrt{\frac{1}{2}} \left(|\uparrow'_{val}\rangle \otimes |\downarrow'_{core}\rangle - |\downarrow'_{val}\rangle \otimes |\uparrow'_{core}\rangle \right) \tag{3.17}$$

with Clebsch-Gordan coefficients $\pm\sqrt{\frac{1}{2}}$. As the red curve in Fig. 3.1 illustrates, the spectrum is given by two peaks with equal spectral weight at energies $E_T = -1/4\ J_H$ and $E_S = 3/4\ J_H$. According Hund's rules, parallel orientation of core and valence spin is energetically favorable as two electrons with the same spin-direction try to avoid each other due to the Pauli principle. In addition, the spin-triplet has an anti-symmetric spatial wave function for which the probability to find two electrons at the same position is reduced leading to a gain in Coulomb

energy and finally to an overall lower energy [83]. It is important to realize that the energy difference between triplet and singlet is solely determined by the exchange constant J_{H} , i.e. Coulomb interaction.

Non-vanishing hyperfine interaction

Fig. 3.1 reveals that the spectrum for spin-up and spin-down capture differs in the number of peaks and their intensity. In a realistic scenario, however, spin-up and spin-down electrons are always captured with equal probability. Consequently, the spin-dependence cannot be resolved in an experimental measurement. However, our model has so far ignored an important part. In reality, nuclear decay always involves an atomic nucleus which actively participates in the decay process. To take this into account, we extend the simple model by a nucleus and from now on consider a nucleus-electron system coupled by hyperfine interaction. For simplicity, we assume a parent nuclear angular momentum of $I = 1$ which decays by EC to a daughter nuclide with $I' = 0$. Now the interesting question is if the more realistic nucleus-electron model is capable of resolving the aforementioned differences, i.e. either to observe a decay into two or just a single state.

Due to the hyperfine interaction, $\mathbf{I}$ and $\mathbf{S}_{\mathrm{val}} (= \mathbf{J}_{\mathrm{val}})$ are coupled to the total angular momentum $\mathbf{F}$ which can take the values $F = 1/2$ and $F = 3/2$ where we assume $L_{\mathrm{val}} = 0$ and $S_{\mathrm{val}} = 1/2$ as is indicated in Fig. 3.2 on the left. Without loss of generality, we consider in the following the two sub-states $|F = 3/2, M_F = 3/2\rangle$ and $|F = 1/2, M_F = 1/2\rangle$ as the representatives for parallel and anti-parallel valence- and nuclear angular momentum, respectively. In terms of the uncoupled basis these states are given by

$$\left|\frac{1}{2}', \frac{1}{2}\right\rangle = \sqrt{\frac{2}{3}} \left|1_{\mathrm{nuc}}\right\rangle \otimes \left|\downarrow_{\mathrm{val}}\right\rangle - \sqrt{\frac{1}{3}} \left|0_{\mathrm{nuc}}\right\rangle \otimes \left|\uparrow_{\mathrm{val}}\right\rangle \tag{3.18}$$

with Clebsch-Gordan coefficients $\sqrt{\frac{2}{3}}$ and $-\sqrt{\frac{1}{3}}$ and

$$\left|\frac{3}{2}', \frac{3}{2}\right\rangle = \left|1_{\mathrm{nuc}}\right\rangle \otimes \left|\uparrow_{\mathrm{val}}\right\rangle \tag{3.19}$$

where we characterize these states by the z-component of the nuclear and valence angular momentum.

The initial state decays by EC into states containing a core-hole with $S'_{\mathrm{core}} = 1/2$, a valence electron $S'_{\mathrm{val}} = 1/2$, an electron-neutrino with $S'_{\nu} = 1/2$ and a

nucleus with I' where one proton has been transformed into a neutron. Due to conservation of $\mathbf{F}$, the final states can be found by re-coupling the four angular momenta to the initial $|F, M_F\rangle$. Since in our example the nucleus can only decay into a single state $|I' = 0, M_I' = 0\rangle$, the angular momentum coupling simplifies to the coupling of three angular momenta $\mathbf{S}'_{\text{val}}, \mathbf{S}'_{\text{core}}$ and $\mathbf{S}'_\nu$. One should realize that the coupling order is not unique, as one can first combine $\mathbf{S}'_{\text{val}}$ and $\mathbf{S}'_{\text{core}}$ to $\mathbf{S}'$ and afterwards $\mathbf{S}'$ and $\mathbf{S}'_\nu$ to $\mathbf{F}$, or alternatively, $\mathbf{S}'_{\text{core}}$ and $\mathbf{S}'_\nu$ to $\mathbf{S}'$ and then $\mathbf{S}'$and $\mathbf{S}'_{\text{val}}$ to $\mathbf{F}$. However, these two coupling schemes are equivalent in the sense that they both form a complete set of states and are related by a unitary transformation [47].

In the following, we will first combine $\mathbf{S}'_{\text{val}}$ and $\mathbf{S}'_{\text{core}}$ to $\mathbf{S}'$ for two reasons: First, $\mathbf{S}'$ then is identical to the coupled core- and valence spin $\mathbf{S}'$ introduced in the previous section. Second, this coupling order allows for a direct physical interpretation of the final states, since the possible values of S' here correspond to the spin-singlet ($S' = 0$) and spin-triplet ($S' = 1$) observable in the spectrum. Performing the angular momentum coupling, we obtain the final states in terms of the uncoupled ones

$$\begin{aligned}&|((S'_{\text{val}}S'_{\text{core}})S'S'_\nu)F, M_F\rangle \\ &= \sum_{M'_S, M'_\nu, M'_{\text{core}}, M'_{\text{val}}} C^{FM_F}_{S'M'_S S'_\nu M'_\nu} C^{S'M'_S}_{S'_{\text{val}}M'_{\text{val}}S'_{\text{core}}M'_{\text{core}}} |S'_{\text{val}}, M'_{\text{val}}\rangle |S'_{\text{core}}, M'_{\text{core}}\rangle |S'_\nu, M'_\nu\rangle\end{aligned} \tag{3.20}$$

with Clebsch-Gordan coefficients $C^{S'M'_S}_{S'_{\text{val}}M'_{\text{val}}S'_{\text{core}}M'_{\text{core}}}$ and $C^{FM_F}_{S'M'_S S'_\nu M'_\nu}$. After EC the atom is not in an eigenstate and starts to evolve in time due to the electromagnetic interactions between the electrons at an energy scale of $\sim$ 1 Ryd [84–86]. Hyperfine interaction – an effect on the sub-meV energy scale – thus is several orders of magnitude smaller and negligible in the atomic relaxation process. Hence, the Hamiltonian which determines the spectrum is the same we used to describe the case without hyperfine interaction (3.14).

The state $|F = 1/2, M_F = 1/2\rangle$ decays into a superposition of spin-triplet

$$\begin{aligned}\psi^{(S'=1)}_{1/2,1/2} =& \sqrt{\frac{2}{3}} \left|0'_{\text{nuc}}\right\rangle \otimes \left|\uparrow'_{\text{val}}\right\rangle \otimes \left|\uparrow'_{\text{core}}\right\rangle \otimes \left|\downarrow'_\nu\right\rangle \\ &- \sqrt{\frac{1}{6}} \left|0'_{\text{nuc}}\right\rangle \otimes \left|\uparrow'_{\text{val}}\right\rangle \otimes \left|\downarrow'_{\text{core}}\right\rangle \otimes \left|\uparrow'_\nu\right\rangle \\ &- \sqrt{\frac{1}{6}} \left|0'_{\text{nuc}}\right\rangle \otimes \left|\downarrow'_{\text{val}}\right\rangle \otimes \left|\uparrow'_{\text{core}}\right\rangle \otimes \left|\uparrow'_\nu\right\rangle\end{aligned} \tag{3.21}$$

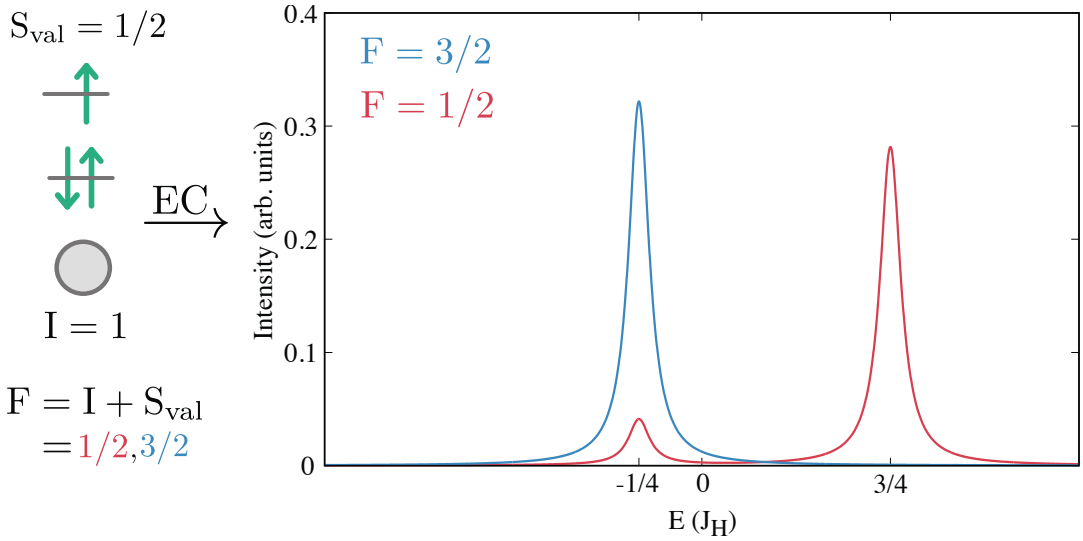

Figure 3.2: EC spectrum for a hyperfine coupled initial state with total angular momentum of $F = 1/2$ (red) and $F = 3/2$ (blue) as a function of Hund's exchange constant J_H. For anti-parallel nuclear and valence spin ($F = 1/2$), the atom decays into a superposition of spin-singlet at energy $E_S = 3/4\ J_H$ and spin-triplet at energy $E_T = -1/4\ J_H$. For parallel nuclear and valence spin ($F = 3/2$), only the spin-triplet at energy E_T is allowed.

and spin-singlet

$$\psi^{(S'=0)}_{1/2,1/2} = \sqrt{\frac{1}{2}} \left|0'_{\text{nuc}}\right\rangle \otimes \left|\uparrow'_{\text{val}}\right\rangle \otimes \left|\downarrow'_{\text{core}}\right\rangle \otimes \left|\uparrow'_{\nu}\right\rangle - \sqrt{\frac{1}{2}} \left|0'_{\text{nuc}}\right\rangle \otimes \left|\downarrow'_{\text{val}}\right\rangle \otimes \left|\uparrow'_{\text{core}}\right\rangle \otimes \left|\uparrow'_{\nu}\right\rangle . \tag{3.22}$$

To keep a clear and short notation, we omit the angular momentum quantum numbers $I', S'_{\text{val}}, S'_{\text{core}}$ and S'_{ν} in the description of the final states. Similar to the case of spin-up capture discussed in the previous section, the system decays into two states mirrored in two peaks (see Fig. 3.2, red). The only difference is that here the intensity is not equally distributed between spin-triplet and spin-singlet due to different Clebsch-Gordan coefficients in the initial and final states. The state $|F = 3/2, M_F = 3/2\rangle$, on the other hand, can only decay into the spin-triplet

$$\psi^{(S'=1)}_{3/2,3/2} = \left|0'_{\text{nuc}}\right\rangle \otimes \left|\uparrow'_{\text{val}}\right\rangle \otimes \left|\uparrow'_{\text{core}}\right\rangle \otimes \left|\uparrow'_{\nu}\right\rangle \tag{3.23}$$

In that case the spectrum is given by a single peak and is identical to the one obtained for spin-down capture (see Fig. 3.2, blue).

The analogy between the spin dependent spectra of the model without an active nucleus and the hyperfine state dependency of the nucleus-electron system is remarkable. While in the former model the number of final states depends on the spin-orientation of the captured electron with respect to the valence spin, in the nucleus-electron model it is determined by the relative orientation of $\mathbf{I}$ and $\mathbf{S}_{\mathrm{val}}$, i.e. the initial hyperfine state. As the weak interaction conserves the total angular momentum, the final states which are accessible after electron capture can be found by coupling nuclear, core, valence and neutrino angular momentum to $\mathbf{F}$. The experiment, however, is only sensitive to the electronic part of the final states which correspond to the eigenstates of H_{SM}. Just like the weak interaction conserves $\mathbf{F}$, so does H_{SM} conserve the coupled angular momentum of core and valence $\mathbf{S}'$ and consequently also $\mathbf{F}$. As the initial hyperfine state $\mathbf{F}$ determines the possible values of $\mathbf{S}'$, the observed final states are subject to selection rules which naturally arise from the conservation of $\mathbf{F}$. Note that the energy shift between the multiplets $S' = 0$ and $S' = 1$ is purely determined by the energy scale of the Coulomb repulsion. Therefore, the impact of hyperfine interaction on the nuclear decay, despite so tiny, becomes visible on this energy scale.

3.4 From simple model to ^{163}Ho

3.4.1 Atomic ^{163}Ho

Contrary to the simple model where we assumed a valence shell with $L_{\mathrm{val}} = 0, S_{\mathrm{val}} = J_{\mathrm{val}} = 1/2$ and a nucleus with $I = 1$, the nuclear and valence total angular momenta in ^{163}Ho are bigger and the angular momentum coupling becomes more involved. The ground state electronic configuration of atomic ^{163}Ho is $[\mathrm{Xe}]4\mathrm{f}^{11}6\mathrm{s}^2$. According to Hund's rules the ground state has $L = 6$, $S = 3/2$ and a total angular momentum of $J = 15/2$. However, this is only an approximated ground state configuration for two reasons: First, L and S are only approximately good quantum numbers due to a finite spin-orbit interaction in the valence shell. Second, Coulomb repulsion couples occupied and unoccupied shells to each other, thereby mixing in additional configurations. A more detailed discussion of the Ho ground state for a vanishing hyperfine interaction can be found in [9].

The simple nucleus-electron model introduced in the previous section reveals

the significance of hyperfine interaction in the calculation of the initial state. We expect the same to be the case for atomic ^{163}Ho and therefore as a first step identify all possible values of the total angular momentum F. With a total nuclear angular momentum of $I = 7/2$ we find $F = |I - J|, \ldots, I + J = 4, \ldots, 11$, each of which is $(2F + 1)$-fold degenerate such that in total there are $\sum_F (2F + 1) = 136$ different states that are eigenstates of

$$H = H_{\mathrm{D}} + H_{\mathrm{C}} + H_{\mathrm{HF}} \tag{3.24}$$

which includes besides the Dirac and Coulomb terms also the hyperfine interaction (3.7). In order to obtain the spectra for each F, a naive approach would be to calculate the spectra for all $|F, M_F\rangle$ and then to average over the $(2F + 1)$ spectra with the same F but different M_F. Although this approach is in principle realizable, a calculation of 136 spectra with sufficient accuracy for an element like ^{163}Ho with 67 interacting electrons is computationally expensive and not very practicable. A more sophisticated approach would be to first sort out (possible) identical spectra and thereby reduce the number of spectra to be calculated before actually calculating them. This is achieved by exploiting underlying symmetries.

As the transition operator (3.11) and the daughter Hamiltonian H_{Dy} responsible for the atomic relaxation both conserve F, the commutators $[T, F^2] = 0$ and $[H_{\mathrm{Dy}}, F^2] = 0$ vanish. As we proof in appendix A.2, this leads to the conclusion that all states with identical F but different M_F are equivalent in the sense that they lead to the same spectrum. Consequently, the number of spectra to be calculated reduces to only one per F and the differential decay rate $\frac{\mathrm{d}\Gamma}{\mathrm{d}\omega}$ can according to (3.13) be written as

$$\begin{aligned}\frac{\mathrm{d}\Gamma}{\mathrm{d}\omega} \propto &-\mathrm{Im}\,(Q-\omega)\sqrt{(Q-\omega)^2 - m_\nu^2} \\ &\times \left[\langle F|T^\dagger \frac{1}{\omega - H_{\mathrm{Dy}} + E_{\mathrm{Ho}} + \mathrm{i}\frac{\gamma}{2}} T|F\rangle - \langle F|T^\dagger \frac{1}{\omega + H_{\mathrm{Dy}} - E_{\mathrm{Ho}} + \mathrm{i}\frac{\gamma}{2}} T|F\rangle\right]\end{aligned} \tag{3.25}$$

with transition operator T defined in (3.11). Note that the z-component of total angular momentum in the initial state $|F, M_F\rangle \to |F\rangle$ is omitted to indicate that the spectrum is independent of M_F. Analogous to the simple nucleus-electron model, hyperfine interaction is neglected in the atomic relaxation process, i.e. we set $H_{\mathrm{Dy}} = H_{\mathrm{D}} + H_{\mathrm{C}}$ which governs the electronic dynamics in the nuclear potential of Dy.

Fig. 3.3 displays the normalized electron capture spectra (3.25) of ^{163}Ho for all possible hyperfine states $F = 4, \ldots, 11$ indicated by the different colors. The F de-

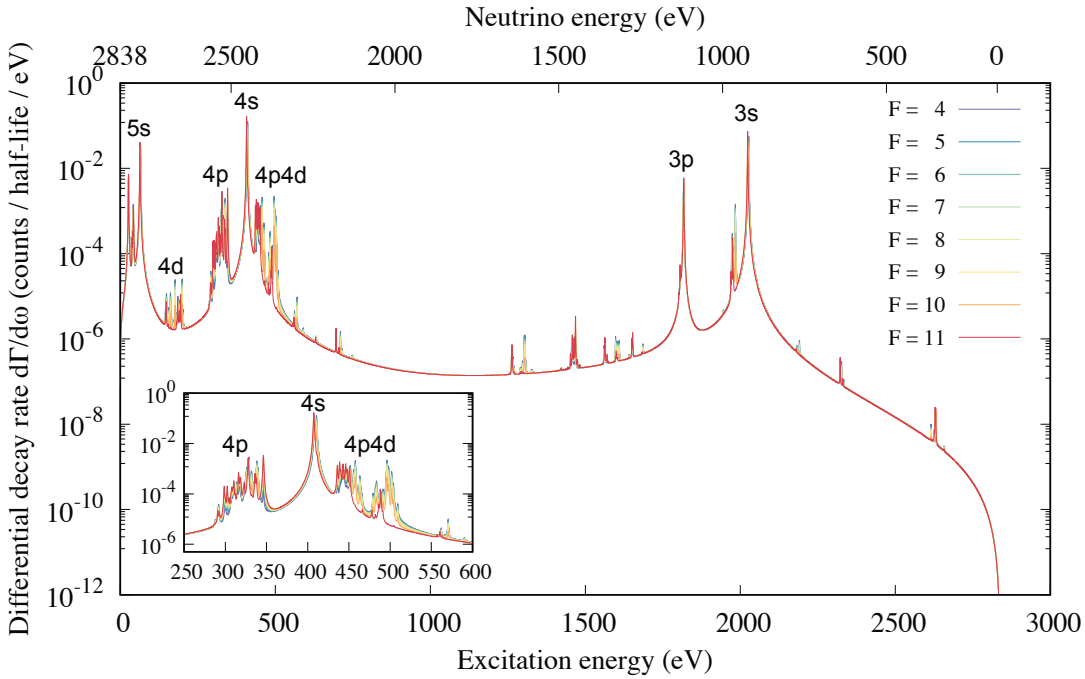

Figure 3.3: Differential electron capture decay rate per atom per average half-life for all possible total angular momenta $F = 4$ (purple) to $F = 11$ (red) as a function of the electronic excitation energy (bottom scale) or neutrino energy (top scale). The inset shows a section around the 4*s* resonance. For all spectra we assume a constant Lorentzian broadening of $\gamma = 1$ eV and a total decay energy of $Q = 2838$ eV [10].

pendence of the spectra is already clearly visible at first glance and affects the full energy window, i.e. all resonances. On closer inspection of the spectra presented in Fig. 3.3 one realizes that for small F the multiplets at higher excitation energy contain more spectral weight than for large F. Let us focus on the resonance with one hole in 4*s* (see inset of Fig. 3.3) which is the resonance with the overall highest intensity. Starting from the maximal total angular momentum, $F = 11$, almost all spectral weight is concentrated in a single peak. When lowering F, this resonance is split in two while spectral weight is continuously transferred to the second peak at about 5 eV higher energy. For $F < 9$, the intensity ratio of these two peaks is inverted and the second peak carries even more spectral weight than the first one. A similar behavior, but even more clearly visible in the spectra, is observed right of the 4*s* resonance where we find the states with two core holes, one in 4*p* and the other in 4*d*. This state can, for example, result from the capture of a 4*s* and subsequent atomic relaxation where a 4*p* electron scatters into

the $4f$ valence shell, while a $4d$ electron fills the created core hole in $4s$. Here the spectrum is particularly sensitive to F, as these multiplets involve an additional electron in the valence shell whose electronic configuration is strongly influenced by F. While some of the multiplets disappear, others are enhanced which in consequence leads to pronounced shifts of spectral weight by several Rydberg.

F-dependent lifetime

Surprisingly, the initial hyperfine state does not only determine the final states and their corresponding spectral weight, but also how fast the radioactive isotope decays. The lifetime τ is a measure of how quickly a radioactive isotope decays and is according to Fermi's golden rule proportional to the inverse of the integral over the differential decay rate

$$\tau \propto \left(\int_0^Q \frac{\mathrm{d}\Gamma}{\mathrm{d}\omega} \mathrm{d}\omega \right)^{-1} . \tag{3.26}$$

In order to grasp the origin of a hyperfine dependent lifetime, we first recall that the differential decay rate $\frac{\mathrm{d}\Gamma}{\mathrm{d}\omega}(\omega)$ can be written as the product of neutrino phase-space factor and resolvent projected onto the state after electron capture. The resolvent responsible for the atomic relaxation process generally conserves spectral weight, i.e. we find

$$\int_0^\infty \frac{\mathrm{d}\Gamma/\mathrm{d}\omega}{(Q-w)\sqrt{(Q-w)^2 - m_\nu^2}} \, \mathrm{d}\omega = \text{const.} \tag{3.27}$$

which in particular is independent of the initial hyperfine state. Hence, a fictitious decay rate solely given by the above integrand would consequently lead to a lifetime independent of F.

The neutrino phase-space factor is a measure of the number of states available a created neutrino with kinetic energy E_ν can occupy. From the F dependence of the spectra we already know that for small F the high-energy resonances on average contain more spectral weight than the ones at lower ω. Due to energy conservation, the total decay energy Q is shared between neutrino and electronic excitations. Therefore, a shift of spectral weight towards higher ω for smaller F leads to an on average lower neutrino energy. A lower neutrino energy, however, implies a reduced phase-space factor, i.e. less states available for the neutrino to occupy, and thus a lower decay rate. This is ultimately reflected in a smaller integral or an increased lifetime.

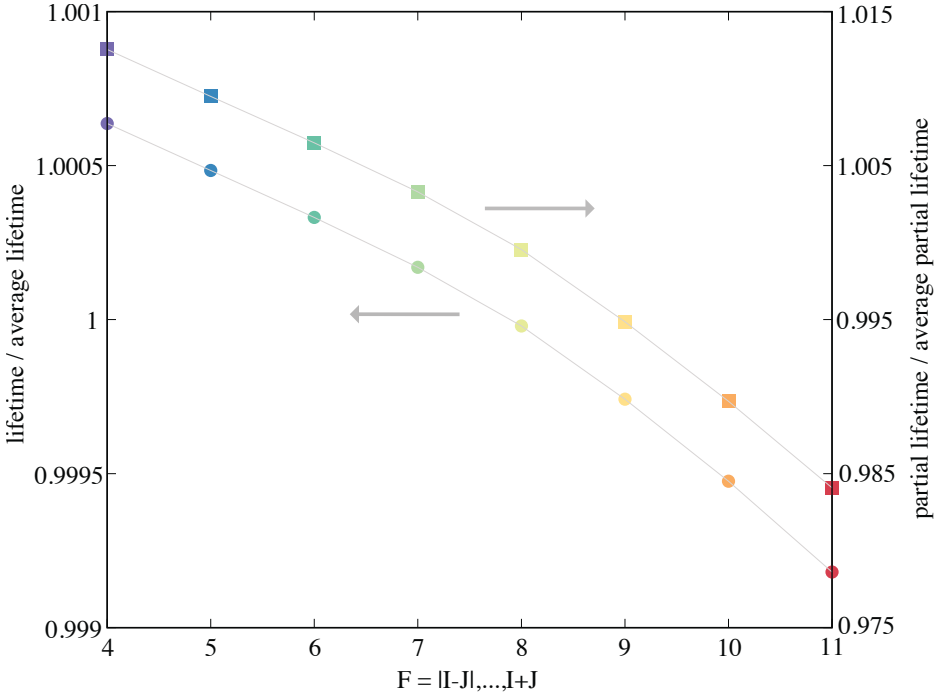

Figure 3.4: Lifetime over average lifetime (left) and partial lifetime over average partial lifetime of the 3*s* core hole (right) as a function of F ranging from $F = 4$ (purple) to $F = 11$ (red).

At high excitation energies the integral is more sensitive to shifts of spectral weight, because there the neutrino phase-space density changes more strongly than at lower energies. Therefore, the biggest change in lifetime is expected in this energy region. In order to obtain the F dependence of the integral only within a certain energy window, we can define a partial lifetime by restricting ω in (3.26) to $\omega \in [E - \epsilon, E + \epsilon]$ centered around a certain resonance energy E. Fig. 3.4 illustrates the lifetime and the partial lifetime at the M1 edge – the resonance with one core hole in 3*s* – as a function of F, both expressed relative to their corresponding averages. The (partial) lifetime is maximal at $F = 4$ and continuously decreases until it becomes minimal at $F = 11$. Here the continuous decrease directly reflects the energy dependence of the phase-space factor. While the maximal change of the lifetime (between $F = 4$ and $F = 11$) is $\sim 1.5‰$, this change is enhanced by about one order of magnitude at the M1 edge and amounts to $\sim 3\%$.

The endpoint of the EC spectrum is practically unaffected by the initial hyperfine state. Therefore, it is not necessary to include the hyperfine interaction in the calculations for the determination of the neutrino mass.

3.4.2 A realistic experimental setup: ^{163}Ho embedded in Gold

In the ECHo (Electron capture in ^{163}Ho Experiment) [28] the Ho atoms are implanted in Gold characterized by a face-centered cubic (fcc) structure and occupy regular lattice sites. The two valence shells ($6s$ and $4f$) hybridize with the Gold which allows valence electrons to populate neighboring sites. Three electrons contribute to the lattice resulting in a modified electronic configuration and different excitation energies. However, a calculation assuming Ho^{3+} ions with electronic configuration $[Xe]4f^{10}6s^0$ leads to spectra with unphysical artifacts. Here the problem is that the Ho atoms embedded in Gold are not fully ionized. The three delocalized electrons to some extent take part in the screening of the nuclear charge. In order to accurately capture this effect, one has to include the Gold band structure in the calculations [87]. As this is a challenge on its own due to an extensive size of the resulting Hilbert space, we here want to work within an approximation assuming the two $6s$ electrons to be localized, i.e. $[Xe]4f^{10}6s^2$. This electronic configuration maintains the symmetry of the Ho^{3+} ion and leads to spectra without unphysical artifacts.

According to Hund's rules the ground state is characterized by $L = 6$, $S = 2$ and $J = 8$. As the energies of the excited multiplets with $J < 8$ are several thousand Kelvin above the ground state, the occupation of these multiplets is strongly suppressed at temperatures well below room temperature which are considered in this chapter. Therefore, we restrict the following calculations to the ground state multiplet $J = 8$. With $I = 7/2$ the possible total angular momenta are $F = |I - J|, \ldots, I + J = 9/2, \ldots, 23/2$.

Non-spherical chemical environment

In addition to the modified electronic configuration, the surrounding Gold breaks the spherical symmetry of the Ho ions. Here we want to work within the framework of crystal field theory [88, 89] and take into account the non-spherical chemical environment by adding an effective crystal field potential H_{CF} to the Hamiltonian (3.24) acting on the valence shell of the Ho ions. The crystal field potential is generated by the electric field of the surrounding ions and has the same symmetry as the crystal lattice. It is convenient to expand the potential on renormalized spherical harmonics $C_{km}(\theta, \phi)$ [89]

$$H_{\mathrm{CF}} = \sum_{k=0}^{\infty} \sum_{m=-k}^{k} a_{km} r^k C_{km}(\theta, \phi) \tag{3.28}$$

where a_{km} are the expansion coefficients of the potential. In second quantization the crystal field Hamiltonian can be written as

$$H_{\mathrm{CF}} = \sum_{k=0}^{\infty} \sum_{m=-k}^{k} \sum_{\tau_i \tau_j} A_{km} \langle Y_{l_i m_i} | C_{km}(\theta, \phi) | Y_{l_j m_j} \rangle a^{\dagger}_{\tau_i} a_{\tau_j} \tag{3.29}$$

where we assume single-particle wave functions given by $\Psi(\mathbf{r}) = R_{nl}(r) Y_{lm}(\theta, \phi)$. The combined index $\tau = \{n_e, l_e, j_e\}$ comprises all relevant single-particle quantum numbers. As it is difficult to determine the radial part of the wave function within a solid, the expansion coefficients $A_{km} = a_{km} \langle R_{n_i l_i} | r^k | R_{n_j l_j} \rangle$ contain the expectation value of the radial part and are usually taken from experiment [89]. Note that the sum over k in (3.28) and (3.29) is infinite. However, only a finite and typically small number of the expansion coefficients are non-zero which can be found by exploiting symmetry properties of the valence shell and of the surrounding charges [89].

An alternative way to represent the crystal field was developed by Stevens in the early 1950s [90]. He suggested to expand the electrostatic potential in terms of total (electronic) angular momentum operators J_x, J_y, J_z. The explicit expression of the crystal field potential expanded on total angular momentum operators and the corresponding expansion coefficients - usually labeled by B_{km} - can be found in [89]. In the case of Ho implanted in Gold, the cubic (O_h) crystal field is characterized by the two parameters B_4 and B_6 which refer to an operator expansion in the sense of Stevens [91]. As both methods are equivalent, the set of parameters B_{km} can be related to the A_{km} by solving the equation defined by equalizing both crystal field Hamiltonians.

In order to obtain H_{CF} on a basis of spherical harmonics, the experimental crystal field parameters presented in [92] are first expressed in terms of Stevens coefficients according to [91, 93] and then transformed to the corresponding A_{km}. Explicitly, we find the following relations for the two non-zero parameters: $A_4 = -240240 B_4 = -160.1$ K and $A_6 = -\frac{61837776}{5} B_6 = 64.3$ K. Identifying the non-zero expansion coefficients

$$A_{40} = A_4, \quad A_{4\pm4} = \sqrt{\frac{5}{14}} A_4, \quad A_{60} = A_6, \quad A_{6\pm4} = -\sqrt{\frac{7}{2}} A_6 \tag{3.30}$$

finally enables us to set up the crystal field Hamiltonian (3.29). Then, we determine the level splitting of the $J = 8$ ground state by calculating the lowest

	Theory	**Experiment**
	E $[K]$	E $[K]$
Γ_3	0.00	0.00
Γ_4	0.11	0.14
Γ_5	7.04	7.64
Γ_3	40.93	44.95
Γ_4	42.23	46.38
Γ_1	43.64	47.92
Γ_5	51.73	56.68

Table 3.1: Crystal field multiplets for Holmium implanted in Gold. The experimental energy levels are taken from [92]. The theoretical values are obtained by calculating the 17 lowest eigenstates of $H = H_{\mathrm{D}} + H_{\mathrm{C}} + H_{\mathrm{CF}}$ whereby H_{CF} is based on the coefficients (3.30) derived from parameters which lead to the experimental splitting [92].

$(2J+1) = 17$ eigenstates of $H = H_{\mathrm{D}} + H_{\mathrm{C}} + H_{\mathrm{CF}}$. Table 3.1 displays the experimental and calculated energy levels. For vanishing hyperfine interaction, the 17-fold degenerate ground state is split due to the crystal field into three low-energy ($T < 8$ K) and four high-energy ($T > 45$ K) multiplets Γ_i which correspond to irreducible representations of the cubic (O_h) point group. By switching on hyperfine interaction, each of the 17 states is further split into $(2I+1) = 8$ sub-states such that in total there are $(2J+1)(2I+1) = 136$ states which correspond to the lowest 136 eigenstates of $H = H_{\mathrm{D}} + H_{\mathrm{C}} + H_{\mathrm{CF}} + H_{\mathrm{HF}}$. The splitting due to hyperfine interaction exceeds the energy difference between the ground state doublet Γ_3 and the first excited triplet Γ_4 resulting in a complicated level structure. For all other multiplets the crystal field exceeds the splitting due to hyperfine interaction, i.e. $H_{\mathrm{CF}} > H_{\mathrm{HF}}$, such that the individual multiplets are well separated from each other.

Due to the broken spherical symmetry the initial states are no longer eigenstates of defined total angular momentum. We can, however, expand these states in terms of the well-known hyperfine eigenstates

$$|\psi_i\rangle = \sum_{F,M_F} \alpha^i_{F,M_F} |F, M_F\rangle \tag{3.31}$$

with expansion coefficients $\alpha^i_{F,M_F} = \langle F, M_F|\psi_i\rangle$. As a result, the spectrum for a

given state $|\psi_i\rangle$ can be written as

$$\frac{\mathrm{d}\Gamma}{\mathrm{d}\omega} \propto -\,\mathrm{Im}\,(Q-\omega)\sqrt{(Q-\omega)^2-m_\nu^2}\sum_{F,M_F}\left|\alpha^i_{F,M_F}\right|^2 \times\left[\langle F|T^\dagger\frac{1}{\omega-H_{\mathrm{Dy}}+E_{\mathrm{Ho}}+\mathrm{i}\frac{\gamma}{2}}T|F\rangle-\langle F|T^\dagger\frac{1}{\omega+H_{\mathrm{Dy}}-E_{\mathrm{Ho}}+\mathrm{i}\frac{\gamma}{2}}T|F\rangle\right] \tag{3.32}$$

where T corresponds to the transition operator (3.11). Note that H_{Dy} governing the electronic dynamics neither includes the hyperfine interaction nor the crystal field. These terms are at least three orders of magnitude smaller than the Coulomb repulsion and thus irrelevant for the dynamics. In that case the spectra are just like for atomic Ho independent of M_F, such that the expansion (3.31) enables a computationally cheap calculation of the spectra. Instead of calculating (at most) 136 spectra, we only have to determine one spectrum for each F. These spectra are then linear combined to obtain the spectrum for a given $|\psi_i\rangle$.

Finite temperature

So far we have respected the non-spherical chemical environment on the level of crystal field theory. As every experimental measurement is performed at finite (and usually fixed) temperature T_{exp}, we furthermore have to take into account that at finite temperature the system generally populates not only the ground state, but a superposition of several states $|\psi_i\rangle$. The weight of each individual state is determined by Boltzmann statistics.

Although a measurement at fixed T_{exp} generally probes several F at once, the weight of each F is constant. As a result, an experiment at fixed temperature is insensitive to the spectral differences arising from the different hyperfine states. In (3.31) the eigenstates of the Hamiltonian including the crystal field, $|\psi_i\rangle$, are expanded in terms of hyperfine eigenstates $|F, M_F\rangle$. The weight of each F is determined by the expansion coefficients α^i_{F,M_F} and depends on the symmetry of $|\psi_i\rangle$. As the individual crystal field multiplets Γ_i typically show different symmetry properties, the amount of admixture of each F depends on the particular Γ_i. For this reason, a possible approach to experimentally resolve the impact of hyperfine interaction on the decay rate is to compare spectra where different crystal field multiplets are occupied.

In practice, this can be realized by measuring at various temperatures. For example, one can set three temperature regimes which are adapted to the level

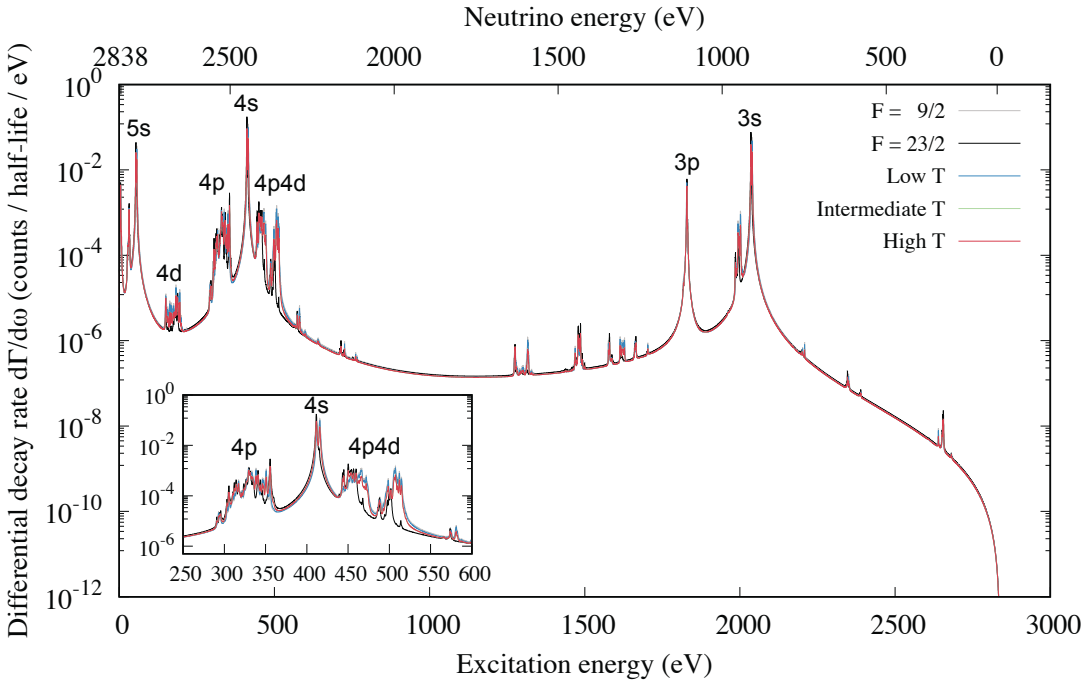

Figure 3.5: Comparison of the differential decay rate for the low (blue), intermediate (green) and high (red) temperature regime. Note that the spectral differences between intermediate and high temperatures are tiny and hardly visible. Additionally, the spectra for minimal ($F = 9/2$) and maximal ($F = 23/2$) total angular momentum are displayed in gray and black, respectively. All spectra are calculated according to (3.32) assuming the configuration $[\mathrm{Xe}]4\mathrm{f}^{10}6\mathrm{s}^2$, a constant Lorentzian broadening of $\gamma = 1$ eV and total decay energy of $Q = 2838$ eV [10].

structure displayed in Table 3.1: A low temperature regime at $T < 0.1$ K, an intermediate regime at 8 K $< T <$ 10 K and a high temperature regime at $T >$ 100 K. Fig. 3.5 displays the calculated spectra for the three different temperature regimes and the spectra for minimal ($F = 9/2$) and maximal ($F = 23/2$) total angular momentum.

In the low temperature limit, only the first four eigenstates with energy < 0.1 K are populated which corresponds to the lowest crystal field multiplet and the sub-states originating from hyperfine interaction. The states with higher energy are hardly occupied and can be neglected. The blue curve in Fig. 3.5 displays the spectrum for this temperature regime which is obtained by averaging over the spectra of the four lowest states. A comparison of the low-temperature spectrum with the one for $F = 9/2$ shows that the two spectra resemble each other. This

demonstrates that the lowest four states have predominantly $F = 9/2$ character with admixtures from $F = 11/2$ and $F = 13/2$. Higher values of F are strongly suppressed.

In the intermediate temperature regime, on the other hand, thermal energy is high enough to populate the lowest three crystal field multiplets, each of which is further split into $(2I + 1)$ sub-states which corresponds to the lowest 64 eigenstates. All total angular momenta, in particular also the ones with high F, contain considerable weight and are represented in the (average) spectrum.

The red plot in Fig. 3.5 shows the spectrum in the high temperature limit. Here, the lowest 136 eigenstates, i.e. all crystal field multiplets and corresponding substates, are populated. If we compare the spectra at intermediate and high temperatures to each other, the differences are tiny and hardly visible. This explains why the green curve in Fig. 3.5 is practically covered by the red one. Hence, a further rise from intermediate to high temperature accompanied by the population of the four high-energy crystal field multiplets does not significantly change the relative weight of the individual F. By comparing the spectra at low and intermediate/high temperatures to each other, the spectral differences resulting from the different hyperfine states finally become visible.

From the case of atomic Ho (see section 3.4.1) we know that spectral weight is shifted towards higher energies when F is lowered. At low temperature small values of F predominate, such that we find on average more spectral weight at higher energies than at intermediate or high temperatures, where higher F values gain more weight. As this shift of spectral weight directly affects the lifetime, we expect longer lifetimes the lower the temperature. The lifetime difference between the low and intermediate temperature regime amounts to $\sim 0.8‰$. Around the M1 edge (core hole in $3s$) this difference increases by about one order of magnitude to $\sim 0.7\%$.

3.5 Conclusion

In conclusion, we calculated the EC spectrum of (atomic) ^{163}Ho for different initial hyperfine eigenstates characterized by the total angular momentum F. Although hyperfine interaction – typically an effect on the sub-meV energy scale – is at least four orders of magnitude smaller than the dominant Coulomb repulsion, the calculated spectra show a clear dependence on the total angular momentum of the initial state. Changing F leads to a shift of spectral weight on the Ryd-

berg energy scale. For small F, our calculations predict on average more spectral weight at higher excitation energies than for large F.

In order to unveil the origin of this surprising effect, we first introduced a simple model. By disentangling the angular momenta of nucleus, core, valence and neutrino, we proved that the impact of hyperfine interaction originates from its complicated interplay with the Coulomb repulsion and the weak interaction. As the total angular momentum $\mathbf{F}$ remains conserved in a weak decay, selection rules naturally arising from this conservation determine the final states observed in the spectra. Depending on the initial F, the system decays into different final states with energy differences determined by the multiplet splitting on the Rydberg energy scale.

Furthermore, we found out that the shift of spectral weight as a function of F leads to a change of the isotope's lifetime on the per mille scale. It turns out that this change is related to a varying number of states the created neutrino can occupy. As the biggest changes of the neutrino phase-space factor are observed near the endpoint, at these energies partial lifetime differences on the percent scale are achievable.

In addition, we have considered a realistic experimental setup (realizable in the ECHo experiment [28]) by taking into account finite temperatures and the non-spherical chemical environment of the Ho ions on the level of crystal field theory. At finite temperature, the system populates a mixed state whereby our results reveal that Boltzmann statistics determines the weight of a given F. A comparison of the spectra measured at different temperatures thus enables to experimentally resolve spectral differences arising from the individual hyperfine eigenstates.

Note that the experimental measurements are typically performed at very low temperatures of $T_{\mathrm{exp}} < 0.1$ K [94]. This raises the question if it is possible to observe sharp and defined resonances at a relatively high temperature of about $T_{\mathrm{exp}} \approx 8$ K which is necessary to have a significant occupation of the three lowest crystal field multiplets. Note, however, that the presented method to unveil the impact of hyperfine interaction on the EC spectrum is not restricted to the proposed temperature regimes. One can, for example, focus only on the two lowest crystal field multiplets, the ground state doublet and the first excited triplet (see Table 3.1). These two multiplets are split by hyperfine interaction into 40 substates with energies up to about 1.9 K. Due to the significantly lower maximal temperature of only 1.9 K compared to the originally proposed 8 K, this might be

experimentally more realizable.

With a current detector resolution of < 10 eV [10] and high statistics in the experimental decay rates, the spectral differences between the individual hyperfine states could even nowadays be visible. What might be problematic is that the true line-broadening exceeds the assumed Lorentzian broadening of $\gamma = 1$ eV. Consequently, differences in the spectrum originating from hyperfine interaction might be smeared out. Therefore, it is important to include Auger-Meitner decay (responsible for the largest part of the line-broadening [11]) in future calculations, in order to see how hyperfine interaction induced spectral differences reveal under more realistic conditions.

Since the observed spectral differences induced by hyperfine interaction practically do not affect the endpoint of the EC spectrum, it is not necessary to include hyperfine interaction in the calculations for the determination of the neutrino mass.

4 Ab initio calculation of the line-broadening due to fluorescence decay

In a nuclear decay by EC, one of the core electrons is captured while simultaneously an electron neutrino is produced. In this process, the total energy Q, which generally depends on both the element under consideration and the particular isotope, is released. For a nuclear ground-to-ground-state decay, Q is due to energy conservation shared between electronic excitations and the energy taken away by the neutrino. After an electron is captured, the daughter atom ends up in an excited state and starts to de-excite. The atomic de-excitation is mainly driven by two processes: The first is caused by the electromagnetic interactions between the electrons, which eventually leads to the emission of Auger-Meitner electrons into the valence shell and the continuum [12, 13]. The second process is the fluorescence decay leading to the production of additional photons. Here, an excited state couples to the electromagnetic field and decays by spontaneous emission into a state with modified electron configuration and one additional photon. Both processes play an important role for an accurate description of the spectrum. While the release of Auger-Meitner electrons typically dominates the decay at lower excitation energies, fluorescence decay plays a superior role for the shells close to the nucleus at high excitation energy, i.e. in particular the K-shell, and elements with large charge number [95].

In section 2.7, we calculated EC spectra for several selected isotopes that undergo *allowed* transitions neglecting Auger-Meitner decay into continuum states and the decay due to fluorescence. Thus, we considered an approximate Hamiltonian involving only the Dirac term and the Coulomb interaction. In this case, the Hamiltonian is characterized by a discrete energy spectrum leading to sharp and well-defined resonances. To account for the experimentally observable broadening of the peaks, an energy-independent Lorentzian-broadening γ was introduced. However, a comparison of such calculations with experimental measurements clearly reveals that a constant broadening does not fit the true line-shapes

well, which show a strongly energy-dependent and asymmetric broadening.

In order to achieve better agreement of theory and experiment, a determination of the line-broadening from first principles becomes indispensable. Using the EC isotope ^{163}Ho as an example, the influence of the Auger-Meitner effect on the spectrum has been investigated [11]. It turned out that the scattering of electrons into unbound states with continuous energy spectrum leads to an energy-dependent and asymmetric broadening of the resonances. Finally, this results in a much better agreement between theory and experiment. However, due to a very small Q-value of about 2.8 keV, ^{163}Ho represents a special case. Since only those resonances with excitation energy smaller than the Q-value are visible in the spectrum, the *K*- and *L*-edge, for which fluorescence decay is particularly important, are excluded. Therefore, the agreement between theory and experiment neglecting fluorescence decay is already very good [11]. For most other EC isotopes, due to their much larger Q-values of the order of several hundred keV, far more energy can be stored in terms of electronic excitations, such that the high-energy resonances, i.e., especially the *K*-edge, become visible in the spectrum. A detailed knowledge of the spectrum at these energies is crucial as it determines the ionizing radiation released in the nuclear decay. The use of radionuclides for cancer treatment, for example, requires detailed knowledge not only of the amount of produced ionizing radiation, but also on its characteristics [5]. This knowledge is also essential to calibrate liquid scintillation counting, one of the primary techniques to determine activity of radionuclides [96].

In order to include fluorescence decay in the calculations, we have to extend the Hamiltonian by the light-matter interaction and by the kinetic energy of the photon. As the photon's energy plus that of the neutrino does not necessarily have to correspond to Q, additional energy can be stored in the form of electronic excitations. Therefore, a photon produced during the de-excitation process can assume all energies from zero up to the Q-value, thus exhibiting a continuous energy spectrum. Consequently, the decay rate has non-vanishing spectral weight at all electronic excitation energies.

In section 4.1, we perform a multipole expansion of the relativistic light-matter interaction which enables us to systematically study the impact of fluorescence decay on the spectral line-shape. Then, in section 4.2, we introduce the concept of self-energies and show on the example of fluorescence decay how a self-energy can be used to describe the line-broadening from first principles. In addition,

we derive an explicit expression of the fluorescence self-energy employing the multipole expansion of the light-matter interaction. Section 4.3 deals with the derivation of the fluorescence yield spectrum. In section 4.4, we finally use the developed concepts to calculate the high-energy radiative EC spectrum as well as the fluorescence yield spectrum of ^{55}Fe. The chapter ends with a summary of the main results.

4.1 Multipole expansion of the light-matter interaction

The Hamiltonian describing the (relativistic) interaction of light with matter in the Coulomb gauge is given by [46]

$$H_{e\gamma} = e \int \psi^\dagger(\mathbf{r}) \boldsymbol{\alpha} \cdot \mathbf{A}(\mathbf{r}) \psi(\mathbf{r}) \mathrm{d}^3 r \tag{4.1}$$

where $\psi^\dagger(\mathbf{r})$ and $\psi(\mathbf{r})$ are the four-component Dirac-spinor fields and $\boldsymbol{\alpha}$ the Dirac matrix. $\mathbf{A}(\mathbf{r})$ denotes the vector potential which in its canonical form reads

$$\mathbf{A}(\mathbf{r}) = \sum_{\mathbf{k}_\gamma} \sum_{\mu=1}^{2} \frac{1}{\sqrt{2V\omega_\gamma}} \left(\boldsymbol{\epsilon}_\mu(\mathbf{k}_\gamma) a^\dagger_{\mathbf{k}_\gamma,\mu} e^{i\mathbf{k}_\gamma \cdot \mathbf{r}} + \boldsymbol{\epsilon}^*_\mu(\mathbf{k}_\gamma) a_{\mathbf{k}_\gamma,\mu} e^{-i\mathbf{k}_\gamma \cdot \mathbf{r}} \right). \tag{4.2}$$

Here, V denotes the quantization volume which we set to 1. $\boldsymbol{\epsilon}_\nu(\mathbf{k}_\gamma)$ represents the polarization vector and $a^\dagger_{\mathbf{k}_\gamma,\nu}$ and $a_{\mathbf{k}_\gamma,\nu}$ are the creation and annihilation operators of a photon in mode $\{\mathbf{k}_\gamma, \mu\}$, respectively. The kinetic energy of the photons is given by

$$H_\gamma = \sum_{\mathbf{k}_\gamma} \sum_{\mu=1}^{2} \omega_\gamma a^\dagger_{\mathbf{k}_\gamma,\mu} a_{\mathbf{k}_\gamma,\mu}. \tag{4.3}$$

where $\omega_\gamma = c|\mathbf{k}_\gamma| = k_\mu$ with $c = 1$. Inserting the vector potential (4.2) into (4.1), the light-matter interaction Hamiltonian becomes

$$\begin{aligned} H_{e\gamma} = e \sum_{\mathbf{k}_\gamma} \sum_{\mu=1}^{2} & \frac{1}{\sqrt{2\omega_\gamma}} \\ & \times \int \psi^\dagger(\mathbf{r}) \boldsymbol{\alpha} \cdot \left(\boldsymbol{\epsilon}_\mu(\mathbf{k}_\gamma) a^\dagger_{\mathbf{k}_\gamma,\mu} e^{i\mathbf{k}_\gamma \cdot \mathbf{r}} + \boldsymbol{\epsilon}^*_\mu(\mathbf{k}_\gamma) a_{\mathbf{k}_\gamma,\mu} e^{-i\mathbf{k}_\gamma \cdot \mathbf{r}} \right) \psi(\mathbf{r}) \mathrm{d}^3 r. \end{aligned} \tag{4.4}$$

In order to simplify notation, we introduce the transition operator

$$T_{e\gamma}(\mathbf{k}_\gamma, \mu) = \boldsymbol{\epsilon}_\mu(\mathbf{k}_\gamma) \cdot \int \mathrm{d}^3 r \; \psi^\dagger(\mathbf{r}) \boldsymbol{\alpha} e^{i\mathbf{k}_\gamma \cdot \mathbf{r}} \psi(\mathbf{r}) \tag{4.5}$$

such that $H_{e\gamma}$ takes the compact form

$$H_{e\gamma} = e \sum_{\mathbf{k}_\gamma} \sum_{\mu=1}^{2} \frac{1}{\sqrt{2\omega_\gamma}} \left(a_\mu^\dagger(\mathbf{k}_\gamma) T_{e\gamma}(\mathbf{k}_\gamma, \mu) + a_\mu(\mathbf{k}_\gamma) T_{e\gamma}^\dagger(\mathbf{k}_\gamma, \mu) \right). \tag{4.6}$$

Note that the light-matter interaction involves only a single photon, i.e. $H_{e\gamma}$ can induce transitions from an initial state with n to a final state with $n \pm 1$ photons by absorbing or emitting a photon.

To systematically study the interaction between light and matter, it is convenient to decompose $T_{e\gamma}(\mathbf{k}_\gamma, \mu)$ into its multipoles. For brevity, we first drop the momentum dependence of $\boldsymbol{\epsilon}_\mu(\mathbf{k}_\gamma)$, i.e. $\boldsymbol{\epsilon}_\mu(\mathbf{k}_\gamma) \to \boldsymbol{\epsilon}_\mu$, and then expand $\boldsymbol{\epsilon}_\mu \cdot e^{i\mathbf{k}_\gamma \cdot \mathbf{r}}$ in terms of multipole potentials [46]

$$\boldsymbol{\epsilon}_\mu \cdot e^{i\mathbf{k}_\gamma \cdot \mathbf{r}} = 4\pi \sum_{JM\lambda} i^{J-\lambda} \left(\boldsymbol{\epsilon}_\mu \cdot \mathbf{Y}_{JM}^{(\lambda)*}(\hat{k}_\gamma) \right) \mathbf{a}_{JM}^{(\lambda)}(\mathbf{r}) \tag{4.7}$$

where $\lambda = 0, 1$ and $M = -J, \ldots, J$. As $\boldsymbol{\epsilon}_\nu \cdot e^{i\mathbf{k}_\gamma \cdot \mathbf{r}}$ transforms as a vector under rotations, the multipole potentials $\mathbf{a}_{JM}^{(\lambda)}(\mathbf{r})$ can be expressed as linear combinations of vector spherical harmonics $\mathbf{Y}_{JM}^{(\lambda)}(\hat{r})$

$$\begin{aligned} \mathbf{a}_{JM}^{(0)}(\mathbf{r}) &= j_J(k_\gamma r) \mathbf{Y}_{JM}^{(0)}(\hat{r}) \\ \mathbf{a}_{JM}^{(1)}(\mathbf{r}) &= \left(j_J'(k_\gamma r) + \frac{j_J(k_\gamma r)}{k_\gamma r} \right) \mathbf{Y}_{JM}^{(1)}(\hat{r}) + \sqrt{J(J+1)} \frac{j_J(k_\gamma r)}{k_\gamma r} \mathbf{Y}_{JM}^{(-1)}(\hat{r}). \end{aligned} \tag{4.8}$$

A definition of the vector spherical harmonics $\mathbf{Y}_{JM}^{(\lambda)}(\hat{r})$ can be found in [47]. In the Coulomb gauge plane waves are transverse. Therefore, their polarization vector $\boldsymbol{\epsilon}_\mu$ is perpendicular to the direction of propagation $\mathbf{k}_\gamma$, i.e. $\boldsymbol{\epsilon}_\mu \cdot \mathbf{k}_\gamma = 0$. Since the vector spherical harmonic $\mathbf{Y}_{JM}^{(-1)}(\hat{k}_\gamma)$ is parallel to $\mathbf{k}_\gamma$, we find that $\boldsymbol{\epsilon}_\mu \cdot \mathbf{Y}_{JM}^{(-1)}(\hat{k}_\gamma) = 0$, such that only the multipoles with $\lambda = 0, 1$ contribute to the above expansion. The parts with $\lambda = 0$ are referred to as *magnetic* multipoles, while those with $\lambda = 1$ represent the *electric* multipoles [46]. This labeling will become meaningful as soon as we have derived explicit expressions for the matrix elements later on, when it will turn out that the magnetic and electric multipoles matrix elements satisfy the corresponding selection rules.

Inserting the multipole expansion (4.7) into (4.5), the transition operator decomposed into the individual multipole moments is given by

$$T_{e\gamma}(\mathbf{k}_\gamma, \mu) = 4\pi \sum_{JM\lambda} i^{J-\lambda} \left(\boldsymbol{\epsilon}_\mu \cdot \mathbf{Y}_{JM}^{(\lambda)*}(\hat{k}_\gamma) \right) \int \mathrm{d}^3 r \, \psi^\dagger(\mathbf{r}) \boldsymbol{\alpha} \cdot \mathbf{a}_{JM}^{(\lambda)}(\mathbf{r}) \psi(\mathbf{r}). \tag{4.9}$$

In order to obtain an expression for $T(\mathbf{k}_\gamma, \mu)$ in second quantization, we next expand the four component Dirac-spinor field in terms creation $e_\tau^\dagger$ and annihilation e_τ operators weighted by the single-particle wave functions $\phi_\tau^\dagger(\mathbf{r})$ and $\phi_\tau(\mathbf{r})$, respectively,

$$\psi(\mathbf{r}) = \sum_\tau \phi_\tau(\mathbf{r}) e_\tau \qquad \psi^\dagger(\mathbf{r}) = \sum_\tau \phi_\tau^\dagger(\mathbf{r}) e_\tau^\dagger \tag{4.10}$$

where τ comprises the quantum numbers $\tau = \{n, \kappa, m\}$. Here, the single-particle wave functions are given by the previously introduced four-component spinors (2.12). Inserting (4.10) into (4.9) and using (2.12) as the single-particle wave functions, the second quantized form of the transition operator decomposed into a sum over *magnetic* ($\lambda = 0$) and *electric* ($\lambda = 1$) multipoles takes the form

$$T_{e\gamma}(\mathbf{k}_\gamma, \mu) = \sum_{\lambda=0}^{1} \sum_{\tau_a \tau_b} t_{\tau_b \tau_a}^{(\lambda)}(\mathbf{k}_\gamma, \mu) e_{\tau_b}^\dagger e_{\tau_a}. \tag{4.11}$$

The matrix elements $t_{\tau_b \tau_a}^{(\lambda)}(\mathbf{k}_\gamma, \nu)$ are explicitly given by

$$\begin{aligned}
&t_{\tau_b \tau_a}^{(0)}(\mathbf{k}_\gamma, \mu) \\
&= 4\pi \sum_{JM} i^J \left(\boldsymbol{\epsilon}_\mu \cdot \mathbf{Y}_{JM}^{(0)*}(\hat{k}_\gamma) \right) \int \mathrm{d}^3 r \, \phi_{\tau_b}^\dagger(\mathbf{r}) \boldsymbol{\alpha} \cdot \mathbf{a}_{JM}^{(0)} \phi_{\tau_a}(\mathbf{r}) \\
&= 4\pi \sum_{JM} i^{J+1} \left(\boldsymbol{\epsilon}_\mu \cdot \mathbf{Y}_{JM}^{(0)*}(\hat{k}_\gamma) \right) \int \mathrm{d}r \left(g_{n_b \kappa_b}(r) j_J(k_\gamma r) f_{n_a \kappa_a}(r) \right. \\
&\quad \left. \times \langle \Omega_{\kappa_b m_b} | \boldsymbol{\sigma} \cdot \mathbf{Y}_{JM}^{(0)} | \Omega_{-\kappa_a m_a} \rangle - f_{n_b \kappa_b}(r) j_J(k_\gamma r) g_{n_a \kappa_a}(r) \langle \Omega_{-\kappa_b m_b} | \boldsymbol{\sigma} \cdot \mathbf{Y}_{JM}^{(0)} | \Omega_{\kappa_a m_a} \rangle \right)
\end{aligned} \tag{4.12}$$

and

$$\begin{aligned}
&t_{\tau_b \tau_a}^{(1)}(\mathbf{k}_\gamma, \mu) \\
&= 4\pi \sum_{JM} i^{J-1} \left(\boldsymbol{\epsilon}_\mu \cdot \mathbf{Y}_{JM}^{(1)*}(\hat{k}_\gamma) \right) \int \mathrm{d}^3 r \, \phi_{\tau_b}^\dagger(\mathbf{r}) \boldsymbol{\alpha} \cdot \mathbf{a}_{JM}^{(1)} \phi_{\tau_a}(\mathbf{r}) \\
&= 4\pi \sum_{JM} i^{J} \left(\boldsymbol{\epsilon}_\mu \cdot \mathbf{Y}_{JM}^{(1)*}(\hat{k}_\gamma) \right) \int \mathrm{d}r \left[\left(j_J'(k_\gamma r) + \frac{j_J(k_\gamma r)}{k_\gamma r} \right) \left(g_{n_b \kappa_b}(r) f_{n_a \kappa_a}(r) \right. \right. \\
&\quad \left. \times \langle \Omega_{\kappa_b m_b} | \boldsymbol{\sigma} \cdot \mathbf{Y}_{JM}^{(1)} | \Omega_{-\kappa_a m_a} \rangle - f_{n_b \kappa_b}(r) g_{n_a \kappa_a}(r) \langle \Omega_{-\kappa_b m_b} | \boldsymbol{\sigma} \cdot \mathbf{Y}_{JM}^{(1)} | \Omega_{\kappa_a m_a} \rangle \right) \\
&\quad + \sqrt{J(J+1)} \frac{j_J(k_\gamma r)}{k_\gamma r} \left(g_{n_b \kappa_b}(r) f_{n_a \kappa_a}(r) \langle \Omega_{\kappa_b m_b} | \boldsymbol{\sigma} \cdot \mathbf{Y}_{JM}^{(-1)} | \Omega_{-\kappa_a m_a} \rangle \right. \\
&\quad \left. \left. - f_{n_b \kappa_b}(r) g_{n_a \kappa_a}(r) \langle \Omega_{-\kappa_b m_b} | \boldsymbol{\sigma} \cdot \mathbf{Y}_{JM}^{(-1)} | \Omega_{\kappa_a m_a} \rangle \right) \right]
\end{aligned} \tag{4.13}$$

for the *magnetic* and *electric* multipoles, respectively. Both involve matrix elements of products of the vector of Pauli matrices σ and vector spherical harmonics that can be rewritten in terms of matrix elements of ordinary spherical harmonics using the following relations [46]:

$$\begin{aligned}
\langle \Omega_{\kappa_b m_b} | \boldsymbol{\sigma} \cdot \mathbf{Y}^{(-1)}_{JM} | \Omega_{\kappa_a m_a} \rangle &= -\langle \Omega_{-\kappa_b m_b} | Y_{JM} | \Omega_{\kappa_a m_a} \rangle \\
\langle \Omega_{\kappa_b m_b} | \boldsymbol{\sigma} \cdot \mathbf{Y}^{(0)}_{JM} | \Omega_{\kappa_a m_a} \rangle &= \frac{\kappa_a - \kappa_b}{\sqrt{J(J+1)}} \langle \Omega_{\kappa_b m_b} | Y_{JM} | \Omega_{\kappa_a m_a} \rangle \\
\langle \Omega_{\kappa_b m_b} | \boldsymbol{\sigma} \cdot \mathbf{Y}^{(1)}_{JM} | \Omega_{\kappa_a m_a} \rangle &= \frac{\kappa_a + \kappa_b}{\sqrt{J(J+1)}} \langle \Omega_{-\kappa_b m_b} | Y_{JM} | \Omega_{\kappa_a m_a} \rangle
\end{aligned} \tag{4.14}$$

Hence, the matrix element for magnetic multipoles simplifies to

$$\begin{aligned}
t^{(0)}_{\tau_b \tau_a}(\mathbf{k}_\gamma, \mu) &= 4\pi \sum_{JM} i^{J+1} \left(\boldsymbol{\epsilon}_\mu \cdot \mathbf{Y}^{(0)*}_{JM}(\hat{k}_\gamma) \right) \langle \Omega_{\kappa_b m_b} | Y_{JM} | \Omega_{-\kappa_a m_a} \rangle \\
&\qquad \times \frac{-(\kappa_a + \kappa_b)}{\sqrt{J(J+1)}} R^{(0)}_{\tau_b \tau_a}(\omega_\gamma) \\
&\equiv 4\pi \sum_{JM} i^{J+1} \left(\boldsymbol{\epsilon}_\mu \cdot \mathbf{Y}^{(0)*}_{JM}(\hat{k}_\gamma) \right) \left[T^{(0)}_{JM}(\omega_\gamma) \right]_{\tau_b \tau_a}
\end{aligned} \tag{4.15}$$

with radial integral $R^{(0)}_{\tau_b \tau_a}(\omega_\gamma) = \int \mathrm{d}r \, j_J(k_\gamma r) \, (g_{n_b \kappa_b} f_{n_a \kappa_a} + f_{n_b \kappa_b} g_{n_a \kappa_a})$. For the electric multipoles, on the other hand, we obtain matrix elements of the form

$$\begin{aligned}
t^{(1)}_{\tau_b \tau_a}(\mathbf{k}_\gamma, \mu) &= 4\pi \sum_{JM} i^{J} \left(\boldsymbol{\epsilon}_\mu \cdot \mathbf{Y}^{(1)*}_{JM}(\hat{k}_\gamma) \right) \langle \Omega_{\kappa_b m_b} | Y_{JM} | \Omega_{\kappa_a m_a} \rangle \\
&\qquad \times \left[\frac{\kappa_b - \kappa_a}{\sqrt{J(J+1)}} R^{(1,1)}_{\tau_b \tau_a}(\omega_\gamma) + \sqrt{J(J+1)} R^{(1,2)}_{\tau_b \tau_a}(\omega_\gamma) \right] \\
&\equiv 4\pi \sum_{JM} i^{J} \left(\boldsymbol{\epsilon}_\mu \cdot \mathbf{Y}^{(1)*}_{JM}(\hat{k}_\gamma) \right) \left[T^{(1)}_{JM}(\omega_\gamma) \right]_{\tau_b \tau_a}
\end{aligned} \tag{4.16}$$

where we have introduced the following abbreviations for the two radial integrals:

$$R^{(1,\alpha)}_{\tau_b \tau_a}(\omega_\gamma) = \begin{cases} \int \mathrm{d}r \, (g_{n_b \kappa_b} f_{n_a \kappa_a} + f_{n_b \kappa_b} g_{n_a \kappa_a}) \left(j'_J(k_\gamma r) + \frac{j_J(k_\gamma r)}{k_\gamma r} \right) & \text{for } \alpha = 1 \\ \int \mathrm{d}r \, (f_{n_b \kappa_b} g_{n_a \kappa_a} - g_{n_b \kappa_b} f_{n_a \kappa_a}) \, \frac{j_J(k_\gamma r)}{k_\gamma r} & \text{for } \alpha = 2 \end{cases} \tag{4.17}$$

Note that the matrix elements $\left[T^{(0)}_{JM}(\omega_\gamma) \right]_{\tau_b \tau_a}$ and $\left[T^{(1)}_{JM}(\omega_\gamma) \right]_{\tau_b \tau_a}$ involve only those parts that are independent of the photon's polarization and direction of propagation.

While the radial part must be evaluated numerically, for the angular part there exists an analytical solution. Matrix elements of the form $\langle \Omega_{\kappa_b m_b} | Y_{JM} | \Omega_{\kappa_a m_a} \rangle$ are conveniently evaluated by using the Wigner-Eckart theorem [47, 50] which allows us to write the angular part as

$$\langle \Omega_{\kappa_b m_b} | Y_{JM} | \Omega_{\kappa_a m_a} \rangle = (-1)^{j_b - m_b} \begin{pmatrix} j_b & J & j_a \\ -m_b & M & m_a \end{pmatrix} \langle \Omega_{\kappa_b} || Y_J || \Omega_{\kappa_a} \rangle. \tag{4.18}$$

Here, $\langle \Omega_{\kappa_b} || Y_J || \Omega_{\kappa_a} \rangle$ denotes the reduced matrix element and the expression in brackets is the Wigner 3j-symbol [47, 50]. The reduced matrix element vanishes if $l_b + J + l_a$ is odd and takes the value

$$\langle \Omega_{\kappa_b} || Y_J || \Omega_{\kappa_a} \rangle = (-1)^{j_b + 1/2} \sqrt{(2j_b+1)(2j_a+1)(2J+1)/4\pi} \begin{pmatrix} j_b & j_a & J \\ -1/2 & 1/2 & 0 \end{pmatrix} \tag{4.19}$$

if $l_b + J + l_a$ is even. Thus, $\left[T^{(0)}_{JM}(\omega_\gamma) \right]_{\tau_b \tau_a}$ can be written as

$$\begin{aligned} \left[T^{(0)}_{JM}(\omega_\gamma) \right]_{\tau_b \tau_a} = (-1)^{2j_b - m_b + 3/2} & \begin{pmatrix} j_b & J & j_a \\ -m_b & M & m_a \end{pmatrix} \begin{pmatrix} j_b & j_a & J \\ -1/2 & 1/2 & 0 \end{pmatrix} \\ & \times \sqrt{(2j_b+1)(2j_a+1)(2J+1)/4\pi} \frac{\kappa_a + \kappa_b}{\sqrt{J(J+1)}} R^{(0)}_{\tau_b \tau_a}(\omega_\gamma) \end{aligned} \tag{4.20}$$

if $l_b + J + l_a \pm 1$ is even, whereas $\left[T^{(1)}_{JM}(\omega_\gamma) \right]_{\tau_b \tau_a}$ becomes

$$\begin{aligned} \left[T^{(1)}_{JM}(\omega_\gamma) \right]_{\tau_b \tau_a} = (-1)^{2j_b - m_b + 1/2} & \begin{pmatrix} j_b & J & j_a \\ -m_b & M & m_a \end{pmatrix} \begin{pmatrix} j_b & j_a & J \\ -1/2 & 1/2 & 0 \end{pmatrix} \\ & \times \sqrt{(2j_b+1)(2j_a+1)(2J+1)/4\pi} \left[\frac{\kappa_b - \kappa_a}{\sqrt{J(J+1)}} R^{(1,1)}_{\tau_b \tau_a}(\omega_\gamma) \right. \\ & \left. + \sqrt{J(J+1)} R^{(1,2)}_{\tau_b \tau_a}(\omega_\gamma) \right] \end{aligned} \tag{4.21}$$

if $l_b + J + l_a$ is even.

Note that the condition $'l_b + J + l_a \pm 1 = \text{even}'$ for magnetic and $'l_b + J + l_a = \text{even}'$ for electric multipole transitions to be non-vanishing, along with the properties of the Wigner 3j-symbols, reflects what is referred to as *selection rules*. For electric dipole transitions ($\lambda = 1$, $J = 1$), for example, the selection rule states that a transition is only possible between states with opposite parity and $\Delta j = j_b - j_a = 0, 1$, while a transition between two states with $j_b = j_a = 0$ is

forbidden. In addition, the condition $m_b = m_a, m_a \pm 1$ must be fulfilled [50]. This condition is exactly reflected in (4.21). On the other hand, the selection rule for a magnetic dipole transition ($\lambda = 0$, $J = 1$) is identical to the one for the electric dipole with the difference that here the two states must have the same parity. This condition is contained in $'l_b + J + l_a \pm 1 = \text{even}'$.

4.2 Fluorescence self-energy

Compared to section 2.7 where we calculated the EC spectrum neglecting fluorescence and Auger-Meitner decay, we now consider a Hamiltonian of the form

$$H = H_D + H_C + H_{e\gamma} + H_\gamma \equiv H_0 + H_{e\gamma} + H_\gamma \tag{4.22}$$

which in addition to Dirac's Hamiltonian and the Coulomb interaction, H_D and H_C, also includes the light-matter interaction $H_{e\gamma}$ and the photon's kinetic energy H_γ. Due to $H_{e\gamma}$, excited states can decay subsequent to EC by the emission of a photon. Several photons can also be released during the de-excitation process. However, since the light-matter interaction is linear in the photon creation and annihilation operators, this would require higher-order processes in perturbation theory, which are much less likely. For this reason, we can restrict ourselves to those processes that involve only one additional photon and further assume no photons to be present at the beginning. In this special case, $H_{e\gamma}$ couples the two sub-spaces with zero and one photon.

The aim of this section is to describe the impact of fluorescence decay on the EC spectrum. Starting from bound states that do not contain any photons, we investigate how these resonances are affected by the additional decay channel. The most obvious approach to this problem is to determine the Green's function

$$G^-(\omega) = \langle \psi_0 | T_{\text{EC}}^\dagger \frac{1}{\omega + i\eta^+ - H_0 - H_{e\gamma} - H_\gamma} T_{\text{EC}} | \psi_0 \rangle. \tag{4.23}$$

Here, T_{EC} denotes the transition operator used to describe the weak interaction. Note that the parent ground state energy is set to zero. This expression, however, would require to invert the full Hamiltonian (4.22) which is no longer possible in this case. After the emission of a photon the atom does not necessarily end up in its ground state, since additional energy may be stored in the form of electronic excitations. Consequently, the photon's kinetic energy can assume all values from 0 up to the Q-value which can correspond to an energy window up to

several hundred keV. Due to this large energy domain, the resulting Hilbert space including states with one photon is of extensive size rendering a determination of the Green's function in this way infeasible.

Instead of directly employing (4.23), we follow an alternative approach presented in [11, 97]. We first partition the Hamiltonian into two parts defined by the projection operators

$$P = \sum_i |\psi_i\rangle\langle\psi_i|, \qquad Q = \sum_i |\phi_i\rangle\langle\phi_i|. \tag{4.24}$$

Here, $|\psi_i\rangle$ denote the bound states with no photon, whereas $|\phi_i\rangle = |\psi_i\rangle \otimes |\mathbf{k}_\gamma, \mu\rangle$ are those configurations involving a single photon. Using the projection operators P and Q the Hamiltonian can be written as

$$H = \begin{pmatrix} PHP & PHQ \\ QHP & QHQ \end{pmatrix} = \begin{pmatrix} PH_0P & PH_{e\gamma}Q \\ QH_{e\gamma}P & Q(H_0 + H_\gamma)Q \end{pmatrix}. \tag{4.25}$$

We aim to find out how the line-shape of the resonances is influenced by the decay due to fluorescence. Thus, we restrict the inversion of (4.25) to the sub-space defined by P, i.e. to those states involving no photon, which yields [97]

$$P\frac{1}{\omega + i\eta^+ - H}P = \frac{1}{\omega + i\eta^+ - PH_0P - \Sigma(\omega)} \tag{4.26}$$

where the fluorescence self-energy is introduced as

$$\Sigma(\omega) = PH_{e\gamma}Q\frac{1}{\omega + i\eta^+ - Q(H_0 + H_\gamma)Q}QH_{e\gamma}P. \tag{4.27}$$

Since the light-matter interaction Hamiltonian acts only between the sub-spaces with zero and one photon, we find $PH_{e\gamma}P = 0$. Consequently, all projectors Q that occur in $\Sigma(\omega)$ can be replaced by unit operators. Inserting the explicit expression for the projector P on the left and right allows us to express the self-energy as a matrix with components

$$\Sigma_{ij}(\omega) = \langle\psi_i|H_{e\gamma}\frac{1}{\omega + i\eta^+ - H_0 - H_\gamma}H_{e\gamma}|\psi_j\rangle. \tag{4.28}$$

The dimension of this matrix is determined by the dimension of the sub-space defined by P. The EC spectrum including the decay due to fluorescence is then

obtained by taking the expectation value of the projected resolvent (4.26) with respect to the state after EC:

$$G^{-}(\omega) = \sum_{ij} \langle \psi_0 | T_{\mathrm{EC}}^{\dagger} | \psi_i \rangle \langle \psi_i | \frac{1}{\omega - E_i \delta_{ij} - \Sigma_{ij}(\omega)} | \psi_j \rangle \langle \psi_j | T_{\mathrm{EC}} | \psi_0 \rangle \tag{4.29}$$

Here, we assumed that H_0 is diagonal on P, i.e. $PH_0P = \sum_i E_i |\psi_i\rangle\langle\psi_i| \equiv \mathrm{diag}(E_i)$. Thus, the impact of fluorescence decay on the EC spectrum is effectively incorporated in the self-energy $\Sigma_{ij}(\omega)$. This enables us to easily include the additional relaxation process due to fluorescence decay into existing calculations that neglect this decay channel. Here the big advantage is that both the Green's function and the self-energy are evaluated on the sub-space of states with no photon. Therefore, the active Hilbert space to be considered is much smaller than the full one including the states with one photon which would have been necessary for the calculation of (4.23) and thus is computationally much more favorable.

Let us now take a closer look at the self-energy and discuss some of its properties along with their physical interpretation. Considering (4.28) we first notice that $\Sigma(\omega)$ has the same mathematical structure as a Green's function and is therefore a complex-valued object. While its real part shifts the peak positions, the imaginary part leads to the broadening of the resonances. The previously used energy independent Lorentzian broadening γ (used as a fit parameter) is now replaced by the imaginary part of the fluorescence self-energy calculated from first principles (see (4.29)). Note that the self-energy itself contains an infinitesimal imaginary part η^{+}. This, however, has no effect of the spectrum as it drops out of the equations when employing a principal value decomposition as we will see in (4.39).

According to Fermi's golden rule, the broadening of a state $|\psi_i\rangle$ is related to its lifetime τ_i by $\tau_i^{-1} \propto -\mathrm{Im}\ \Sigma_{ii}(E_i)$, where E_i denotes the excitation energy of $|\psi_i\rangle$. Note, however, that the fluorescence self-energy alone captures only parts of the experimentally observed broadening and thus describes only the (partial) lifetime related to fluorescence. Auger-Meitner decay into continuum states is of the same order of magnitude and is essential for an accurate description of the spectrum [11]. While fluorescence decay plays a superior role at high excitation energies, i.e. in particular starting from the *K*-edge, Auger-Meitner decay usually dominates the line-broadening at lower excitation energies [95]. In experiments that rely on a calorimetric measurement of the EC spectrum, the isotopes are embedded in some absorber material. Consequently, the isotope's outer shells hybridize with the orbitals of surrounding absorber material thereby opening ad-

ditional relaxation channels. The influence of these can be taken into account by introducing a suitable self-energy, analogous to the one derived here [55, 87]. As the decay due to fluorescence and Auger-Meitner decay into the continuum (or the chemical environment) are fully unrelated processes, the total self-energy is obtained by adding up the self-energies of the individual decay channels.

Moreover, $\Sigma_{ij}(\omega)$ is generally not diagonal. Therefore, bound states without photon, which are decoupled from each other neglecting the self-energy, are now coupled by the off-diagonal elements. The interference induced in this way leads to an asymmetric broadening of the resonances known as Fano's effect [98]. However, as shown on the example of Auger-Meitner decay in ^{163}Ho, the asymmetry induced by the energy-dependent broadening is much larger and mainly responsible for the observed line-shape [11]. The same is to be expected for the decay due to fluorescence.

The self-energy in terms of multipoles

In the following steps, we further simplify the fluorescence self-energy. For this purpose, we employ the multipole expansion of the light-matter interaction derived in section 4.1, which allows us to study the impact of individual multipoles on the spectral line-shape. Substituting (4.6) for $H_{e\gamma}$, the self-energy becomes

$$\Sigma_{ij}(\omega) = \frac{e^2}{2} \sum_{\mu=1}^{2} \sum_{\mathbf{k}_\gamma} \frac{1}{\omega_\gamma} \langle \psi_i | T^\dagger_{e\gamma}(\mathbf{k}_\gamma, \mu) \frac{1}{\omega + i\eta^+ - H_0 - H_\gamma} T_{e\gamma}(\mathbf{k}_\gamma, \mu) | \psi_j \rangle. \quad (4.30)$$

The sum over all photon momenta $\mathbf{k}_\gamma$ can be performed by taking the continuum limit as

$$\sum_{\mathbf{k}_\gamma} \to \frac{1}{(2\pi)^3} \int \mathrm{d}^3 k_\gamma = \frac{1}{(2\pi)^3} \int \mathrm{d}\omega_\gamma \omega_\gamma^2 \mathrm{d}\Omega_\gamma \quad (4.31)$$

where we assume spherical coordinates. Hence, the fluorescence self-energy can be written as

$$\Sigma_{ij}(\omega) = \frac{e^2}{2(2\pi)^3} \sum_{\mu=1}^{2} \int \langle \psi_i | T^\dagger_{e\gamma}(\mathbf{k}_\gamma, \mu) \frac{1}{\omega + i\eta^+ - H_0 - H_\gamma} T_{e\gamma}(\mathbf{k}_\gamma, \mu) | \psi_j \rangle \times \omega_\gamma \mathrm{d}\omega_\gamma \mathrm{d}\Omega_\gamma. \quad (4.32)$$

Inserting (4.11) for the transition operator $T_{e\gamma}(\mathbf{k}_\gamma, \mu)$ with matrix elements (4.15) and (4.16) for the magnetic and electric multipoles, respectively, and further using

that $H_\gamma a^\dagger_{\mathbf{k}_\gamma,\mu}|\psi_i\rangle = \omega_\gamma a^\dagger_{\mathbf{k}_\gamma,\mu}|\psi_i\rangle$, we finally end up with

$$\Sigma_{ij}(\omega) = 4\alpha \sum_{\mu=1}^{2} \int \omega_\gamma \mathrm{d}\omega_\gamma \mathrm{d}\Omega_\gamma \sum_{\tau_a\tau_b\tau'_a\tau'_b} \sum_{JM\lambda} \sum_{J'M'\lambda'} \left(\mathbf{Y}^{(\lambda')}_{J'M'}(\hat{k}_\gamma)\cdot\boldsymbol{\epsilon}^*_\mu\right)\left(\boldsymbol{\epsilon}_\mu\cdot\mathbf{Y}^{(\lambda)*}_{JM}(\hat{k}_\gamma)\right) \times \left[T^{(\lambda')}_{J'M'}(\omega_\gamma)\right]_{\tau'_b\tau'_a}\left[T^{(\lambda)}_{JM}(\omega_\gamma)\right]_{\tau_b\tau_a}\left\langle\psi_i\middle|e^\dagger_{\tau'_b}e_{\tau'_a}\frac{1}{\omega+i\eta^+-H_0-\omega_\gamma}e^\dagger_{\tau_b}e_{\tau_a}\middle|\psi_j\right\rangle \tag{4.33}$$

where α denotes the fine-structure constant. As the vector spherical harmonics with $\lambda = 0, 1$ both are orthogonal to $\hat{k}_\gamma$, the sum over the two polarizations can be performed as [46]

$$\sum_{\mu=1}^{2}\left(\mathbf{Y}^{(\lambda')}_{J'M'}(\hat{k}_\gamma)\cdot\boldsymbol{\epsilon}^*_\mu\right)\left(\boldsymbol{\epsilon}_\mu\cdot\mathbf{Y}^{(\lambda)*}_{JM}(\hat{k}_\gamma)\right) = \left(\mathbf{Y}^{(\lambda')}_{J'M'}(\hat{k}_\gamma)\cdot\mathbf{Y}^{(\lambda)*}_{JM}(\hat{k}_\gamma)\right) \tag{4.34}$$

such that the self-energy simplifies to

$$\Sigma_{ij}(\omega) = 4\alpha \int \omega_\gamma \sum_{\tau_a\tau_b\tau'_a\tau'_b} \sum_{JM\lambda} \sum_{J'M'\lambda'} \left(\mathbf{Y}^{(\lambda')}_{J'M'}(\hat{k}_\gamma)\cdot\mathbf{Y}^{(\lambda)*}_{JM}(\hat{k}_\gamma)\right)\left[T^{(\lambda')}_{J'M'}(\omega_\gamma)\right]_{\tau'_b\tau'_a} \times \left[T^{(\lambda)}_{JM}(\omega_\gamma)\right]_{\tau_b\tau_a}\left\langle\psi_i\middle|e^\dagger_{\tau'_b}e_{\tau'_a}\frac{1}{\omega+i\eta^+-H_0-\omega_\gamma}e^\dagger_{\tau_b}e_{\tau_a}\middle|\psi_j\right\rangle \mathrm{d}\omega_\gamma\mathrm{d}\Omega_\gamma. \tag{4.35}$$

In the following, we integrate over the photon's kinetic energy and all momentum directions. To evaluate the latter integral, we exploit that the vector spherical harmonics obey in analogy to the ordinary ones the orthonormality relation [47]

$$\int \mathrm{d}\Omega_\gamma\ \mathbf{Y}^{(\lambda')*}_{J'M'}(\hat{k}_\gamma)\cdot\mathbf{Y}^{(\lambda)}_{JM}(\hat{k}_\gamma) = \delta_{J'J}\delta_{M'M}\delta_{\lambda'\lambda}. \tag{4.36}$$

This enables us to directly integrate over all photon directions

$$\Sigma_{ij}(\omega) = 4\alpha \int \sum_{\tau_a\tau_b\tau'_a\tau'_b} \sum_{JM\lambda} \left[T^{(\lambda)}_{JM}(\omega_\gamma)\right]_{\tau'_b\tau'_a}\left[T^{(\lambda)}_{JM}(\omega_\gamma)\right]_{\tau_b\tau_a} \times \left\langle\psi_i\middle|e^\dagger_{\tau'_b}e_{\tau'_a}\frac{1}{\omega+i\eta^+-H_0-\omega_\gamma}e^\dagger_{\tau_b}e_{\tau_a}\middle|\psi_j\right\rangle \omega_\gamma\mathrm{d}\omega_\gamma. \tag{4.37}$$

It is important to note that a direct consequence of the orthonormality relation (4.36) is that different multipoles as well as magnetic and electric parts of the transition operator never interfere. To evaluate the integral over ω_γ, we replace

$$\frac{1}{\omega+i\eta^+-H_0-\omega_\gamma} \longrightarrow \sum_n \frac{|\psi_n\rangle\langle\psi_n|}{\omega+i\eta^+-E_n-\omega_\gamma}$$

where $|\psi_n\rangle$ are eigenstates of H_0. Then we rewrite $\frac{1}{\omega+i\eta^+-E_n-\omega_\gamma}$ as

$$\frac{1}{\omega+i\eta^+-E_n-\omega_\gamma} = \mathcal{P}\frac{1}{\omega-E_n-\omega_\gamma} - i\pi\delta(\omega-E_n-\omega_\gamma) \tag{4.38}$$

where $\mathcal{P}$ represents the Cauchy principal value. Now the self-energy is split into a real and an imaginary part, both involving an integral over ω_γ. For the imaginary part the integration is simple and leads to

$$\begin{aligned}\text{Im}\,\Sigma_{ij}(\omega) = -4\pi\alpha \sum_{\tau_a\tau_b\tau_a'\tau_b'}\sum_{JM\lambda}\sum_n \left[T_{JM}^{(\lambda)}(\omega-E_n)\right]_{\tau_b'\tau_a'}\left[T_{JM}^{(\lambda)}(\omega-E_n)\right]_{\tau_b\tau_a} \\ \times(\omega-E_n)\left\langle\psi_i\middle|e^\dagger_{\tau_b'}e_{\tau_a'}\middle|\psi_n\right\rangle\left\langle\psi_n\middle|e^\dagger_{\tau_b}e_{\tau_a}\middle|\psi_j\right\rangle\Theta(\omega-E_n).\end{aligned} \tag{4.39}$$

The integral for the real part, on the other hand, is more involved. However, once we have found an expression for Im $\Sigma_{ij}(\omega)$, the corresponding real part Re $\Sigma_{ij}(\omega)$ is related to it via the Kramers-Kronig relation and can be written as [99]

$$\text{Re}\,\Sigma_{ij}(\omega) = \frac{2}{\pi}\mathcal{P}\int_0^\infty \frac{\omega'\text{Im}\,\Sigma_{ij}(\omega')}{\omega'^2-\omega^2}\,\mathrm{d}\omega'. \tag{4.40}$$

At first glance, it does not look like we have simplified the calculation of the real part, since we have transformed one integral into another one, both extending to infinity. However, (4.40) has the advantage that the integrand falls off quickly such that in practice one can restrict the integration domain to a finite interval and still obtain sufficiently converged real parts. Here the drawback is that this interval exceeds the energy window on which the self-energy is needed. Hence it is necessary to determine Im $\Sigma_{ij}(\omega)$ on this extended energy domain.

4.3 Fluorescence yield spectrum

The fluorescence yield (FY) spectrum determines the number of photons with energy ω_γ released following the nuclear decay by EC. The aim of this section is to derive an explicit expression for the FY spectrum. Let us assume that the parent ground state $|\Psi_0\rangle = |\Phi_Z\rangle\otimes|\psi_0\rangle\otimes|0_\nu\rangle\otimes|0_\gamma\rangle$ with parent nuclear wavefunction $|\Phi_Z\rangle$, electronic ground state wave function $|\psi_0\rangle$, zero neutrinos and zero photons transforms by EC into an intermediate state of the form $|\Psi_n\rangle = |\Phi_{Z-1}\rangle\otimes|\psi_n\rangle\otimes|q_\nu',\tau_\nu'\rangle\otimes|0_\gamma\rangle$. Here, $|\Phi_{Z-1}\rangle$ denotes the nuclear wave function after EC where one proton inside the nucleus is transformed into a neutron. $|\psi_n\rangle$ is the (excited)

electronic wave function in the modified nuclear potential, whereas the produced neutrino is characterized by its momentum q'_ν and the set of quantum numbers τ'_ν. As no photon is produced in the EC process, we assume zero photons to be present in the parent ground and intermediate state.

In a second step, the excited intermediate state decays under the emission of a photon. As the intermediate states $|\Psi_n\rangle$ involve no photons, the light-matter interaction can only induce transitions where one photon is created. Therefore, $H_{e\gamma}$ can be replaced by the transition operator $T_{e\gamma}$ introduced in (4.5). Hence, the final state is given by $|\Psi_f\rangle = |\Phi_{Z-1}\rangle \otimes |\psi_f\rangle \otimes |q_\nu, \tau_\nu\rangle \otimes |\mathbf{k}_\gamma, \mu\rangle$ comprising an (excited) electronic wave function $|\psi_f\rangle$, a neutrino with momentum q_ν and quantum numbers τ_ν, as well as a photon with momentum $\mathbf{k}_\gamma$ and polarization μ. According to Fermi's golden rule, this process is described by the second-order decay rate $\Gamma^{(2)}$ [100]:

$$\Gamma^{(2)} \propto \sum_f \left| \sum_n \frac{\langle \Psi_f | T_{e\gamma} | \Psi_n \rangle \langle \Psi_n | T_{\mathrm{EC}} | \Psi_0 \rangle}{E_0 - E_n} \right|^2 \delta(E_0 - E_f) \tag{4.41}$$

Here, $E_0 = Q + E_d$, $E_n = E_d^*(n) + E_\nu$ and $E_f = E_d^*(f) + E_\nu + \omega_\gamma$ are the energies of initial, intermediate and final state, respectively. The sum over $|\Psi_n\rangle$ extends over all excited electronic wavefunctions and all states the neutrino can occupy, i.e. $\sum_n = \sum_{\psi_n} \sum_{q'_\nu, \tau'_\nu}$. The sum over final states additionally involves a photon and can be written as $\sum_f = \sum_{\psi_f} \sum_{\mathbf{k}_\gamma, \mu} \sum_{q_\nu, \tau_\nu} = \sum_{\psi_f} \int \omega_\gamma^2 \mathrm{d}\omega_\gamma \mathrm{d}\Omega_\gamma \sum_{q_\nu, \tau_\nu}$ where the sum over $\mathbf{k}_\gamma$ is transformed into an integral under the assumption of spherical coordinates. Recall that the EC transition operator can be written as a product of nuclear, electronic and neutrino part, $T_{\mathrm{EC}} = T_n T_e T_\nu$. With $T_\nu = \sum_{q''_\nu, \tau''_\nu} \nu^\dagger_{q''_\nu, \tau''_\nu}$ we explicitly find for the neutrino part of the two matrix elements in (4.41)

$$\sum_{q'_\nu, \tau'_\nu} \langle q_\nu, \tau_\nu | q'_\nu, \tau'_\nu \rangle \langle q'_\nu, \tau'_\nu | \sum_{q''_\nu, \tau''_\nu} \nu^\dagger_{q''_\nu, \tau''_\nu} | 0_\nu \rangle = \sum_{q'_\nu, \tau'_\nu} \sum_{q''_\nu, \tau''_\nu} \delta_{q_\nu, q'_\nu} \delta_{\tau_\nu, \tau'_\nu} \delta_{q'_\nu, q''_\nu} \delta_{\tau'_\nu, \tau''_\nu} = 1. \tag{4.42}$$

The action of T_n can be written as $T_n \Phi_Z \propto \Phi_{Z-1}$. Consequently, nuclear and neutrino part can be decoupled from the rest, such that the second-order decay rate is solely determined by the electronic part

$$\begin{aligned} \Gamma^{(2)} \propto \sum_{\psi_f} \sum_{\mu=1}^{2} \int \omega_\gamma \mathrm{d}\omega_\gamma \mathrm{d}\Omega_\gamma \sum_{q_\nu, \tau_\nu} \left| \sum_{\psi_n} \frac{\langle \psi_f | T_{e\gamma} | \psi_n \rangle \langle \psi_n | T_e | \psi_0 \rangle}{Q - \epsilon_n - E_\nu + \mathrm{i}\frac{\gamma}{2}} \right|^2 \\ \times \delta(Q - \epsilon_f - E_\nu - \omega_\gamma) \end{aligned} \tag{4.43}$$

where we introduced $\epsilon_n := E_d^*(n) - E_d$ and $\epsilon_f := E_d^*(f) - E_d$ as the intermediate and final state energies measured from the daughter ground state energy E_d. Note that we added an imaginary part $\mathrm{i}\frac{\gamma}{2}$ in the denominator, in order to take into account the finite lifetime of the intermediate states which is assumed to be the same for all $|\psi_n\rangle$. Furthermore, one ω_γ in the integrand over all photon energies cancels due to the prefactor of $(2\omega_\gamma)^{-1/2}$ in the light-matter interaction (4.6).

As the energy taken away by the neutrino is experimentally not accessible, we in the next step sum over all possible momenta q_ν. This is done by taking the continuum limit as $\sum_{q_\nu} \to \int \mathrm{d}E_\nu E_\nu^2$, where we assume massless neutrinos. By employing the delta function $\delta(Q - \epsilon_f - E_\nu - \omega_\gamma)$, this integral is easily evaluated such that the decay rate becomes:

$$\Gamma^{(2)} \propto \sum_{\psi_f} (Q - \epsilon_f - \omega_\gamma)^2 \sum_{\mu=1}^{2} \int \omega_\gamma \mathrm{d}\omega_\gamma \mathrm{d}\Omega_\gamma \left| \sum_{\psi_n} \frac{\langle \psi_f | T_{e\gamma} | \psi_n \rangle \langle \psi_n | T_e | \psi_0 \rangle}{\epsilon_f + \omega_\gamma - \epsilon_n + \mathrm{i}\frac{\gamma}{2}} \right|^2 \tag{4.44}$$

Our final goal is to derive an expression for the FY spectrum, i.e. to determine the number of photons as a function of their energy ω_γ released subsequent to nuclear decay by EC. We are not interested in one particular polarization or direction. Thus, the integral $\int \mathrm{d}\Omega_\gamma$ and the sum over polarizations $\sum_\mu$ are evaluated by using (4.34) and further exploiting orthonormality of the vector spherical harmonics (4.36). As $\Gamma^{(2)}$ yields the total number of released photons disregarding their energy distribution, the desired quantity is finally obtained by performing the derivative with respect to ω_γ:

$$\frac{\mathrm{d}\Gamma^{(2)}}{\mathrm{d}\omega_\gamma}(\omega_\gamma) \propto \sum_{\psi_f} (Q - \epsilon_f - \omega_\gamma)^2 \omega_\gamma \left| \sum_{\psi_n} \frac{\langle \psi_f | \mathcal{T}_{e\gamma} | \psi_n \rangle \langle \psi_n | T_e | \psi_0 \rangle}{\epsilon_f + \omega_\gamma - \epsilon_n + \mathrm{i}\frac{\gamma}{2}} \right|^2 \tag{4.45}$$

Here, $\mathcal{T}_{e\gamma}$ denotes the polarization- and direction-independent part of photon transition operator $T_{e\gamma}$. Note that the orthonormality relation of the vector spherical harmonics (4.36) employed to evaluate $\int \mathrm{d}\Omega_\gamma$ ensures that different multipoles do not interfere.

It is convenient to express the FY spectrum in terms of a Green's function in analogy to the EC spectrum, but now for a second-order process. For this purpose, we first rewrite $\frac{\mathrm{d}\Gamma^{(2)}}{\mathrm{d}\omega_\gamma}(\omega_\gamma)$ as:

$$\frac{\mathrm{d}\Gamma^{(2)}}{\mathrm{d}\omega_\gamma}(\omega_\gamma) \propto \int \mathrm{d}\omega (Q - \omega)^2 \, \omega_\gamma \sum_{\psi_f} \delta(\omega - \epsilon_f - \omega_\gamma) \left| \sum_{\psi_n} \frac{\langle \psi_f | \mathcal{T}_{e\gamma} | \psi_n \rangle \langle \psi_n | T_e | \psi_0 \rangle}{\epsilon_f + \omega_\gamma - \epsilon_n + \mathrm{i}\frac{\gamma}{2}} \right|^2 \tag{4.46}$$

Replacing the delta function by the response function of a classical damped harmonic oscillator [9]

$$\begin{aligned}\delta(\omega-\epsilon_f-\omega_\gamma) \to & -\lim_{\gamma\to 0^+}\mathrm{Im}\left[\frac{1}{\omega-\epsilon_f-\omega_\gamma+\mathrm{i}\frac{\gamma}{2}}-\frac{1}{\omega+\epsilon_f+\omega_\gamma+\mathrm{i}\frac{\gamma}{2}}\right]\\ \approx & -\lim_{\gamma\to 0^+}\mathrm{Im}\left[\frac{1}{\omega-\epsilon_f-\omega_\gamma+\mathrm{i}\frac{\gamma}{2}}\right]\end{aligned} \tag{4.47}$$

and the sum over the excited states by the resolvent, we finally arrive at the most compact expression for the FY spectrum:

$$\begin{aligned}&\frac{\mathrm{d}\Gamma^{(2)}}{\mathrm{d}\omega_\gamma}(\omega_\gamma)\propto -\mathrm{Im}\int \mathrm{d}\omega (Q-\omega)^2\,\omega_\gamma\\ &\times\left\langle\psi_0\middle|T_e^\dagger\frac{1}{\omega-H_0-\mathrm{i}\frac{\gamma}{2}}\mathcal{T}_{e\gamma}^\dagger(\omega_\gamma)\frac{1}{\omega-H_0-\omega_\gamma+\mathrm{i}\frac{\gamma}{2}}\mathcal{T}_{e\gamma}(\omega_\gamma)\frac{1}{\omega-H_0+\mathrm{i}\frac{\gamma}{2}}T_e\middle|\psi_0\right\rangle\end{aligned} \tag{4.48}$$

Note that all propagators contain an energy-independent broadening γ. As we have discussed before, this parameter can be replaced by a self-energy calculated from first principles including all possible additional decay channels, i.e. fluorescence and Auger-Meitner decay into the continuum (or the chemical environment).

4.4 The example of ^{55}Fe

The aim of this section is to apply the previously derived expressions for the fluorescence self-energy and the FY spectrum to the example of ^{55}Fe. Here we calculate the EC spectrum employing the derived fluorescence self-energy to describe the line-broadening from first principles. As fluorescence decay becomes particularly important at high excitations energies, we focus on the high-energy part of the EC spectrum up to 200 keV. At these energies, the impact of Auger-Meitner decay on the spectral line-shape is small and will be neglected. In addition, we calculate the FY spectrum which in this context provides information about the number of photons released subsequent to EC. Our calculations include a description of radiative EC, a process which is in literature often referred to as internal bremsstrahlung. Radiative EC describes the decay of parent atom into the daughter, an electron-neutrino and a photon. The radiative EC spectrum was first calculated for the case of K capture by Morrison and Schiff in 1940 [101]. A

(relativistic) theory of radiative EC was developed by Martin and Glauber in the 1950s [102, 103]. Although fully relativistic, the theory of Martin and Glauber describes the Coulomb interaction between the electrons on a mean-field level. We will go beyond mean-field and show the implications of the FY spectrum.

^{55}Fe undergoes an *allowed* nuclear EC decay into an excited ^{55}Mn* atom under the emission of an electron-neutrino. The total energy released in the nuclear decay amounts to $Q = 231$ keV [67] and is shared between the electronic excitations and the energy taken away by the neutrino. The differential decay rate $\frac{\mathrm{d}\Gamma}{\mathrm{d}\omega}(\omega)$ presents the rate of decay as a function of the electronic excitations ω of the ^{55}Mn atom. An expression of the differential decay rate for an *allowed* EC decay was derived in section 2.6. For the case of ^{55}Fe it takes the form:

$$\frac{\mathrm{d}\Gamma}{\mathrm{d}\omega} \propto -\mathrm{Im}\left[\langle\Psi_{\mathrm{Fe}}|T_{\mathrm{EC}}^\dagger \frac{1}{\omega + \mathrm{i}\eta^+ - H} T_{\mathrm{EC}}|\Psi_{\mathrm{Fe}}\rangle - \langle\Psi_{\mathrm{Fe}}|T_{\mathrm{EC}}^\dagger \frac{1}{\omega + \mathrm{i}\eta^+ + H} T_{\mathrm{EC}}|\Psi_{\mathrm{Fe}}\rangle\right] \tag{4.49}$$

Here, $|\Psi_{\mathrm{Fe}}\rangle$ denotes the ground state of the ^{55}Fe atom and T_{EC} the transition operator describing the EC process. Note that the ground state energy of the ^{55}Fe atom is set to zero. The Hamiltonian H governing the dynamics subsequent to EC comprises all interactions except the weak interaction which is treated perturbatively and hence already described by T_{EC}. Here we want to study the impact of fluorescence decay on the spectral line-shape. Therefore, we neglect Auger-Meitner decay and work with the Hamiltonian introduced in (4.22),

$$H = H_D + H_C + H_{e\gamma} + H_\gamma \equiv H_0 + H_{e\gamma} + H_\gamma. \tag{4.50}$$

H contains besides the Dirac and Coulomb parts also the light-matter interaction $H_{e\gamma}$ as well as the photon's kinetic energy H_γ. The light-matter interaction allows the system to spontaneously decay by emitting a photon. As the atom afterwards not necessarily ends up in the ^{55}Mn ground state, additional photons may be emitted. However, the light-matter interaction Hamiltonian is linear in the photon creation and annihilation operators, such that the production of more than one photon would involve higher-order processes. Hence, the most dominant contribution stems from the emission of a single photon which we consider here.

Once a core electron has been captured, an electron from one of the outer shells can refill the core hole under the emission of a photon. This process is described by the self-energy (operator) $\Sigma(\omega)$. Following the derivation in section 4.2, the

differential decay rate including fluorescence decay can be written as

$$\frac{\mathrm{d}\Gamma}{\mathrm{d}\omega} \propto -\mathrm{Im}\,(Q-\omega)\sqrt{(Q-\omega)^2-m_\nu^2} \times \left[\langle\psi_{\mathrm{Fe}}|T_e^\dagger \frac{1}{\omega - H - \Sigma(\omega)} T_e|\psi_{\mathrm{Fe}}\rangle - \langle\psi_{\mathrm{Fe}}|T_e^\dagger \frac{1}{\omega + H + \Sigma(\omega)} T_e|\psi_{\mathrm{Fe}}\rangle\right] \tag{4.51}$$

where $|\psi_{\mathrm{Fe}}\rangle$ denotes the (electronic) ground state of the ^{55}Fe atom. T_e is the electronic part of the EC transition operator T_{EC} (2.33) annihilating one of the core electrons in the $ns_{1/2}$ and $mp_{1/2}$ orbitals of ^{55}Fe. The corresponding (relative) capture probabilities are calculated according to (2.31). Note that the infinitesimal imaginary part η^+ is replaced by the self-energy $\Sigma(\omega)$.

As we have shown in section 4.2, the self-energy can be represented as a matrix on the basis of states involving no photons. According to (4.28), the elements of this matrix are given by

$$\Sigma_{ij}(\omega) = \left\langle\psi_i\right| H_{e\gamma} \frac{1}{\omega + i\eta^+ - H_0 - H_\gamma} H_{e\gamma} \left|\psi_j\right\rangle \tag{4.52}$$

where $|\psi_i\rangle$ and $|\psi_j\rangle$ are bound states with zero photons.

Fig. 4.1 illustrates a specific decay channel. The operator T_e in (4.51) can, for example, annihilate a $1s$ core electron. The resulting state, within the Hilbert space of zero photons, has an excitation energy of about 6.5 keV measured from the ^{55}Mn ground state. This state is not an eigenstate of H. It can, for example, interact via the light-matter interaction with an electronic state with a core hole in the $2p$ shell and one additional photon. As the photon can assume any positive energy, there is a continuum of states with a $2p$ core hole and one additional photon as is indicated by the blue density of states in Fig. 4.1. This results in a set of mixed states in terms of photon occupation number. Each state with a $2p$ core hole and one photon gets a small admixture of the state with a $1s$ core hole without photon, as indicated in purple. The process depicted in Fig. 4.1 can be described by a function, i.e. a single matrix element of the form (4.52). For a state with core hole in $1s$ and no photon we obtain according to (4.32)

$$\Sigma_{\underline{1s}}^{2p}(\omega) \propto \int_0^\infty \left\langle\psi_{\underline{1s}}\right| T_{e\gamma}^\dagger(\mathbf{k}_\gamma) \frac{1}{\omega + i\eta^+ - \omega_{\underline{2p}} - \omega_\gamma} T_{e\gamma}(\mathbf{k}_\gamma) \left|\psi_{\underline{1s}}\right\rangle \omega_\gamma \mathrm{d}\omega_\gamma \tag{4.53}$$

where $T_{e\gamma}(\mathbf{k}_\gamma)$ is the light-matter transition operator introduced in (4.6) which depends on the photon's wave vector $\mathbf{k}_\gamma$ and therefore also on its energy ω_γ. The

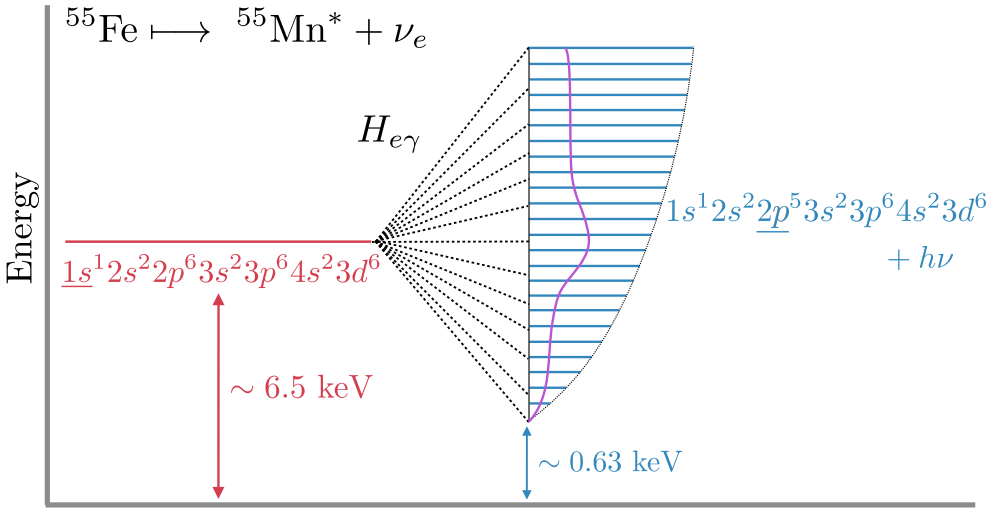

Figure 4.1: Sketch of a specific decay channel subsequent to nuclear decay by EC of an ^{55}Fe atom. The energy is labeled with respect to the ground-state energy of the ^{55}Mn atom. At about 6.5 keV excitation energy (red line) one finds a state with a core hole in $1s$. This state is not an eigenstate of the Hamiltonian, but can via the light-matter interaction $H_{e\gamma}$ interact with states with for example a $2p$ core hole and one additional photon (blue). These states start at about 0.63 keV, the excitation energy of a $2p$ core hole and form a continuum due to all possible photon energies. Each state with $2p$ core hole plus photon gets an admixture of a state with $1s$ core hole and no photon (purple).

matrix elements of $H_{e\gamma}$ (or $T_{e\gamma}$) scale as the Fourier transform of the product of these orbitals which are in turn strongly energy-dependent.

Fig. 4.2 shows the imaginary part of the fluorescence self-energy (4.39) on a double-logarithmic plot for several decay channels starting from the capture of a $1s$ core electron in ^{55}Fe. The displayed self-energies exhibit a strong energy-dependence and change by several orders of magnitude on an energy window of roughly 200 keV.

At resonance, we can compare the imaginary part of the self-energy with Hartree-Slater (HS) [104] and Hartree-Fock (HF) [105] calculations. These values are indicated by blue and green dots, respectively, and are in good agreement with the presented calculations. Note that the literature values correspond to the full width at half maximum and can thus be compared to twice the imaginary part

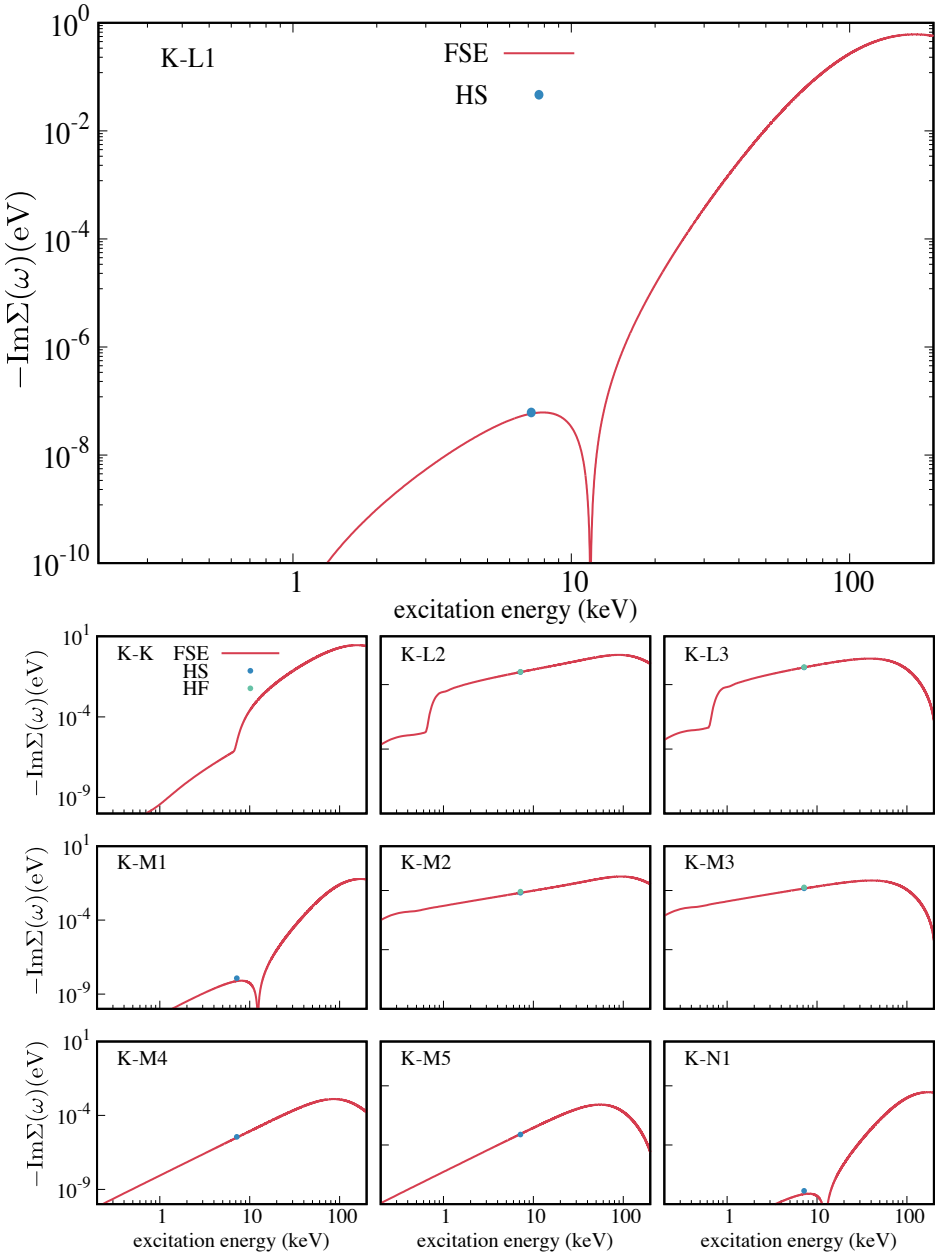

Figure 4.2: Energy-dependence of the imaginary part of the fluorescence self-energy (FSE) for different decay channels after the capture of a 1s electron in ^{55}Fe. At resonance, we can compare the imaginary part of the self-energy with Hartree-Slater (HS) [104] and Hartree-Fock (HF) [105] calculations. These values are indicated by blue and green dots, respectively. For the $K-K$ channel no literature value was found. Note the logarithmic vertical axis.

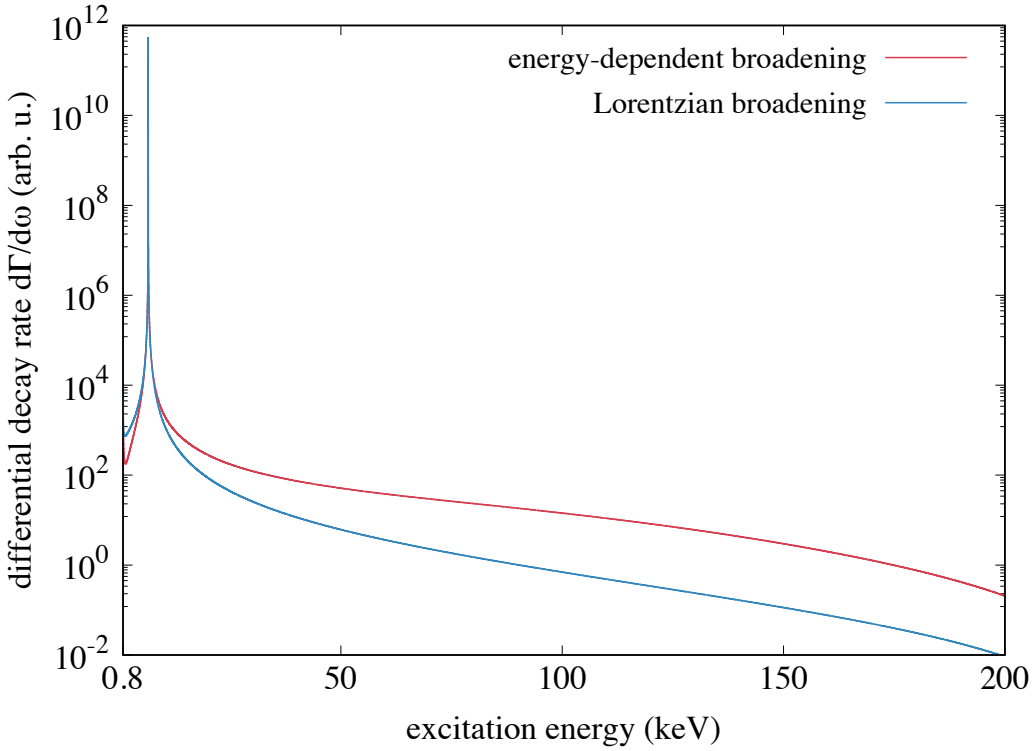

Figure 4.3: High-energy part of the EC spectrum of ^{55}Fe for a constant Lorentzian line-broadening (blue) and an energy-dependent broadening due to fluorescence decay (red). The energy-dependence of the latter leads to an increase of more than one order of magnitude in the ionizing radiation with energies in the range from $50 - 200$ keV. Close to the main resonance, the differences between the two spectra are modest.

of the self-energy. Also note that no literature value was found for the $K - K$ transition related to a spin-flip of the $1s$ core hole.

Remarkably, we observe a strong increase of the self-energy above the binding energies of the core electrons. This is directly related to a strong increase in the transition matrix element, in particular due to magnetic dipole transitions. Although the fluorescence self-energy of a core excited atomic state is strongly energy-dependent over an energy window of several keV, this does not imply that the line-shape completely deviates from a Lorentzian. The imaginary-part of the self-energy is of the order of eV, whereas its changes on this energy scale are small enough, such that at resonance the line-shape is approximately given by a Lorentzian.

Fig. 4.3 shows the high-energy part of the EC spectrum of ^{55}Fe as function of

ω, the energy stored in terms of electronic excitations, which is approximately equal to the energy of the ionizing radiation released in the EC decay. The blue curve displays the EC spectrum under the assumption of a constant self-energy. The red curve, on the other hand, shows the spectrum for an energy-dependent self-energy broadening. For an energy window of several hundred eV around the resonance, the differences between the two theories are tiny and hardly visible in the spectra. However, in the range of $50 - 200$ keV where high-energy ionizing radiation is emitted, we observe an increase of events by more than one order of magnitude in the case of the energy-dependent self-energy. In consequence, this also affects the total amount of ionizing radiation which roughly corresponds to the first moment of the differential decay rate, i.e. the integral $\int_0^\infty \omega \frac{\mathrm{d}\Gamma}{\mathrm{d}\omega} \mathrm{d}\omega$. As most events happen close to the resonance, we only find a modest change of less than one per mille for the total energy released in terms of ionizing radiation.

Fluorescence yield spectrum

Following nuclear decay by EC, the atom can, for example, first evolve in time due to the electromagnetic interactions between the electrons and occupy (excited) bound states which include no photon. These states, referred to as intermediate states, can spontaneously decay into (excited) states with modified electronic configuration plus one additional photon. As discussed in section 4.3, such processes are described by the second-order decay rate. From this expression one can derive the fluorescence yield (FY) spectrum by integrating over all neutrino energies E_ν, or equivalently, over all excitation energies $\omega = Q - E_\nu$. The FY spectrum provides information about the number of photons released with energy ω_γ. Following the derivation presented in section 4.3, the final form of the FY spectrum can be written in terms of a Green's function (4.48)

$$\begin{aligned}\frac{\mathrm{d}\Gamma^{(2)}}{\mathrm{d}\omega_\gamma}(\omega_\gamma) \propto -\mathrm{Im} \int \mathrm{d}\omega (Q-\omega)^2\, \omega_\gamma \left\langle \psi_{\mathrm{Fe}} \middle| T_e^\dagger \frac{1}{\omega - H_0 - \Sigma^\dagger(\omega)} \right. \\ \left. \times\, \mathcal{T}_{e\gamma}^\dagger(\omega_\gamma) \frac{1}{\omega - H_0 - \omega_\gamma - \Sigma(\omega)} \mathcal{T}_{e\gamma}(\omega_\gamma) \frac{1}{\omega - H_0 - \Sigma(\omega)} T_e \middle| \psi_{\mathrm{Fe}} \right\rangle\end{aligned} \tag{4.54}$$

where the Lorentzian broadening $\mathrm{i}\frac{\gamma}{2}$ is replaced by the fluorescence self-energy $\Sigma(\omega)$. The operator $\mathcal{T}_{e\gamma}(\omega_\gamma)$ denotes the polarization- and angular independent part of the light-matter transition operator, T_e the electronic part of the EC transition operator. The Hamiltonian H_0 comprises the Dirac Hamiltonian and the

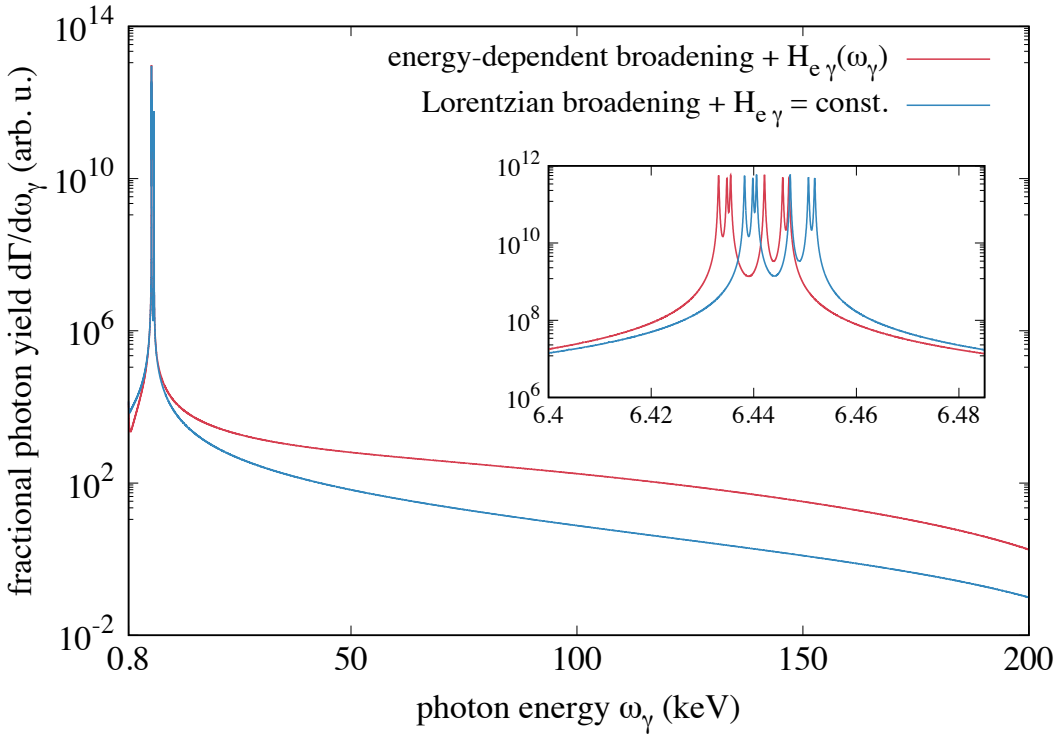

Figure 4.4: Calculated high-energy part of the FY spectrum of ^{55}Fe. The red curve assumes an energy-dependent broadening due to fluorescence decay and an energy-dependent Hamiltonian $H_{e\gamma}(\omega_\gamma)$. The blue curve is calculated for a constant Lorentzian line-broadening and energy-independent Hamiltonian $H_{e\gamma} = \text{const}$. The latter is evaluated at the energy difference of the respective coupled states. The inset shows a section of the FY spectrum at $\approx$ 6.44 keV. Photons at this energy are produced in the transition of a $3p$ electron into the $1s$ core hole resulting in a final state with one hole in $3p$ plus additional photon. Due to the $3p - 3d$ Coulomb interaction multiplets are formed leading to six peaks split by energies on the Rydberg scale.

Coulomb interaction.

Fig. 4.4 displays the FY spectrum between $0.8 - 200$ keV and a section around $\approx$ 6.44 keV. The red curve is calculated for an energy-dependent broadening and energy-dependent light-matter interaction. For the blue curve a constant Lorentzian broadening and energy-independent light-matter interaction is assumed. In this case, $H_{e\gamma}$ (or $\mathcal{T}_{e\gamma}$) is evaluated at the energy difference of the respective coupled states. If, for example, a $2p$ electron fills a $1s$ core hole, the

transition operator $\mathcal{T}_{e\gamma}$ is evaluated at $\omega_\gamma = \omega_{\underline{1s}} - \omega_{\underline{2p}}$, where $\omega_{\underline{1s}}$ and $\omega_{\underline{2p}}$ are the energies of the states with core holes in $1s$ and $2p$, respectively.

A comparison of the FY spectrum shown in Fig. 4.4 and the EC spectrum displayed in Fig. 4.3 reveals that the two spectra resemble each other. While the agreement is good at very high energies, differences become visible close to the resonances at lower energies. These emerge due to the fact that in the first-order spectrum the fluorescent decay of an excited state into a second excited state at lower excitation energy cannot be resolved.

Our result for the FY spectrum employing the energy-dependent broadening, i.e. the red curve displayed in Fig. 4.4, is in good agreement with theoretical calculations based on the Martin and Glauber theory [102, 103] as well as with experimental measurements [106]. Martin and Glauber employ a fully relativistic framework, but treat the mutual Coulomb repulsion between the electrons only on a mean-field level. We go beyond this level of theory and take into account the full Coulomb interaction. This leads to differences close to the resonances. An example of a specific decay channel where these differences become visible is displayed in the inset of Fig. 4.4. Here the FY spectrum at photon energies of ≈ 6.44 keV is shown. These photons are produced in the decay of a $3p$ electron into a $1s$ core hole created in the EC process leading to a final state with one hole in $3p$ and additional photon. Due to the Coulomb interaction between the $3p$ shell and the valence $3d$ shell, this state is split into multiplets. This explains the six peaks for the blue and red curve shown in the inset of Fig. 4.4 which are split by energies on the Rydberg scale. In addition, the $3p$ shell is split due to a finite spin-orbit coupling into $3p_{1/2}$ and $3p_{3/2}$. However, the splitting due to spin-orbit interaction is much smaller compared to the multiplet splitting. On a pure mean-field level, the multiplet splitting would not be visible. Hence, one would only observe a very small splitting due to a finite spin-orbit coupling.

Although the number of peaks observed for the blue and red curve displayed in the inset of Fig. 4.4 is the same, the peak positions for the latter are shifted to lower photon energies. This is caused by the real part of the self-energy shifting the resonance with core hole in the $1s$ shell by several eV towards lower excitation energies. On the other hand, the calculation leading to the blue curve assumes a vanishing real part, such that these resonances are not shifted.

4.5 Conclusion

In conclusion, we developed an *ab initio* description of the line-broadening due to fluorescence decay in terms of a self-energy formalism. This enables for a computationally efficient way to include additional photons in the Hilbert space. Starting from a multipole expansion of the (relativistic) light-matter interaction, we expressed the fluorescence self-energy in terms of the individual multipole transitions. Thus, the effect of single decay channels on the spectral line-shape can be analyzed.

Furthermore, we derived an expression for the FY spectrum based on Green's functions. This allows accurate prediction of the number of photons released and their energy following nuclear decay by EC.

As the formalism is general in its form, it can also be used to derive the electron yield, i.e. an expression for the number of electrons subsequent to EC. In this case the light-matter interaction Hamiltonian $H_{e\gamma}$ must be replaced by the Coulomb repulsion coupling bound to unbound states. A detailed knowledge of the electron yield spectrum is of great interest, for example in radiotherapy [4]. Therefore, it may be interesting in future studies to calculate the electron yield for established or potential new isotopes suitable for this purpose.

In section 4.4, we applied the derived concepts to determine the high-energy EC spectrum of ^{55}Fe. We calculated the spectrum for an energy-dependent broadening by means of the fluorescence self-energy and for an energy-independent Lorentzian broadening. A comparison of these two spectra revealed that close to a resonance, the differences between the two theories are modest. At very high excitation energies of > 50 keV, however, our calculations predict at least one order of magnitude more intensity for the energy-dependent broadened spectrum than for the case of a Lorentzian broadening. This clearly demonstrates the significance of an energy-dependent line-broadening calculated from first principles for an accurate description of EC spectra in general. An analysis of the corresponding matrix elements proved that this high-energy photon excess results particularly from magnetic dipole transitions. The difference in total amount of ionizing radiation between these two theories is less than one per mille.

Finally, we calculated the high-energy FY spectrum of ^{55}Fe. At high energies, our results are in good agreement with theoretical as well as experimental results found in the literature. However, close to the resonances at lower energies, differences compared to other theories become visible. While these theories work on a mean-field level, we calculate the electronic interactions using the full Coulomb

interaction. Hence, single resonances get split by energies on the Rydberg scale not captured on the mean-field level.

5 Optimized single-particle states for the nuclear many-body problem

Most of the unstable atomic nuclei decay by beta- or EC transitions in which a proton (neutron) is transformed into a neutron (proton). These decays involve the nuclear many-body wave functions of the initial and final state, whose accurate calculation is one of the major concerns in nuclear structure theory. To address this problem, several approaches based on phenomenological interactions or mean-field approximations have been employed [107, 108]. However, these theoretical models often lead to inaccurate descriptions which are not in accordance with experimental observations. Only recently, it could be shown on the example of beta decay rates that this discrepancy can be strongly reduced by using an *ab initio* description of the nuclear many-body problem [109].

A prominent example, which strongly depends on the knowledge of an accurate nuclear matrix element, is the conjectured neutrinoless double-beta decay ($0\nu\beta\beta$) [54, 110], in which the parent nucleus decays into its daughter with two fewer neutrons and two more protons, while emitting two electrons but no neutrino. Whether the neutrino is a Majorana particle, i.e. its own anti-particle, or a Dirac particle is still an open question in particle physics. Hence, the confirmation of the existence of the $0\nu\beta\beta$ decay, for which an accurate knowledge of the nuclear matrix element is indispensable, would imply the neutrino to be its own anti-particle, i.e. a Majorana particle and thereby solve this puzzle. *Ab initio* nuclear structure calculations seem to be a very promising approach to provide nuclear matrix elements with the desired accuracy necessary to achieve this goal [54].

Although very auspicious, such calculations are also challenging as they involve two- as well as three-nucleon interactions and besides require very large model spaces. For this reason, *ab initio* descriptions of the nuclear many-body problem for heavy nuclei are (currently) infeasible. Up to today, the upper end of the nuclear chart which could be described from first principles is set by ^{100}Sn [111] with the future goal to extent this limit to higher mass numbers.

The starting point of many *ab initio* computations is the choice of a suitable

single-particle basis. Since the associated single- and consequently also the many-particle space is infinite-dimensional, some kind of truncation must be employed in order to perform numerical calculations. However, this leads to the undesirable fact that physical observables turn out to depend on the basis set parameters. A key criterion in choosing a suitable single-particle basis is to reduce this dependence as much as possible while ensuring rapid convergence [112].

Here we want to focus on one particular *ab initio* approach, the so-called no-core shell model (NCSM) [113, 114] in which the nucleus is described by a set of point-like, interacting nucleons. The basic idea of the NCSM is to express the many-body states in terms of Slater determinants and to convert the many-body Schrödinger equation into a Hamiltonian matrix eigenvalue problem. It has only recently been shown for the NCSM [112, 115] that a single-particle basis of natural orbitals constructed in a preceding calculation, one can not only minimize the dependence on basis set parameters, but also reduce the complexity of the many-body problem, which ultimately translates into much faster convergence. This constitutes a promising improvement to extend *ab initio* calculations to heavier nuclei.

The goal of this chapter is to present a novel iterative method to optimize the single-particle basis set, formulated for the NCSM and based in its fundamental idea on the concept of natural orbitals. To do so, we first provide a brief overview of the status quo in section 5.1 by introducing two important and commonly used basis sets in nuclear structure theory, namely the harmonic oscillator and the natural orbital basis. Then, in section 5.2, we present our novel iterative scheme by providing a detailed explanation of the underlying algorithm. In section 5.3, we finally discuss advantages of the introduced approach over conventional methods and possible implications for *ab initio* nuclear structure calculations.

5.1 The status quo

The basic assumption in low-energy nuclear many-body calculations is that the nucleus is made up of point-like interacting protons and neutrons. The starting point in the NCSM is the intrinsic Hamiltonian [114]

$$H = T_{\mathrm{rel}} + V \tag{5.1}$$

which is given by the relative kinetic energy T_{rel} and the interaction V between the nucleons. The latter typically involves two- as well as three-nucleon interactions. The relative kinetic energy consists of a one- and two-body operator [114]

$$T_{\text{rel}} = \left(1 - \frac{1}{A}\right) \sum_{i}^{A} \frac{\mathbf{p}_i^2}{2m_N} - \frac{1}{A} \sum_{i<j}^{A} \frac{\mathbf{p}_i \cdot \mathbf{p}_j}{m_N} \tag{5.2}$$

where $\mathbf{p}_i$ is the momentum of the i-th nucleon and m_N the (average) nucleon mass. Note that T_{rel} depends on the number of nucleons A leading to an overall A-dependent intrinsic nuclear Hamiltonian.

5.1.1 Harmonic oscillator eigenstates

Usually, the first step in NCSM calculations is to express the intrinsic nuclear Hamiltonian (5.1) on a basis of harmonic oscillator (HO) wave functions which are eigenstates of the well-known Hamiltonian

$$h(\omega) = \frac{p^2}{2m_N} + \frac{m_N \omega^2 r^2}{2} \tag{5.3}$$

where ω denotes the oscillator frequency. The corresponding eigenenergies, which are identical for protons and neutrons, are given by $\epsilon_{nl} = (2n + l + \frac{3}{2})\omega$ and are fully characterized by the quantum number $e = (2n + l)$ [116].

Due to their localized nature and simple analytic form, HO states are widely used in nuclear physics and are well suited to describe the atomic nucleus [117]. However, the convergence of physical observables like for example the ground state energy or the charge radius is relatively slow. In addition, these observables turn out to be strongly dependent on the basis set parameter, i.e. the oscillator frequency ω, which hinders an extraction of such observables from theoretical calculations [112]. The reason for this is that HO wave functions show the wrong asymptotic behavior, since they fall off like Gaussians at large distances, while the correct behavior corresponds to that of bound states in an attractive potential of finite range, which typically fall off exponentially [118]. Consequently, many wave functions are needed to correctly describe the long-range behavior of the states, which is reflected in a fast growing many-body space and finally explains the slow convergence. This becomes a major drawback when systems with a larger number of nucleons are described on an HO basis and eventually overrules the advantages of this basis.

5.1.2 Natural orbitals

A second single-particle basis set are the so-called natural orbitals (NOs), originally proposed by Löwdin and Shull in the 1950s [119, 120]. The goal was to find single-particle states that are optimally matched to the structure of the underlying many-particle states, i.e. to describe them by only a few Slater-determinants. Since then, NOs have been used primarily in quantum chemistry [121], atomic [122] and solid state physics [123], but in recent years have received increasing attention in the field of nuclear theory [112, 115, 118, 124].

The central object for the determination of the NOs is the single-particle density matrix of the many-body ground state $|\psi_0\rangle$,

$$\rho_{\tau\tau'} = \langle\psi_0|a_\tau^\dagger a_{\tau'}|\psi_0\rangle \tag{5.4}$$

where $\tau = \{n, l, j, m, t\}$ represent the single-particle quantum numbers. Here n is the radial quantum number, l the angular momentum, j the total angular momentum with projection m and t the isospin projection quantum number. NOs are defined as the eigenstates of $\rho_{\tau\tau'}$, whereas the associated eigenvalues give the (mean) occupation numbers. NOs are designed to minimize the number of Slater-determinants required to represent the many-particle wave function $|\psi_0\rangle$ and include additional contributions originating from high-lying orbitals that would be unoccupied at the pure mean-field level. These turn out to be of great significance which ultimately leads to faster convergence compared to alternative basis sets [112, 115, 123].

However, it is important to realize that before we can determine the density matrix, we must first calculate the many-body ground state $|\psi_0\rangle$. For most relevant systems, this is beyond the realm of possibility, since it would require solving the full many-body Schrödinger equation. Fortunately, it has been shown in older works from quantum chemistry [125] that an approximate ground state taking into account at least parts of the correlations beyond mean-field, is already sufficient to optimize the single-particle basis. However, it is expectable that the closer the approximate ground state approaches the exact one, the greater the benefit of the basis optimization. Therefore, it is desirable to determine the ground state as accurately as possible. The prevailing approach in nuclear theory is starting from the Hartree-Fock (HF) state obtained in a previous calculation and adding correlations by many-body perturbation theory [112, 115].

Once an (approximate) ground state has been found, one can construct the den-

sity matrix. For the rotationally symmetric nuclear problem, the many-particle ground state is characterized by a definite total angular momentum J with projection M and parity P. Such a state is generally given by a superposition of various Slater-determinants composed of single-particle states of the form $|nljmt\rangle$. If one were to diagonalize the density matrix without additional constraints, then the resulting NOs would generally be incompatible with the underlying symmetries. For an initial state with definite J, for example, the density matrix generally couples states with different j, i.e. the total angular momentum of the NOs would not be a good quantum number [118]. To ensure that the NOs have well-defined isospin projection, angular- and total angular momentum, we thus diagonalize and subsequently transform the respective (ljt)-blocks of the density matrix separately. Note that the rotation matrix can only connect states with identical magnetic quantum number m. Due to the underlying symmetries each of the individual (ljt)-blocks is independent of m. In consequence, the rotation matrices that transform HO wave functions to NOs are identical for each magnetic substate with $m = -j, \ldots, j$ that belong to a given j. A more detailed discussion can be found in [118].

5.2 An outlook to the future − generalized natural orbitals

The aim of this chapter is to present a novel approach to the optimization of the single-particle basis, which in its basic idea relies on the concept of the previously introduced NO. However, the fundamental difference from the usual method is that the basis is not optimized in one step, but iteratively, i.e., one first optimizes a sub-set of single-particle states and then gradually adds the remaining orbitals after the included ones have been pre-optimized. To obtain (optimized) states with the correct symmetry in the ordinary NO approach, each (ljt)-block of the density-matrix must be diagonalized separately. For simplicity, we from now on do not distinguish between protons and neutrons which allows us to ignore the isospin projection t. Hence, we focus on (lj)-blocks in the density matrix whose size will determine the (minimal) number of states included in each iteration step.

In the following, we specify our method and present the relevant steps of the underlying algorithm. For this purpose, we assume the nuclear Hamiltonian (5.1)

to be given on a basis of HO eigenstates. Different basis sets, for example HF wave functions, work equally well. In practice, we have to work on a finite basis and truncate the single-particle space. Since each HO is characterized by the number of oscillator quanta e, this is done by discarding all states with $e > e_{\max}$. To keep the notation short, we introduce the quantum number κ, where $\kappa = -l-1$ if $j = l+1/2$ and $\kappa = l$ if $j = l-1/2$, which enables us to label the sub-sets by only one quantum number instead of two.

Instead of setting up the full density matrix of the (approximate) ground state, we assume in the first iteration step that the A nucleons may only occupy single-particle states with one specific κ, i.e., we restrict ourselves to those states of a single sub-block of the density matrix. Since the $0s_{1/2}$-orbital is typically the most occupied one, we choose to start with $s_{1/2}$-orbitals characterized by $\kappa_1 = -1$. Hence, the single-particle Hilbert space is given by

$$V^{(1)} = \left\{ |n\kappa_1\rangle \;\middle|\; n = 0, \ldots, \frac{e_{\max} - l(\kappa_1)}{2} \right\}. \tag{5.5}$$

where n_1 are the radial quantum numbers of the HO states with κ_1. Here the maximal value of n is determined by the chosen truncation $e_{\max}$.

In the next step we diagonalize the corresponding Hamiltonian labeled by $H^{(1)}$ to determine the many-body ground state $|\psi_0^{(1)}\rangle$. This, however, is only achievable for larger nuclei if one removes (unimportant) configurations from the many-particle basis, i.e. the Slater determinants which can be constructed from single-particle states with $e \leq e_{\max}$. In the traditional NO approach starting from the HO basis, for this purpose, one uses the so-called $N_{\max}$-truncation scheme [114]. Every many-particle basis state is characterized by a total of $N = (e_1 + \cdots + e_A)$ HO oscillator quanta. Let N_0 denote the number of quanta in the lowest allowed configuration, then N can be written as $N = N_0 + N_{\text{ex}}$, where N_{ex} are the number of excited quanta with respect to N_0. In the $N_{\max}$-truncation scheme all Slater-determinants with $N_{\text{ex}} > N_{\max}$ are removed from the many-particle basis. Although the $N_{\max}$-truncation scheme is applicable in the first iteration step where we start from a sub-set solely given by HO states, it loses its validity in all further iteration steps.

The symmetry-adapted NOs we want to work with are given by linear combinations of the chosen single-particle states (here HO wave functions) with the same κ. For this reason, their radial quantum number n is not well-defined, which makes an assignment of oscillator quanta e in the context of NOs meaningless. Instead, we truncate the many-particle basis by neglecting all configurations with

coefficients ϵ smaller than a predefined threshold value $\epsilon^{(1)}_{\text{min}}$, i.e. we remove all Slater-determinants with $\epsilon < \epsilon^{(1)}_{\text{min}}$. Once we have found the ground state for a given $\epsilon^{(1)}_{\text{min}}$, we set up the density matrix

$$\rho^{(1)} = \left(\rho^{(1)}_{n,\kappa_1;n',\kappa_1} \right) \tag{5.6}$$

where $\rho^{(1)}_{n,\kappa_1;n',\kappa_1} = \langle \psi^{(1)}_0 | a^\dagger_{n,\kappa_1} a_{n',\kappa_1} | \psi^{(1)}_0 \rangle$. The eigenvectors of $\rho^{(1)}$ define a unitary transformation $u^{(1,\kappa_1)}$

$$|m\kappa_1\rangle^{(1)} = \sum_n u^{(1,\kappa_1)}_{m,n} \, |n\kappa_1\rangle \tag{5.7}$$

with the help of which the HO states $|n\kappa_1\rangle$ are transformed to their NO representation $|m\kappa_1\rangle^{(1)}$. Here the quantum number m labels the transformed radial part (not to be confused with the magnetic quantum number), whereas the superscript in $|\ldots\rangle^{(1)}$ indicates the (first) iteration step. Note that $u^{(1,\kappa_1)}$ does not mix HO states with different magnetic number. Hence, the states $|n\kappa_1\rangle$ and $|m\kappa_1\rangle^{(1)}$ have the same magnetic quantum number.

Since some NOs are hardly occupied in $|\psi^{(1)}_0\rangle$, these states can be optionally removed from the basis. In practice, this is realized by introducing a threshold value $n^{(1)}_{\text{min}}$. States with an occupation smaller than $n^{(1)}_{\text{min}}$ are excluded from the basis, while those with larger occupation are kept. In this way the single-particle basis is reduced which is ultimately reflected in a smaller number of matrix elements and thus accelerated convergence. As we only want to remove unimportant states, the computational accuracy remains practically unchanged compared to the original set of states. However, one should keep in mind that orbitals which have a low occupation number at a particular iteration step and therefore appear unimportant, might be more occupied at a later time and thus become more relevant.

Note that if any NOs have been removed from the basis, $u^{(1,\kappa_1)}$ is adjusted accordingly, i.e. the corresponding rows/columns are removed. Afterwards, the transformation $u^{(1,\kappa_1)}$ is applied to all matrix elements of the nuclear Hamiltonian H involving states with κ_1. If the nucleons could only occupy single-particle states characterized by κ_1, then we would have already found an optimized basis set. However, we know that in reality things are more complicated and require an inclusion of single-particle states with different κ as well.

Therefore, in the second iteration step we extend the (optimized) basis set consisting of the NOs $|m\kappa_1\rangle^{(1)}$ by adding HO states with identical quantum number

$\kappa_2 = 1$, i.e. the $p_{1/2}$-orbitals. Thus, the single-particle Hilbert space of the second iteration step is given by

$$V^{(2)} = \left\{ |m\kappa_1\rangle^{(1)} \right\} \bigcup \left\{ |n\kappa_2\rangle \mid n = 0, \ldots, \frac{e_{\max} - l(\kappa_2)}{2} \right\}. \tag{5.8}$$

The associated Hamiltonian $H^{(2)}$ includes, in addition to the parts that contain solely orbitals with κ_1 or κ_2, also terms that involve both. Note that all matrix elements of $H^{(2)}$ involving orbitals with κ_1 are transformed by using $u^{(1,\kappa_1)}$. As in the previous iteration step, we now determine the density matrix of the ground state of $H^{(2)}$ for a chosen $\epsilon^{(2)}_{\min}$ which is labeled by $|\psi^{(2)}_0\rangle$, and neglect those parts that couple states with κ_1 and κ_2, i.e. the off-diagonal elements, since these would lead to NOs incompatible with the required symmetry properties. Hence, the density matrix of the second iteration step takes the block-diagonal form

$$\rho^{(2)} = \begin{pmatrix} \rho^{(2)}_{m,\kappa_1;m',\kappa_1} & 0 \\ 0 & \rho^{(2)}_{n,\kappa_2;n',\kappa_2} \end{pmatrix} \tag{5.9}$$

where the first block, $\rho^{(2)}_{m,\kappa_1;m',\kappa_1} = \langle\psi^{(2)}_0| a^\dagger_{m,\kappa_1} a_{m',\kappa_1} |\psi^{(2)}_0\rangle$, includes the previously optimized orbitals with κ_1, while the second one, $\rho^{(2)}_{n,\kappa_2;n',\kappa_2} = \langle\psi^{(2)}_0| a^\dagger_{n,\kappa_2} a_{n',\kappa_2} |\psi^{(2)}_0\rangle$, comprises the yet fully unadapted HO wave functions $|n\kappa_2\rangle$. The eigenvectors of $\rho^{(2)}$ define a unitary transformation $u^{(2)}$ that transforms all states, i.e. $|m\kappa_1\rangle^{(1)}$ and $|n\kappa_2\rangle$, to their NO representation. Note that the first block of $\rho^{(2)}$ involving the previously optimized states $|m\kappa_1\rangle^{(1)}$ is not diagonal due to a different ground state and is therefore re-optimized. Due to the block-diagonal structure of $\rho^{(2)}$, the rotation of each sub-block can be performed separately. Let $u^{(2,\kappa_1)}$ and $u^{(2,\kappa_2)}$ denote the parts of $u^{(2)}$ acting on $|m\kappa_1\rangle^{(1)}$ and $|n\kappa_2\rangle$, respectively, then the transformation is explicitly given by

$$\begin{aligned} |m\kappa_1\rangle^{(2)} &= \sum_{m'} u^{(2,\kappa_1)}_{m,m'} |m'\kappa_1\rangle^{(1)} \\ |m\kappa_2\rangle^{(2)} &= \sum_{n} u^{(2,\kappa_2)}_{m,n} |n\kappa_2\rangle \,. \end{aligned} \tag{5.10}$$

As before, m labels the radial quantum number of the states optimized in the current iteration step which are either obtained from previously optimized states or from the yet fully unadapted HO wave functions. Then $u^{(2)}$ is applied to the nuclear Hamiltonian with the possibility to remove unimportant states from the single-particle basis by introducing a threshold $n^{(2)}_{\min}$.

In this way, we can iteratively include and optimize all other single-particle states up to $\kappa_{i_{\max}}$ which is achieved in $i_{\max} - 2$ further iteration steps where $i_{\max}$ is determined by the number of possible κ-values compatible with the given $e_{\max}$. In each iteration we choose values for $n_{\min}^{(i)}$ and $\epsilon_{\min}^{(i)}$ that define the truncation on the single- and many-particle level, respectively. In the last iteration step we end up with a single-particle Hilbert space of the form

$$V^{(i_{\max})} = \left\{ |m\kappa_1\rangle^{(i_{\max}-1)} \right\} \bigcup \cdots \bigcup \left\{ |n\kappa_{i_{\max}}\rangle \;\middle|\; n = 0, \ldots, \frac{e_{\max} - l(\kappa_{i_{\max}})}{2} \right\} \tag{5.11}$$

involving all previously optimized states with $\kappa = \kappa_1, \ldots, \kappa_{i_{\max}-1}$ and HO states with $|n\kappa_{i_{\max}}\rangle$. Diagonalization of the corresponding Hamiltonian $H^{(i_{\max})}$ leads to the ground state $|\psi_0^{(i_{\max})}\rangle$ which enables us to set up the density matrix

$$\rho^{(i_{\max})} = \begin{pmatrix} \rho^{(i_{\max})}_{m,\kappa_1;m',\kappa_1} & 0 & \cdots & 0 \\ 0 & \rho^{(i_{\max})}_{m,\kappa_2;m',\kappa_2} & \cdots & 0 \\ \vdots & \vdots & \ddots & \vdots \\ 0 & 0 & \cdots & \rho^{(i_{\max})}_{n,\kappa_{i_{\max}};n',\kappa_{i_{\max}}} \end{pmatrix}. \tag{5.12}$$

Here $\rho^{(i_{\max})}_{m,\kappa_j;m',\kappa_j} = \langle\psi_0^{(i_{\max})}|a^\dagger_{m,\kappa_j} a_{m',\kappa_j}|\psi_0^{(i_{\max})}\rangle$ are the sub-blocks of the density matrix for the last iteration step $i_{\max}$ involving the states optimized in the previous iteration steps where $j = 1, \ldots, i_{\max} - 1$. The last block of $\rho^{(i_{\max})}$ contains the HO states with $|n\kappa_{i_{\max}}\rangle$ and reads $\rho^{(i_{\max})}_{n,\kappa_{i_{\max}};n',\kappa_{i_{\max}}} = \langle\psi_0^{(i_{\max})}|a^\dagger_{n,\kappa_{i_{\max}}} a_{n',\kappa_{i_{\max}}}|\psi_0^{(i_{\max})}\rangle$. The eigenvectors of $\rho^{(i_{\max})}$ define a unitary transformation $u^{(i_{\max},\kappa_i)}$ for every sub-set of states labeled by $i = 1, \ldots, i_{\max}$ such that

$$\begin{aligned} |m\kappa_1\rangle^{(i_{\max})} &= \sum_{m'} u^{(i_{\max},\kappa_1)}_{m,m'} \, |m'\kappa_1\rangle^{(i_{\max}-1)} \\ |m\kappa_2\rangle^{(i_{\max})} &= \sum_{m'} u^{(i_{\max},\kappa_2)}_{m,m'} \, |m'\kappa_2\rangle^{(i_{\max}-1)} \\ &\vdots \\ |m\kappa_{i_{\max}}\rangle^{(i_{\max})} &= \sum_{n} u^{(i_{\max},\kappa_{i_{\max}})}_{m,n} \, |n\kappa_{i_{\max}}\rangle \end{aligned} \tag{5.13}$$

which transforms all single-particle basis states to a set of fully optimized NOs. After the $i_{\max}$-th iteration, the algorithm stops and we obtain in addition to a fully optimized set of single-particle states the nuclear Hamiltonian on this basis. Although constructed in a different way, our single-particle states still show a strong similarity to the ordinary NOs, which is why we refer to them as *generalized* NOs.

Note that both $n_{\mathrm{min}}^{(i)}$ and $\epsilon_{\mathrm{min}}^{(i)}$ generally depend on the iteration step and can be chosen to be of different sizes. However, as we have indicated before, it remains to be clarified how to choose best the thresholds $n_{\mathrm{min}}^{(i)}$ so that no important states are removed from the basis set at inopportune times. $\epsilon_{\mathrm{min}}^{(i)}$, on the other hand, allows us to fix the number of configurations in the many-particle basis. For small configuration spaces it is feasible to choose $\epsilon_{\mathrm{min}}^{(i)}$ very small, i.e. to consider large many-particle configuration spaces. For higher iteration steps the single-particle basis sets get larger accompanied by an increasing number of configurations. Therefore, one typically has to increase $\epsilon_{\mathrm{min}}^{(i)}$ in order to avoid excessive computational costs.

Recall that so far we have made no distinction between protons and neutrons. If we distinguished between them, then each sub-set of identical κ would split into two, one for protons and the other for neutrons. Consequently, there would then be twice as many sub-sets in total, requiring twice as many iteration steps to determine the fully optimized single-particle basis set.

5.3 Conclusion

In conclusion, we have proposed a novel approach to find an optimized single-particle basis set for the nuclear many-body problem starting from a basis of HO eigenstates. The main difference of this method over the existing NO approach is that the optimization is performed iteratively, i.e., sub-sets of the basis are optimized separately. Here, the (minimum) size of each sub-set is determined by symmetries required of the single-particle states, i.e., parity, total angular momentum and isospin conservation.

One starts by including only a sub-set of states that coincide in their quantum number κ and then transforms these states to NOs using the eigenvectors of the corresponding density matrix. Subsequently, one extends the optimized single-particle basis by a set of states with identical κ (different from the previous one) and rotates as before all orbitals contained in this basis set to their NO representation. This process is reiterated until all possible states are included and finally optimized. Due to the similarity to ordinary NOs, we refer to the fully optimized states as *generalized* NOs.

The key advantage of this method is that in all iteration steps except the last one, we consider (pre-optimized) sub-spaces of smaller size than the full space considered in the classical NO approach. The gain here is that by pre-optimizing

parts of the basis before adding further states, the diagonalization of the resulting Hamiltonian in each iteration step is simplified compared to the situation without any optimization. Thus it is possible to start from much larger single-particle basis sets than currently tractable, i.e. to choose bigger values of $e_{\max}$ at the very beginning, as well as to manage larger configuration spaces on the many-particle level.

Moreover, our method allows to dynamically eliminate, i.e. in each iteration step separately, (unimportant) states with very low occupations. This enables us to effectively capture the impact of very high-lying HO states while at the same time keeping the size of the single-particle space small and the computational costs low.

In order to extract physical observables from theoretical calculations and to compare them to experimental results, it is crucial to achieve full convergence as well as to minimize the dependence of physical observables on the basis set parameters. Using ordinary NOs, it was shown on the example of ^{16}O that the frequency dependence of the ground state energy and the charge radius practically vanishes, while at the same time the convergence behavior improves substantially with respect to the HO or HF basis [112, 115]. However, for heavier nuclei such as ^{78}Ni, this frequency dependence cannot be fully eliminated [112].

This problem can be addressed by starting from single-particle wave functions that reflect the true states better than is currently done. Our introduced *generalized* NOs seem to be ideally suited for this purpose for the reasons given above. It is to be expected that if the *generalized* NOs are chosen as a single-particle basis, the dependence of the observables on the oscillator frequency could be further reduced or, at best, even eliminated. This could enable one to extend *ab initio* calculations to heavier nuclei than currently feasible.

6 Interference between Nonresonant and Resonant Inelastic X-Ray Scattering: The example of NiO

Transition-metal compounds are of great significance in the search for new, technologically highly-relevant quantum materials with open d-shells, as they show many fascinating properties like giant magnetoresistance or high temperature superconductivity [126, 127]. All of these properties are closely related to the underlying electronic structure, in particular to the orbital degrees of freedom. Therefore, a detailed knowledge of the so-called $d - d$ excitations, i.e. on-site transitions between crystal field split d-states, is crucial, as they provide material specific information about the local symmetry of d-ions in a crystal. However, the precise determination of the corresponding spectra is quite challenging, since $d - d$ excitations involve dipole-forbidden transitions which in turn are difficult to access experimentally [128].

In recent years, two spectroscopic techniques, the Resonant Inelastic X-ray Scattering (RIXS) and the Nonresonant Inelastic X-ray Scattering (NIXS), have proven among others useful for their identification [128–133]. In typical NIXS (as well as RIXS) experiments the conditions are set such that the respective other process is suppressed. For instance, in NIXS the incident photon energy is typically chosen several hundred electron volt away from an atomic resonance [129–131] in order to minimize the resonant contribution of RIXS to the cross section. This implies, that interference between NIXS and RIXS is assumed to be negligible in the explanation of the measured spectrum.

However, almost a decade ago, Sun et al. [134] observed in their inelastic x-ray study on the O_2 molecule a pronounced angular anisotropy in the measured intensity, which could be attributed to the interference of NIXS and RIXS. Furthermore, the authors indicate the importance of the interference term for the interpretation of x-ray scattering spectra in general [134]. Indeed, there is also experimental evidence for the case of Nickel oxide, which may indicate interference of NIXS and RIXS [135]. Until today, a theoretical investigation of the NIXS-RIXS

interference term particularly in the context of $d-d$ excitations is missing.

In the remainder of this chapter we want to investigate the interference of RIXS and NIXS in more detail using the textbook example of Nickel oxide (NiO). For this purpose, we begin in section 6.1 with an introduction to Inelastic X-ray Scattering (IXS), a spectroscopic technique capable of probing the electronic structure of materials. IXS comprises NIXS and RIXS, which are afterwards introduced in the sections 6.1.1 and 6.1.2, respectively. There we review the corresponding cross sections and explain how $d-d$ excitations are induced. In section 6.2, we then focus on the NIXS-RIXS interference term and analyze besides the polarization dependence predicted by Sun et. al [134], also the energy dependence, under the assumption of a typical experimental scattering geometry.

6.1 Inelastic X-ray Scattering (IXS)

Inelastic X-ray Scattering (IXS) is a powerful experimental tool to investigate the correlated motion of electrons in atoms, molecules or solids. The basic idea of every x-ray scattering experiment is to scatter photons off matter, leaving behind the system in an excited state [100]. By measuring the change in energy, momentum (and polarization) of the scattered photons information on the excitations can be extracted. IXS is mediated by the light-matter interaction which typically can be treated non-relativistically, as the photon energies ($\sim$ 10 keV) used in inelastic scattering experiments are well below the electron rest mass ($m_e = 511$ keV) such that relativistic effects can be neglected. In the Coulomb gauge ($\nabla \cdot \mathbf{A} = 0$) the non-relativistic light-matter interaction Hamiltonian is given by [100]

$$H_{\text{int}} = \sum_{n=1}^{N} \left(\frac{e}{m_e} \mathbf{p}_n \cdot \mathbf{A}(\mathbf{r}_n, \mathbf{k}) + \frac{e^2}{2m_e} \mathbf{A}^2(\mathbf{r}_n, \mathbf{k}) \right) \tag{6.1}$$

where we employ natural units ($c = \hbar = \epsilon_0 = 1$). Here $\mathbf{r}_n$ and $\mathbf{p}_n$ are the position and momentum of the n-th electron and $\mathbf{A}(\mathbf{r}_n, \mathbf{k})$ denotes the vector potential with wave vector $\mathbf{k}$. In the following we will omit the index n and implicitly assume a summation over all N electrons.

The vector potential $\mathbf{A}$ is linear in the photon annihilation and creation operators. Therefore, the $\mathbf{p} \cdot \mathbf{A}$ term leads to inelastic x-ray scattering in second-order perturbation theory which dominates close to an absorption edge. The $\mathbf{A}^2$ term, on the other hand, corresponds to the first-order contribution and is the leading term far away from a resonance [100].

The quantity of interest in IXS experiments is the double differential cross section (DDCS) which describes the intensity of scattered photons measured within the energy range $\mathrm{d}\omega^0_{\mathrm{out}}$ and solid angle $\mathrm{d}\Omega$ [100]

$$\frac{\mathrm{d}^2\sigma}{\mathrm{d}\Omega \mathrm{d}\omega^0_{\mathrm{out}}} = r_0^2 \left(\frac{\omega^0_{\mathrm{out}}}{\omega^0_{\mathrm{in}}}\right) \sum_f \Bigg| \langle f|e^{i\mathbf{q}\cdot\mathbf{r}}|i\rangle (\boldsymbol{\epsilon}^*_{\mathrm{out}} \cdot \boldsymbol{\epsilon}_{\mathrm{in}}) + \frac{1}{m_e} \sum_n \frac{\langle f|\boldsymbol{\epsilon}^*_{\mathrm{out}} \cdot \mathbf{p}|n\rangle \langle n|\boldsymbol{\epsilon}_{\mathrm{in}} \cdot \mathbf{p}|i\rangle}{\omega^0_{\mathrm{in}} - (E^0_n - E^0_i) + \mathrm{i}\Gamma/2} \Bigg|^2 \delta(E^0_i - E^0_f + \omega) \tag{6.2}$$

where $r_0 = \frac{e^2}{m_e}$ denotes the classical electron radius. $|i\rangle$, $|f\rangle$ and $|n\rangle$ are the initial, final and intermediate states with corresponding energies E^0_i, E^0_f and E^0_n. $\mathbf{k}_{\mathrm{in}}$, ω^0_{in} and $\boldsymbol{\epsilon}_{\mathrm{in}}$ are the wave vector, energy and polarization of the incoming, and $\mathbf{k}_{\mathrm{out}}$, ω^0_{out} and $\boldsymbol{\epsilon}_{\mathrm{out}}$ of the outgoing photons. The scattering vector and the energy loss are defined by $\mathbf{q} = \mathbf{k}_{\mathrm{in}} - \mathbf{k}_{\mathrm{out}}$ and $\omega = \omega^0_{\mathrm{in}} - \omega^0_{\mathrm{out}}$, respectively. Γ is the lifetime broadening and will be taken from experiment.

In order to calculate the DDCS (6.2) for NiO the first step is to set up the Hamiltonian and to determine all relevant eigenstates. The Hamiltonian describing NiO is similar to the one we used to describe electron capture spectra, with the difference that we now consider a crystal and not a single atom. The spherical symmetry in NiO is broken due to the six O^{2-}-ions which surround the Ni^{2+}-ions octahedrally. To mimic the local symmetry of the Ni^{2+}-ions, we approximate the solid by a single Ni^{2+}-ion and add an effective crystal field potential H_{CF} to the Hamiltonian $H = H_{\mathrm{D}} + H_{\mathrm{C}} + H_{\mathrm{CF}}$ where H_D and H_C represent Dirac's Hamiltonian and Coulomb interaction, respectively. In an octahedral crystal field, the ten-fold degenerate $3d$ states split into a six-fold degenerate t_{2g} and a four-fold degenerate e_g irreducible representation. The e_g orbitals (d_{z^2} and $d_{x^2-y^2}$) point towards the oxygen ions, whereas the lobes of the t_{2g} orbitals (d_{xy}, d_{xz} and d_{yz}) point in between the oxygen. Hence, the electrons in the e_g orbitals experience a stronger Coulomb repulsion than electrons in the t_{2g} orbitals and are therefore higher in energy. The energy splitting between e_g and t_{2g} is referred to as the crystal field splitting Δ_{CF} and in NiO amounts to $\Delta_{\mathrm{CF}} \approx 1.1$ eV [126].

6.1.1 Nonresonant Inelastic X-ray Scattering (NIXS)

The first term in (6.2) is based on the $\mathbf{A}^2$ term of the interaction and describes the Nonresonant Inelastic X-ray scattering (NIXS). The basic idea of NIXS is to

transfer high momenta in the scattering process such that higher-order multipoles beyond the dipole become relevant. This is typically achieved in the hard x-ray regime ($\sim$ 10 keV) where the photon energy exceeds the atomic transition energies [136]. While at low momentum transfer the direction of $\mathbf{q}$ provides equivalent information as the polarization vector in x-ray absorption spectroscopy (XAS), at high momentum transfer NIXS can resolve more complicated features not accessible in XAS. This property is for example utilized in the recently developed experimental method *s*-NIXS which allows to make a direct image of the active orbitals in novel quantum materials [137]. Furthermore, NIXS has been used to study the ground-state symmetry in strongly correlated materials [138] or to observe $d-d$ excitations in transition metal oxides [128–131].

The NIXS spectrum is determined by the so-called dynamic structure factor

$$S(\mathbf{q},\omega) = \sum_f \left|\langle f|e^{i\mathbf{q}\cdot\mathbf{r}}|i\rangle\right|^2 \delta(E_i^0 - E_f^0 + \omega) \tag{6.3}$$

which contains only the material-specific part of the DDCS (6.2). Note than one can express the dynamic structure factor in terms of a linear response function as shown in [128].

In order to directly obtain the transitions in terms of the different allowed multipole excitations, it is convenient to expand the exponential in terms of renormalized spherical harmonics $C_m^{(k)}(\hat{r}) = \sqrt{4\pi/(2k+1)}Y_m^{(k)}(\hat{r})$

$$e^{i\mathbf{q}\cdot\mathbf{r}} = \sum_{k=0}^{\infty}\sum_{m=-k}^{k} i^k(2k+1)j_k(qr)C_m^{(k)*}(\hat{q})C_m^{(k)}(\hat{r}) \tag{6.4}$$

where $j_k(qr)$ is a k-th order spherical Bessel function. Then, the matrix elements can be written as [128]

$$\begin{aligned}\langle f|e^{i\mathbf{q}\cdot\mathbf{r}}|i\rangle = \sum_{k=0}^{\infty}\sum_{m=-k}^{k} & i^k(2k+1)\langle R_{n_f l_f}|j_k(qr)|R_{n_i l_i}\rangle \\ & \times C_m^{(k)*}(\hat{q})\langle Y_{l_f m_f}|C_m^{(k)}(\hat{r})|Y_{l_i m_i}\rangle\end{aligned} \tag{6.5}$$

where we have assumed initial and final state wave functions of the form $\psi(\mathbf{r}) = R_{nl}(r)Y_{lm}(\theta,\phi)$. The sum over multipole moments k, which contribute to a transition from $l_i \to l_f$ are restricted by the triangle condition of the Clebsch-Gordan coefficients $|l_i - l_f| \leqslant k \leqslant l_i + l_f$ and by parity $l_i + l_f + k =$ even. For $d-d$ transitions this implies $k = 0, 2, 4$. Due to conservation of angular momentum, the

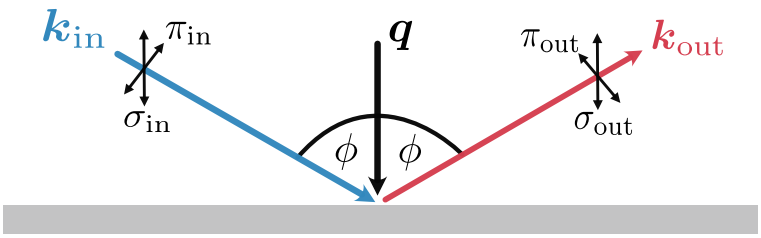

Figure 6.1: Sketch of the scattering geometry. The momentum transfer $\mathbf{q} = \mathbf{k}_{\mathrm{in}} - \mathbf{k}_{\mathrm{out}}$ is parallel to the [110]-direction.

magnetic quantum number m satisfies the condition $m = m_f - m_i$. The excitations in NIXS are spin-conserving, i.e. $\Delta S = 0$.

The NIXS scattering amplitude (6.5) depends on both, the absolute values of the scattering vector $|\mathbf{q}| = q$ and on its direction $\hat{q}$ with respect to the crystal axis. The momentum transfer q emerges in the argument of the spherical Bessel function $j_k(qr)$. For the scattering geometry (see Fig. 6.1) we assume for all our calculations q is related to the incident photon energy and the angle $\phi = \sphericalangle(\mathbf{k}_{\mathrm{in/out}}, \mathbf{q})$ by $q = 2\cos(\phi)\omega_{\mathrm{in}}^0$. As the momentum transfer increases, first the quadrupole ($k = 2$) and then the hexadecapole ($k = 4$) transitions become maximal [128]. Monopole ($k = 0$) excitations, on the other hand, peak at zero photon energy, but only play a role for the elastic scattering which is irrelevant for our purpose. Hence, the size of q determines the spectral weight of the allowed multipoles which offers an opportunity to optimize the experimentally measured intensity.

The directional dependence on $\mathbf{q}$, on the other hand, is encoded in the angular part of the matrix element $\sum_{m=-k}^{k} C_m^{(k)*}(\hat{q})\langle Y_{l_f m_f}|C_m^{(k)}(\hat{r})|Y_{l_i m_i}\rangle$. All multipoles except the monopole ($k = 0$) show a directional dependence on $\mathbf{q}$. Since the spherical harmonics are sensitive to the z-component of the orbital angular momentum of the initial and final states, the orientation of $\mathbf{q}$ with respect to the sample determines which valence states are probed [136].

6.1.2 Resonant Inelastic Scattering (RIXS) at the K-edge

Resonant inelastic X-ray Scattering (RIXS) originates from the $\mathbf{p} \cdot \mathbf{A}$ term and is the second order process of the DDCS (6.2). A core electron is first excited into the valence shell and then decays by refilling the core hole and emitting a photon. By analyzing the change in energy, momentum and polarization of the scat-

tered photons one can retrieve information about the elementary excitations of the system under consideration. RIXS is a versatile technique, capable of probing a broad class of low-energy excitations in molecules, atoms or solids. For example, it has been successfully applied to probe elementary excitations like magnons [139], charge-transfer [140] or phonons [141]. In particular, also the $d-d$ excitations in transition metal oxides have been observed by RIXS [132, 133]. Apart from its versatility, RIXS has numerous advantages compared to alternative methods like for instance neutron scattering, which made RIXS a popular and widespread technique. For example, RIXS is bulk sensitive, polarization dependent and can be utilized to probe thin films or surfaces [142]. A more detailed discussion can be found in the review [142].

The RIXS spectrum is determined by the the second term of the DDCS (6.2)

$$\frac{\mathrm{d}^2\sigma}{\mathrm{d}\Omega\mathrm{d}\omega^0_{\mathrm{out}}} \propto \sum_f \left| \sum_n \frac{\langle f|\mathcal{D}'^{\dagger}|n\rangle\langle n|\mathcal{D}|i\rangle}{\omega^0_{\mathrm{in}} - (E^0_n - E^0_i) + \mathrm{i}\Gamma/2} \right|^2 \delta(E^0_i - E^0_f + \omega) \tag{6.6}$$

where $\mathcal{D} = \boldsymbol{\epsilon}_{\mathrm{in}} \cdot \mathbf{p}$ and $\mathcal{D}' = \boldsymbol{\epsilon}_{\mathrm{out}} \cdot \mathbf{p}$ are the dipole operators for the absorption and emission processes, respectively. Alternatively, one can rewrite the RIXS cross section in terms of a Green's function similar to the dynamic structure factor. However, since RIXS is a second-order process, this requires a higher-order Green's function.

In the following, we will consider RIXS at the K-edge, i.e. the excitation of a $1s$ core electron. Since the transition into the $3d$ shell is dipole-forbidden and therefore weak, we focus on the much stronger dipole-allowed excitation into the $4p$ shell above the Fermi edge. At the K-edge, the angular momentum of the excited $4p$ electron is directly related to the polarization of the incident photons. More precisely, the dipole operator takes the form $\mathcal{D} \sim \sum_{q\sigma} \epsilon_q p^{\dagger}_{q\sigma} s_\sigma$ where $\epsilon_q = C^{(1)}_q(\hat{\epsilon})$ are the components of the polarization vector $\boldsymbol{\epsilon}$; $p^{\dagger}_{q\sigma}$ creates an electron in $4p$ with spin component σ and projection of of orbital momentum q onto the z-axis, whereas s_σ annihilates a $1s$ electron [133]. Note that we have neglected the finite $4p$ band width and instead assume a constant, momentum independent energy of the $4p$ shell. In the intermediate state, the $1s$ core hole, the $4p$ and $3d$ shell interact. $d-d$ excitations describe the transitions between different d-orbitals and involve a change of orbital angular momentum. Since the $1s$ core hole cannot transfer angular momentum to the valence, the $d-d$ excitations are caused by the higher-order terms of the $3d-4p$ Coulomb repulsion ($\sim$ 0.1 eV). The much

stronger $1s - 3d$ Coulomb interaction ($\sim 6 - 8$ eV), on the other hand, leads to charge-transfer excitations which are observed at higher excitation energies [133]. Since the excitations are induced by the $3d - 4p$ Coulomb repulsion and not directly by the photon, this process is referred to as indirect RIXS.

In order to better understand how the $d - d$ excitations are induced in the indirect RIXS process, let us now take a look at an example. Assume the $1s$ electron to be excited from the ground state into the $4p$ state with orbital angular momentum $m_{4p} = 1$. An electron in one of the t_{2g} orbitals, for example the one with $m_{3d} = -2$, then interacts with the $4p$ electron, thereby exchanging an orbital angular momentum of $+2$ such that the two electrons are scattered into the states with $m'_{3d} = 0$ and $m'_{4p} = -1$. The dipole operator responsible for the de-excitation process annihilates the $4p$ electron and refills the core-hole. Finally, the atom ends up in a state where one of the t_{2g} electrons has been excited into an e_g which corresponds to a $d - d$ excitation.

Due to the absent spin-orbit coupling at the K-edge, only the exchange interaction of the $1s$ with the valence shell can lead to a spin-flip of the core hole. This term, however, is relatively small such that the spin is unlikely to change. Consequently, also the spin of the $4p$ electron which refills the core hole remains the same and one mainly probes spin-conserving excitations. Furthermore, it is important to realize that the angular momentum transfer from $4p$ to $3d$ is necessarily connected with a polarization change of the photon.

In the following, we focus on incident photon energies far away from a resonance which is satisfied if the photon energy exceeds the excitation energy of all the intermediate states $|n\rangle$, i.e. we assume $\left|\frac{E_n}{\omega_{\text{in}}+\text{i}\Gamma/2}\right| \ll 1 \; \forall \; |n\rangle$. As a first step we rewrite the scattering amplitude and measure all energies from the resonance energy ω_{res} which in the underlying case corresponds to the $1s - 4p$ atomic transition energy. In that case the RIXS scattering amplitude takes the form

$$\mathcal{F}_{fi} = \sum_n \frac{\langle f|\mathcal{D}'^{\dagger}|n\rangle\langle n|\mathcal{D}|i\rangle}{\omega_{\text{in}} - E_n + \text{i}\Gamma/2} \tag{6.7}$$

where $\omega_{\text{in}} = \omega_{\text{in}}^0 - \omega_{\text{res}}$ denotes the energy of the incoming x-rays and $E_n = E_n^0 - \omega_{\text{res}}$ the energy of the intermediate state $|n\rangle$ both measured from ω_{res}. The initial state energy has been set to zero $E_i \equiv 0$.

Although we evaluate the general expression of the RIXS amplitude (6.7) in all our calculations, we now expand the scattering amplitude in terms of a power

series in order to provide a better understanding of the relevant terms. Far away from the resonance, (6.7) can be written as [143]

$$\mathcal{F}_{fi} = \frac{1}{\omega_{\text{in}} + \text{i}\Gamma/2} \sum_{m=0}^{\infty} F_m \tag{6.8}$$

with matrix elements

$$\begin{aligned} F_m &= \sum_n \left(\frac{E_n}{\omega_{\text{in}} + \text{i}\Gamma/2} \right)^m \langle f|\mathcal{D}'^{\dagger}|n\rangle\langle n|\mathcal{D}|i\rangle \\ &= \left(\frac{1}{\omega_{\text{in}} + \text{i}\Gamma/2} \right)^m \langle f|\mathcal{D}'^{\dagger} H^m \mathcal{D}|i\rangle. \end{aligned} \tag{6.9}$$

In the last line the sum over intermediate states $|n\rangle$ with energy E_n has been replaced by H^m, as these are eigenstates of the Hamiltonian.

We can further make the following approximations: The first term in the expansion ($m = 0$) does not involve the Hamiltonian H. Hence, the state after the dipole-allowed excitation, $\mathcal{D}|i\rangle$, remains unaltered and consequently the $m = 0$ term only contributes to elastic scattering. Since we are interested in $d - d$ excitations which are caused by IXS, we can omit the $m = 0$ term. In addition, we ignore all terms in the series with $m > 1$, because for large ω_{in} these are strongly suppressed with respect to $m = 1$. Finally, the leading-order scattering amplitude for incident photon energies far away from a resonance is given by

$$\mathcal{F}_{fi}^{(1)} = \left(\frac{1}{\omega_{\text{in}} + \text{i}\Gamma/2} \right)^2 \langle f|\mathcal{D}'^{\dagger} H \mathcal{D}|i\rangle. \tag{6.10}$$

In this case RIXS is proportional to a linear response function similar to NIXS. Compared to the general RIXS amplitude (6.7), (6.10) has the advantage that it is independent of the complicated intermediate states $|n\rangle$ which in particular is useful for systems with a large number of atoms where the calculation of the intermediate states might become challenging [143]. However, despite a finite $4p$ bandwidth of the order of one Rydberg [144] (which is neglected here) and the fact that only the $m = 1$ term is included in the expansion, the leading-order scattering amplitude (6.10) provides an accurate description of RIXS starting from approximately 100 eV away from the resonance.

Since the polarization and momentum vectors are rank-1 spherical tensor operators, it is convenient to separate polarization-dependent and independent parts by re-coupling the spherical tensor operators [142]

$$\mathcal{F}_{fi}^{(1)} \sim \left(\frac{1}{\omega_{\text{in}} + \text{i}\Gamma/2} \right)^2 \sum_{K=0}^{2} \left\{ \boldsymbol{\epsilon}_{\text{out}}^* \otimes \boldsymbol{\epsilon}_{\text{in}} \right\}^{(K)} \cdot \langle f| \left\{ \mathbf{r}^{\dagger} \otimes H\mathbf{r} \right\}^{(K)} |i\rangle \tag{6.11}$$

where the momentum is linked to the position by $\mathbf{p} = \frac{m}{\mathrm{i}}[\mathbf{r}, H]$. The scalar product of the two spherical tensor operators $\mathbf{A}^{(K)} \equiv \left\{\boldsymbol{\epsilon}^*_{\mathrm{out}} \otimes \boldsymbol{\epsilon}_{\mathrm{in}}\right\}^{(K)}$ and $\mathbf{B}^{(K)} \equiv \left\{\mathbf{r}^\dagger \otimes H\mathbf{r}\right\}^{(K)}$ can explicitly be written as [47]

$$\mathbf{A}^{(K)} \cdot \mathbf{B}^{(K)} = \sum_{Q=-K}^{K} (-1)^Q A^{(K)}_{-Q} B^{(K)}_{Q} \tag{6.12}$$

with components $A^{(K)}_{-Q}$ and $B^{(K)}_{Q}$. Since we consider excitations between two states with identical parity, the contribution from $K = 1$ vanishes due to conservation of parity. Although the $K = 0$ term is non-zero, it only contributes to the elastic scattering. Therefore, the amplitude is determined by $K = 2$ and reads

$$\mathcal{F}^{(1)}_{fi} = \left(\frac{1}{\omega_{\mathrm{in}} + \mathrm{i}\Gamma/2}\right)^2 \sum_{Q=-2}^{2} (-1)^Q \mathbf{A}^{(2)}_{-Q} \mathbf{B}^{(2)}_{Q}. \tag{6.13}$$

In contrast to NIXS where the polarization dependence enters as a geometric prefactor, in RIXS it directly influences the scattering process by weighting the fundamental amplitudes $\mathbf{B}^{(2)}$.

6.2 NIXS-RIXS interference

Although NIXS and RIXS can be regarded as two complementary experimental techniques, both can be used to probe $d - d$ excitations. Consequently, most of the final states $|f\rangle$ are reached in NIXS and RIXS such that there is - apart from the pure NIXS and RIXS parts - also a non-vanishing NIXS-RIXS interference which contributes to the DDCS (6.2). This term, however, is typically neglected in theoretical calculations. Here we want to systematically analyze the energy- and angular dependence of the NIXS-RIXS interference and to show its impact on the $d - d$ excitations in NiO.

In order to specify the relative strength of NIXS and RIXS as a function of the incident photon energy, we now calculate the transition strength which we define as the radial part of the cross section. In NIXS the transition strength can be read off directly from the scattering amplitude (6.5)

$$f_N = \left|(2k+1)\langle R_{3\mathrm{d}}(r)|j_k(2\cos(\phi)\omega^0_{\mathrm{in}} r)|R_{3\mathrm{d}}(r)\rangle\right|^2 \tag{6.14}$$

and depends on the multipole order k and on ϕ. In RIXS, on the other hand, the transition strength is determined by the product of two dipole matrix elements

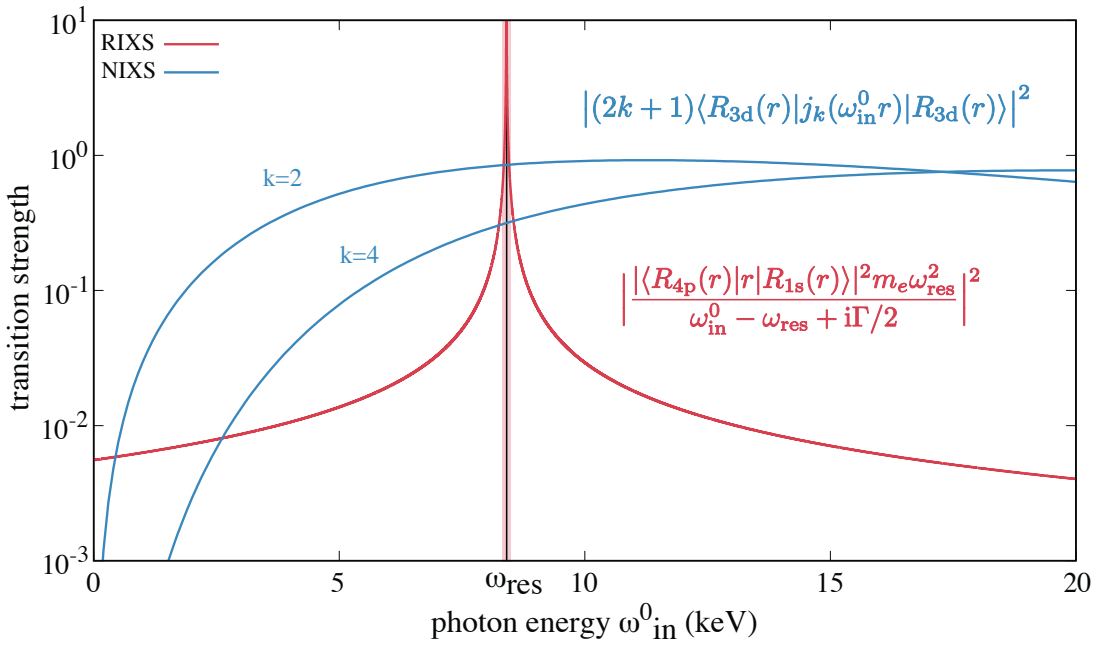

Figure 6.2: Transition strength for NIXS (blue) and RIXS (red) as a function of the incident photon energy ω^0_{in} at an angle of $\phi = \sphericalangle(\mathbf{k}_{\text{in/out}}, \mathbf{q}) = 60°$. The lifetime broadening Γ of the Ni $1s$ core hole is set to $\Gamma = 1.44$ eV and has been taken from experiment [145]. ω_{res} corresponds to the energy matching the $1s - 4p$ atomic transition which in NiO amounts to $\omega_{\text{res}} \approx 8.4$ keV. The red hatched area ± 100 eV around the resonance indicates where the leading-order RIXS amplitude (6.10) loses validity.

times the resonant enhancement as can be inferred from (6.6). Replacing the momentum operator by $\mathbf{p} = \frac{m}{\mathrm{i}}[\mathbf{r}, H]$, the dipole operator is proportional to the scalar product of polarization and position vector

$$\boldsymbol{\epsilon} \cdot \langle n'l'm'|\mathbf{r}|nlm\rangle = \sum_{q=-1}^{1} (-1)^q \epsilon_{-q} \langle R_{n'l'}(r)|r|R_{nl}(r)\rangle \langle l'm'|C^{(1)}_q(\hat{r})|lm\rangle \tag{6.15}$$

with single-particle orbitals $|nlm\rangle = R_{nl}(r)|lm\rangle$.

Here we focus on the $1s - 4p$ edge, i.e. the dipole operators couple the $1s$ and $4p$ orbital, such that the relevant radial integral is $\langle R_{4p}(r)|r|R_{1s}(r)\rangle$. The Hamiltonian originating from the commutator $\mathbf{p} = \frac{m}{\mathrm{i}}[\mathbf{r}, H]$ enters twice and is evaluated between the initial/final state and the intermediate state with a core hole in the $1s$ shell. Assuming that $\omega_{\text{res}} \approx |E_i - E_n|$ and $E_i \approx E_f$ leads to an

additional factor of ω_{res}^2. Finally, the transition strength in RIXS takes the form

$$f_R = \left| \frac{|\langle R_{4\text{p}}(r)|r|R_{1\text{s}}(r)\rangle|^2 m_e \omega_{\text{res}}^2}{\omega_{\text{in}}^0 - \omega_{\text{res}} + \text{i}\Gamma/2} \right|^2 . \tag{6.16}$$

Fig. 6.2 displays the transition strength in RIXS and NIXS as a function of the incident photon energy ω_{in}^0. Close to a resonance, RIXS it is strongly enhanced exceeding NIXS. At the resonance the enhancement is $(\omega_{\text{res}}/\Gamma)^2$ and for transition metals amounts to $\sim 10^6$ [143]. Off-resonance RIXS rapidly decays until at about 100 eV away from the resonance. First the quadrupole ($k = 2$) and finally, at higher photon energies, the hexadecapole ($k = 4$) term in NIXS take over. The magnitude of the interference is proportional to the product of the NIXS and RIXS transition strength. Although this leads to a big interference in the vicinity of a resonance, it is small compared to the strongly enhanced RIXS which will dominate the cross section at these energies. Thus, the energy window, where measurable interference effects can be expected, ranges from hundred eV up to a few keV away from the resonance. Interestingly, typical NIXS experiments on transition-metal oxides, like for example NiO [129, 130] and CuO [131], are performed at photon energies $\sim 0.8 - 1.5$ keV away from the resonance and fall in the aforementioned energy window. Hence, interference effects are expected to become relevant and should be included in the calculations in order to accurately describe the measured spectra.

Energy dependence

While the transition strength determines the magnitude, the type of the interference, i.e. constructive or destructive, depends on the relative phase between the NIXS and RIXS scattering amplitudes. One possibility to change the relative phase and thereby the interference is to tune the incident photon energy across a resonance which in the underlying case corresponds to the $1s - 4p$ atomic transition energy at $\omega_{\text{res}} \approx 8.4$ keV.

Fig. 6.3 shows the RIXS+NIXS spectrum of NiO including the interference for $\pi_{\text{in}} - \pi_{\text{out}}$ at an angle of $\phi = \sphericalangle(\mathbf{k}_{\text{in/out}}, \mathbf{q}) = 60^\circ$ and $\sigma_{\text{in}} - \sigma_{\text{out}}$ polarization for different photon energies from 5 keV (purple) to 9 keV (red). The bottom row displays the individual RIXS, NIXS and interference contributions. In all calculations the momentum transfer points in the [110]-direction. For cross-polarization $\sigma_{\text{in}} - \pi_{\text{out}}$ and $\pi_{\text{in}} - \sigma_{\text{out}}$ NIXS and consequently the interference vanishes, be-

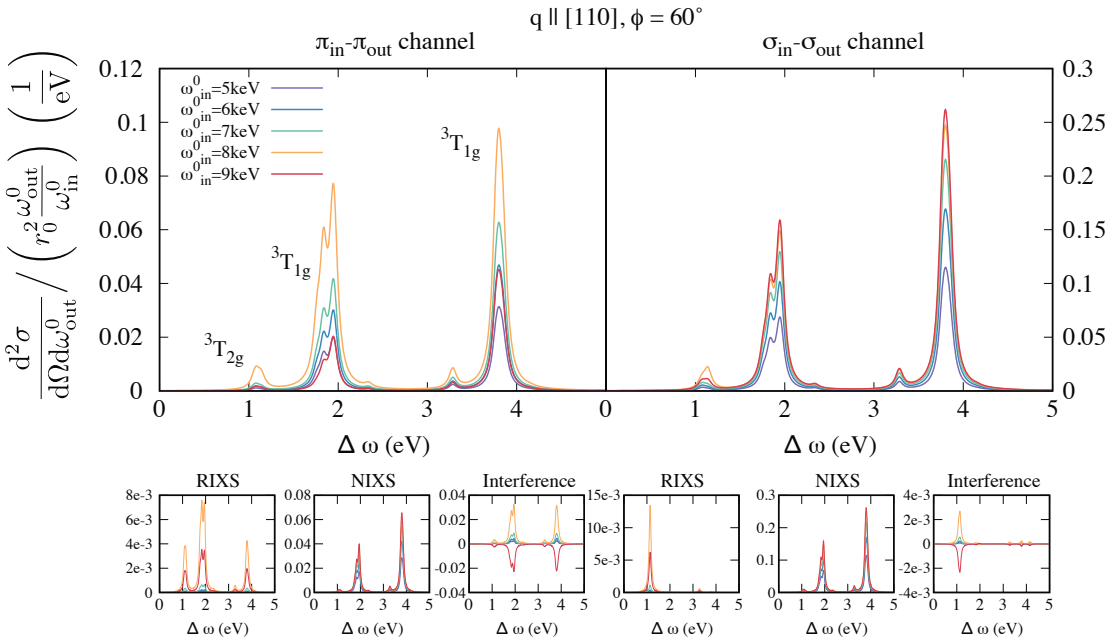

Figure 6.3: The top row shows the NIXS+RIXS spectra including the interference for $\pi_{\text{in}} - \pi_{\text{out}}$ polarization at $\phi = \sphericalangle(\mathbf{k}_{\text{in/out}}, \mathbf{q}) = 60°$ and $\sigma_{\text{in}} - \sigma_{\text{out}}$ polarization (see Fig. 6.1) for different incident photon energies $\omega^0_{\text{in}} = 5 - 9$ keV. The bottom row displays the different parts (RIXS, NIXS and Interference) composing the full spectra on the top. The momentum transfer $\mathbf{q}$ is parallel to the [110]-direction.

cause the polarization vectors of the incident and scattered photons are by definition orthogonal to each other. Therefore, we can ignore these channels.

Both, the RIXS and NIXS spectrum shows three main peaks. The first peak at 1.1 eV has ${}^3T_{2g}$ symmetry and is quadrupole forbidden. However, hexadecapole transitions and higher-order effects lead to some small intensity. The second and third peak around 1.8 and 3.0 eV have ${}^3T_{1g}$ symmetry and can be reached from the ${}^3A_{2g}$ ground state with configuration $t_{2g}^6 e_g^2$ by quadrupole and hexadecapole transitions [128].

At first glance it might be surprising to observe three resonances instead of one, as a single photon can only excite one electron at time. We therefore want to explain the origin of the individual resonances in more detail:

The first peak is understandable on a mean-field level and corresponds to the excitation of one electron from the occupied t_{2g} into one of the empty e_g states at an excitation energy of roughly $\Delta_{\text{CF}} = 1.1$ eV. However, Coulomb repulsion splits the energy of the $t_{2g}^5 e_g^3$ configuration, because the t_{2g} (xy) electron interacts

more strongly with the e_g $(x^2 - y^2)$ than with an e_g (z^2) electron which leads to an additional peak at 3 eV. The second peak sits at roughly twice the energy of the crystal field splitting and corresponds to the double excitation from t_{2g} to e_g. This peak results from the Coulomb interaction between t_{2g} and e_g which mixes in configurations with two holes in t_{2g} and therefore is only understandable in a true many-body picture [40].

In both polarization channels the interference is constructive below the edge ($\omega_{\text{in}}^0 = 5 - 8$ keV) and destructive above ($\omega_{\text{in}}^0 = 9$ keV) which can be understood as follows: The sign of the RIXS amplitude (6.7) is determined by $1/(\omega_{\text{in}} + \mathrm{i}\Gamma/2)$. Below the edge ($\omega_{\text{in}} < 0$), the real and imaginary part of $1/(\omega_{\text{in}} + \mathrm{i}\Gamma/2)$ are negative. If, however, the photon energy is tuned above the edge ($\omega_{\text{in}} > 0$), the real part turns positive while the imaginary part remains negative. Contrarily, in NIXS neither the sign of the real nor the imaginary part changes which could compensate the sign-flip in RIXS. Therefore, the relative phase between RIXS and NIXS differs below and above the edge, finally changing the character of the interference.

The magnitude of the interference shows a similar energy dependence as RIXS. It is maximal at 8 keV – the energy closest to the resonance – and rapidly decays when the photon energy moves away. Remarkably, for the ${}^3T_{1g}$ states in the $\pi_{\text{in}} - \pi_{\text{out}}$ channel, the spectral weight due to interference exceeds RIXS by almost one order of magnitude. Above 7 keV the interference is even of the same order as NIXS leading to prominent changes of the spectra. While in NIXS the intensity of all peaks increases from 5 to 9 keV, the sequence of the spectra changes when the RIXS and interference parts are included. Precisely, the spectrum at 9 keV drops below the one at 6 keV for the first and third excitation or even below the spectrum at 5 keV for the second peak. As RIXS adds more spectral weight to the spectrum at 9 keV than to all the other spectra below 8 keV, the strongly reduced intensity can only be explained by the interference.

In the $\sigma_{\text{in}} - \sigma_{\text{out}}$ channel, the excitations with ${}^3T_{1g}$ symmetry disappear in RIXS. Hence, also the interference vanishes and the spectra look similar to NIXS at these energies. The ${}^3T_{2g}$ peak, however, shows a high RIXS intensity and a non-vanishing interference. At 8 keV RIXS and the interference become maximal and are of similar magnitude. Since the interference is – like in the $\pi_{\text{in}} - \pi_{\text{out}}$ channel – constructive below the edge and destructive above, RIXS and interference both add spectral weight to the NIXS intensity leading to the pronounced peak at 1.1 eV.

Angular dependence

So far we have discussed the energy-dependence of the NIXS+RIXS spectrum at the fixed angle of $\phi = \sphericalangle(\mathbf{k}_{\text{in/out}}, \mathbf{q}) = 60°$. A second possibility to tune the NIXS-RIXS interference is by changing ϕ. Photons are characterized by transverse waves, i.e. their momentum and polarization vector are perpendicular to each other. Since the electric field of σ-polarized photons oscillates perpendicular to the scattering plane, their polarization vector is independent of ϕ and hence, no angular dependence of the interference is observed. In the $\pi_{\text{in}} - \pi_{\text{out}}$ channel, on the other hand, an angular dependence of the interference is expected, because here the polarization vectors depend on the orientation of $\mathbf{k}_{\text{in}}$ and therefore on ϕ. Two sets of polarization vectors for $\pi_{\text{in}} - \pi_{\text{out}}$ polarization are compatible with the scattering geometry shown in Fig. 6.1. In Cartesian coordinates they are given by

$$\boldsymbol{\epsilon}_{\text{in}} = \frac{1}{\sqrt{a^2+b^2}} \begin{pmatrix} a \\ b \\ 0 \end{pmatrix} \quad , \quad \boldsymbol{\epsilon}_{\text{out}} = \frac{1}{\sqrt{a^2+b^2}} \begin{pmatrix} b \\ a \\ 0 \end{pmatrix}$$

and

$$\boldsymbol{\epsilon}'_{\text{in}} = \frac{1}{\sqrt{a^2+b^2}} \begin{pmatrix} b \\ a \\ 0 \end{pmatrix} \quad , \quad \boldsymbol{\epsilon}'_{\text{out}} = \frac{1}{\sqrt{a^2+b^2}} \begin{pmatrix} a \\ b \\ 0 \end{pmatrix} \tag{6.17}$$

where $a = \sin(\phi) - \cos(\phi)$ and $b = \sin(\phi) + \cos(\phi)$. Note that the two sets of polarization vectors lead to the same spectrum.

Fig. 6.4 shows the angular dependence of the interference for $\pi_{\text{in}} - \pi_{\text{out}}$ polarization below ($\omega^0_{\text{in}} = 8$ keV) and above ($\omega^0_{\text{in}} = 9$ keV) the edge. Below the edge the interference is constructive for $\phi > 45°$ and destructive for $\phi < 45°$. Above the edge, the situation is reversed as a result of the energy-dependence of the interference discussed before.

To unscramble the origin of the observed angular dependence of the interference, we will in the following analyze the individual polarization dependence of NIXS and RIXS. In NIXS the polarization dependence is determined by the scalar product of the polarization vectors. Explicitly, we find for the two possible sets of polarization vectors $\boldsymbol{\epsilon}^*_{\text{out}} \cdot \boldsymbol{\epsilon}_{\text{in}} = \sin^2(\phi) - \cos^2(\phi)$, i.e. negative values for $\phi < 45°$ and positive for $\phi > 45°$. At an angle of $\phi = 45°$ the scalar product vanishes leading to vanishing NIXS and interference terms. While the sign-change of $\boldsymbol{\epsilon}^*_{\text{out}} \cdot \boldsymbol{\epsilon}_{\text{in}}$ induces a phase-change in NIXS, the sign in RIXS remains constant when ϕ crosses 45° which is closely connected to the change of orbital angular momen-

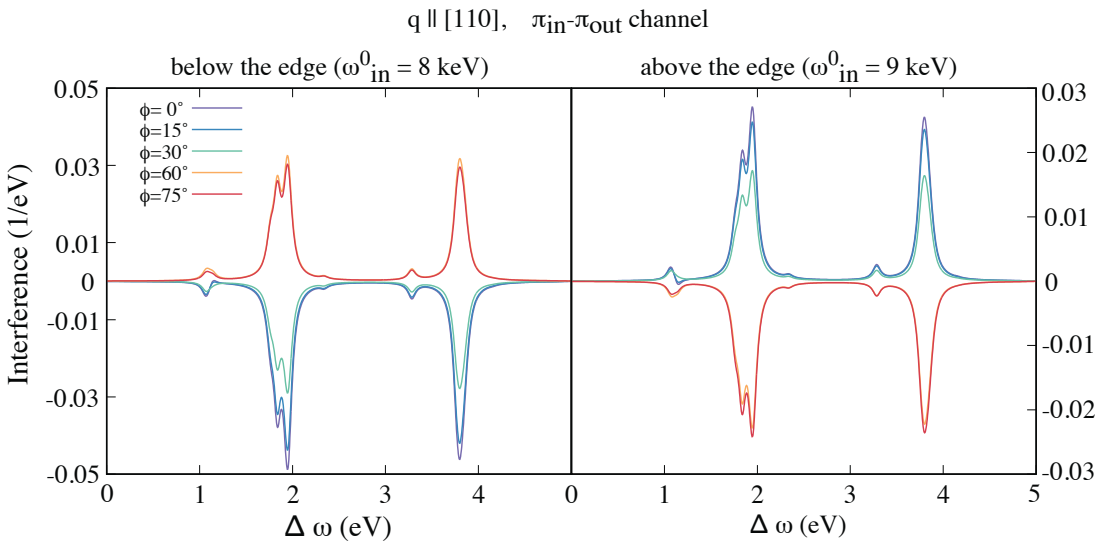

Figure 6.4: Angular dependence of the NIXS-RIXS interference below and above the $1s - 4p$ edge at an energy of $\omega_{\text{res}} \approx 8.4$ keV. The calculations are performed for $\pi_{\text{in}} - \pi_{\text{out}}$ polarization and the momentum transfer is parallel to the [110]-direction.

tum of the $4p$ electron in the intermediate state and to the particular scattering geometry. Recall the example discussed in section 6.1.2, where a $1s$ core electron is excited into the $4p$ orbital with angular momentum $m_{4p} = 1$, then scatters into $m_{4p} = -1$ and finally refills the core hole. As we have pointed out, the relevant components of the polarization vector in the excitation (ϵ_1) and de-excitation (ϵ_{-1}) steps necessarily need to be different in order to transfer angular momentum to the $3d$ states, thereby inducing $d - d$ excitations. By relating the spherical components $\epsilon_{\pm 1}$ to the Cartesian ones (6.17), $\epsilon_{\pm 1} = \mp(\epsilon_x \pm \mathrm{i}\epsilon_y)/\sqrt{2}$, the polarization dependence takes the form $\epsilon^*_{-1} \cdot \epsilon_1 = -(\mathrm{i}a + b)(a + \mathrm{i}b) = -\mathrm{i}$ and in particular is independent of ϕ. As a result, the different interference beyond $\phi = 45°$ can be attributed to the sign change of the NIXS amplitude, because only the NIXS flips sign. In alternative scattering geometries, however, where for example the angles $\sphericalangle(\mathbf{k}_{\text{in}}, \mathbf{q})$ and $\sphericalangle(\mathbf{k}_{\text{out}}, \mathbf{q})$ are not identical, the angular dependence of the polarization vectors is different and one might also observe sign-changes of the RIXS amplitude which could affect the interference.

6.3 Conclusion

In summary, we have calculated the NIXS spectrum for the textbook-example NiO including RIXS and interference contributions for incident photon energies from $\omega_{\text{in}}^0 = 5 - 9$ keV and a momentum transfer in the [110]-direction. The photon energies were chosen far away from the $1s - 4p$ resonance at $\omega_{\text{res}} \approx 8.4$ keV enabling us to expand the RIXS amplitude in terms of a power series. Since the cross-polarized channels vanish in NIXS, interference is possible for $\pi_{\text{in}} - \pi_{\text{out}}$ and $\sigma_{\text{in}} - \sigma_{\text{out}}$ polarization.

Our results reveal that even several hundred electron volts away from the $1s - 4p$ resonance, the interference can be of the same order as NIXS leading to prominent changes of the relative and absolute peak intensities. In particular, this becomes evident in the $\pi_{\text{in}} - \pi_{\text{out}}$ channel where all three peaks show non-vanishing interference. Furthermore, our study unscrambles the origin of the NIXS-RIXS interference and provides a systematic analysis of the angular and energy dependence. It turns out that whether one has constructive or destructive interference depends on the scattering geometry, i.e. on the angle $\phi = \sphericalangle(\mathbf{k}_{\text{in/out}}, \mathbf{q})$, but also on the incident photon energy relative to the resonance. The different interference across an edge can be assigned to a sign change of the real part in RIXS and is observed in both polarization channels. The angular dependence is due to the sign change of the polarization in NIXS and only occurs in the $\pi_{\text{in}} - \pi_{\text{out}}$ channel.

In conclusion, our results indicate that the inclusion of the interference term in future calculations will reduce the discrepancy between theory and experiment and provide a better understanding of the $d - d$ excitations in transition metal compounds. A comparison of theory and future experiments will make it possible to test our predictions. In particular, it will be interesting to see if our theoretical predictions can explain the observed features in the NiO spectrum [135] which might originate from a NIXS-RIXS interference.

7 Summary & Outlook

Within this thesis, we provided a theoretical description of nuclear decay by electron capture. We discussed the influence of nuclear degrees of freedom and the coupling to the continuous spectrum of the electromagnetic field on the decay rate.

In chapter 2, we used the theory originally developed by Brass and Haverkort for the case of ^{163}Ho [9] to calculate the electron capture spectra of various isotopes such as ^{55}Fe, ^{65}Zn, ^{71}Ge, ^{118}Te, ^{131}Cs, ^{140}Nd and ^{165}Er. Some of these isotopes (^{55}Fe, ^{71}Ge, ^{131}Cs, ^{140}Nd, ^{165}Er) are of relevance for radiotherapy, while others (^{118}Te, ^{65}Zn) are interesting from a metrological point of view. We calculated all spectra on a basis of bound orbitals without explicitly including Auger-Meitner and fluorescence decay. To improve the accuracy of these calculations, future work could include the decay into unbound states and the coupling to the continuous spectrum of the electromagnetic field. For the case of Auger-Meitner decay the necessary formalism was developed in [11, 55], while chapter 4 of this work provides the setting for the description of fluorescence decay.

In chapter 3, we investigated the influence of hyperfine interaction on the nuclear decay by electron capture. For the example of charge neutral atomic ^{163}Ho, we demonstrated that a change of the initial hyperfine state leads to a shift of spectral weight on the Rydberg energy scale. Using a simple model, we were able to show that this surprising effect originates from selection rules related to the conservation of total angular momentum. In addition, we observed that a variation of the initial hyperfine state leads to a change of the isotope's lifetime on the per mille level. The calculations presented here constitute an extension of the studies on hydrogen- and heliumlike ions found in the literature [76, 77] to the case of charge neutral atoms. Furthermore, we considered a realistic experimental setup realizable in the ECHo experiment [28]. In this context, we included the non-spherical chemical environment as well as finite temperatures in the calculations. We could show that Boltzmann statistics determines the weight of a given

hyperfine state. Therefore, by comparing spectra measured at different temperatures, the influence of hyperfine interaction can be made visible. With a current detector resolution of < 10 eV [10], spectral differences induced by hyperfine interaction may already be visible. However, in order to see how these differences reveal under more realistic experimental conditions, Auger-Meitner decay to unbound states should be included in future calculations.

To accurately describe the differential decay rate requires to include Auger-Meitner decay into unbound states and the decay due to fluorescence. While the former is important at lower excitation energies, the latter becomes particularly relevant for the high-energy part of the spectrum. In chapter 4, we presented a description of the line-broadening due to fluorescence decay. Employing a self-energy formalism we showed that it is possible to efficiently include additional photons in the Hilbert space. For the example of electron capture decay in ^{55}Fe, we applied the derived formalism to describe the high-energy part of the spectrum. Compared to a constant Lorentzian broadening, an energy-dependent broadening described by the fluorescence self-energy leads to an increase of events by more than one order of magnitude at very high energies. This clearly demonstrates the relevance of an *ab initio* description of the spectral lineshape at these energies.

In addition, we calculated the second-order fluorescence yield spectrum, which provides information about the number of released photons following electron capture. We compared two calculations: First, a calculation employing an energy-independent Lorentzian line-broadening as well as an energy-independent light-matter interaction. Second, a calculation where these quantities were assumed to be energy-dependent. For the latter, our calculations predict a high-energy photon excess of more than one order of magnitude. This is in agreement with calculations based on the theory of Martin and Glauber [102, 103] and with experimental results [106]. While this frequently cited theory works on a mean-field level, we described the problem employing the full Coulomb interaction between the electrons. As we could show, this leads to additional multiplets in the fluorescence yield spectrum not resolved in theory of Martin and Glauber.

By means of the developed formalism it is possible to accurately predict the amount of ionizing radiation released in the decay. For example, this is important in the search for new radionuclides for cancer treatment, since their selection is often based on theoretical calculations [5]. In addition, a detailed knowledge of

the amount of ionizing radiation released in the decay is also crucial to calibrate liquid scintillation counting [96].

In a future work, it will be interesting to extend the derived approach to determine the electron yield spectrum, i.e. the number of electrons released following electron capture. This can be achieved by combining the derived equations describing the second-order decay process with the description of Auger-Meitner decay discussed in [11, 55].

The accurate description of nuclear decay rates requires a precise knowledge of the involved nuclear many-body wave functions. Within chapter 5 of this thesis, we were concerned with the optimization of the single-particle basis, the starting point of many *ab initio* nuclear many-body calculations. Although very promising, *ab initio* calculations are also quite challenging. As we have discussed, the choice of the single-particle basis is decisive for the computational performance of the many-body calculation and thus for the convergence behavior of the observables to be calculated. We presented a novel iterative scheme to determine an optimized set of single-particle states, which we referred to as *generalized* natural orbitals. Compared to ordinary natural orbitals, already used in nuclear structure calculations [112, 115, 118, 124], the proposed *generalized* natural orbitals promise to better reflect the true single-particle states. Hence, a calculation starting from these orbitals is expected to reduce the complexity of the many-body problem, which ultimately translates into a faster convergence. Therefore, *generalized* natural orbitals constitute a promising improvement to extend *ab initio* calculations to heavier nuclei than currently feasible. By directly implementing our proposed iterative scheme in a future work, it will be possible to test the performance of our method and to further investigate the implications for nuclear structure calculations.

In chapter 6, we considered inelastic x-ray scattering, a powerful tool to investigate the electronic structure of correlated many-electron systems. Depending on the energy of the incoming x-rays relative to an atomic edge, x-rays can scatter resonantly or nonresonantly off matter. Two established spectroscopic techniques, the Resonant Inelastic X-ray Scattering (RIXS) and the Nonresonant Inelastic X-ray Scattering (NIXS) were introduced. These techniques rely on the two terms of the (non-relativistic) light-matter interaction Hamiltonian, which are proportional to the vector potential and the vector potential squared, respec-

tively. As we demonstrated, both RIXS and NIXS are capable of probing so-called $d-d$ excitations, i.e. on-site transitions between crystal field split d-states. Motivated by experimental indications of a possible NIXS-RIXS interference for the case of $d-d$ excitations in Nickel oxide [135], we provided a theoretical analysis of the interference and focused on this example. Our results revealed that the type of interference, i.e. constructive or destructive, depends not only on the incoming photon energy with respect to an atomic edge, but also on the angle between the momentum of the incoming photons and the scattering vector. We could show that even several hundred electron volts away from an atomic edge, the NIXS-RIXS interference leads to prominent changes of the absolute and relative peak intensities. As typical NIXS experiments on transition-metal compounds are performed at photon energies several hundred electron volts away from an atomic edge [129–131], including the interference in theoretical calculations might lead to a better agreement with the experiment. Thus, it will be interesting to compare our calculations with experimental data to see if our predictions can explain the observed features in the Nickel oxide spectrum [135], which are presumably related to NIXS-RIXS interference.

A Appendix

A.1 Lanczos method

In this section, we introduce the Lanczos method [37]. In this work it is used to determine the ground state of a many-body problem described by a hermitean Hamiltonian H as well as to determine its dynamics subsequent to some perturbation. The basic idea of the Lanczos method is to iteratively construct a subspace of the full Hilbert space, the so-called Krylov space, on which the Hamiltonian is represented as a tri-diagonal matrix. Using an appropriate algorithm, this matrix is then easily diagonalized to obtain an approximate ground state. Below, we briefly outline the algorithm and show how it can be used to calculate response functions, closely following [38].

The algorithm

The first step in the Lanczos algorithm is to generate a normalized and typically random trial vector $|\phi_0\rangle$ which is included in the basis. To determine the many-body ground state, starting vector and true ground state must have a finite overlap. In the next step, the Hamiltonian acts on $|\phi_0\rangle$ thereby creating a new state

$$b_1|\phi_1\rangle = |\tilde{\phi}_1\rangle = H|\phi_0\rangle - a_0|\phi_0\rangle \tag{A.1}$$

where $a_0 := \langle\phi_0|H|\phi_0\rangle$ and $b_1^2 := \langle\tilde{\phi}_1|\tilde{\phi}_1\rangle$. By subtracting $a_0|\phi_0\rangle$ from the newly generated state $H|\phi_0\rangle$, it is assured that new state is orthogonal to $|\phi_0\rangle$, whereas b_1 takes into account the normalization. Thus, $|\phi_1\rangle$ denotes the properly orthonormalized state which is included in the Krylov basis. Similarly, the third state is constructed by acting with H on the previously generated state $|\phi_1\rangle$. This state is afterwards orthogonalized with respect to all previous basis states and normalized

$$b_2\,|\phi_2\rangle = |\tilde{\phi}_2\rangle = H\,|\phi_1\rangle - \sum_{i=0}^{1} |\phi_i\rangle\,\langle\phi_i|H|\phi_1\rangle = H\,|\phi_1\rangle - a_1\,|\phi_1\rangle - b_1\,|\phi_0\rangle \tag{A.2}$$

where $a_n := \langle \phi_n | H | \phi_n \rangle$ and $b_n^2 = \langle \tilde{\phi}_n | \tilde{\phi}_n \rangle$. The construction of further basis states works in the same way. For the $(n+1)$-st state we find

$$\begin{aligned} b_{n+1} |\phi_{n+1}\rangle = |\tilde{\phi}_{n+1}\rangle &= H |\phi_n\rangle - \sum_{i=0}^{n} |\phi_i\rangle \langle \phi_i | H | \phi_n \rangle \\ &= H |\phi_n\rangle - a_n |\phi_n\rangle - b_n |\phi_{n-1}\rangle . \end{aligned} \tag{A.3}$$

Note that due to orthogonality of the first n basis states, all terms except $a_n |\phi_n\rangle - b_n |\phi_{n-1}\rangle$ vanish in the orthogonalization of $|\phi_{n+1}\rangle$. In consequence, only $|\phi_n\rangle$ and $|\phi_{n\pm1}\rangle$ have non-vanishing overlap with $H |\phi_n\rangle$. After L iteration steps the Hamiltonian can be expressed on the $L+1$ dimensional Krylov space as

$$H_L = \begin{pmatrix} a_0 & b_1 & 0 & \dots & 0 & 0 \\ b_1 & a_1 & b_2 & \dots & 0 & 0 \\ 0 & b_2 & a_2 & \ddots & 0 & 0 \\ \vdots & \vdots & \ddots & \ddots & \ddots & \vdots \\ 0 & 0 & \dots & \ddots & a_{L-1} & b_L \\ 0 & 0 & \dots & 0 & b_L & a_L \end{pmatrix} . \tag{A.4}$$

If the number of iteration steps corresponds to $L = N - 1$ where N denotes the dimension of the underlying full Hilbert space, then the Lanczos method performs a unitary transformation of the original Hamiltonian. However, for most many-body problems the full Hilbert space is of extraordinary size and therefore computationally intractable. For this reason, one is usually restricted to the regime $L \ll N$. Using an appropriate second algorithm, the (approximate) ground state is obtained by diagonalization of H_L. Note that due to the typically small number of Krylov states compared to the dimension of the full space, the Lanczos method only gives a good approximation of the ground and the lowest lying states.

Response functions

The system's response to some perturbation T, for instance the weak interaction or in a core-level spectroscopic context the light-matter interaction, is described by the Green's function

$$G(z) = \langle \psi_0 | T^\dagger \frac{1}{z - H} T | \psi_0 \rangle \tag{A.5}$$

where $|\psi_0\rangle$ denotes the system's ground state obtained from a previous Lanczos run. To calculate $G(z)$, one can start the Lanczos routine as described above for

the normalized state $T|\psi_0\rangle$ and create in L iteration steps the tridiagonal Hamiltonian H_L. The spectrum is then determined by the resolvent of H_L projected on the normalized state $T|\psi_0\rangle$ which corresponds to the $[1,1]$ matrix element of the inverse of

$$z - H_L = \left(\begin{array}{c|ccccc} z-a_0 & -b_1 & 0 & \dots & 0 & 0 \\ \hline -b_1 & z-a_1 & -b_2 & \dots & 0 & 0 \\ 0 & -b_2 & z-a_2 & \ddots & 0 & 0 \\ \vdots & \vdots & \ddots & \ddots & \ddots & \vdots \\ 0 & 0 & \dots & \ddots & z-a_{L-1} & -b_L \\ 0 & 0 & \dots & 0 & -b_L & z-a_L \end{array}\right). \tag{A.6}$$

Rewriting this matrix in block-matrix form

$$z - H_L = \begin{pmatrix} z-a_0 & B^{(1)^T} \\ B^{(1)} & z - H_L^{(1)} \end{pmatrix}, \tag{A.7}$$

the Green's function can be written as

$$\begin{aligned} G(z) = \left[(z-H_L)^{-1}\right]_{1,1} &= \left(z - a_0 - B^{(1)^T}(z - H_L^{(1)})B^{(1)}\right)^{-1} \\ &= \left(z - a_0 - b_1^2\left[(z-H_L^{(1)})^{-1}\right]_{1,1}\right)^{-1}. \end{aligned} \tag{A.8}$$

As one can immediately see, the evaluation of this expression involves the inverse of $z - H_L^{(1)}$, i.e. the inversion of a sub-matrix of dimension $L-1$. Thus, we can proceed in the same way and obtain the inverse by partitioning this sub-matrix analogous to (A.7). This step is iteratively repeated for all other sub-matrices until we finally obtain the Green's function as a continued fraction

$$G(z) = \left[(z-H_L)^{-1}\right]_{1,1} = \cfrac{1}{z - a_0 - \cfrac{b_1^2}{z - a_1 - \cfrac{b_2^2}{z - a_2 - \dots}}}. \tag{A.9}$$

Block Lanczos

Of particular importance for the calculation of EC spectra is the block-variant of Lanczos' method, a generalization of the ordinary algorithm presented here. The basic idea is similar to the above description with the difference that the block-version starts from set of n orthonormal vectors $\mathbf{\Phi}_0 = \{|\phi_0^{(1)}\rangle, \dots, |\phi_0^{(n)}\rangle\}$. In consequence, the Hamiltonian is represented by a block-tri-diagonal matrix, i.e.

the diagonal and off-diagonal entries a_i and b_i in (A.4) are replaced by block-matrices A_i and B_i, whereas their dimension equals the length of the starting vector $\mathbf{\Phi}_0$. A more detailed description of the block-variant can be found in [55, 87].

A.2 Equivalence of the states $|F, M_F\rangle$ with identical F but different M_F

Given a state with definite F and maximal $F_z^{\max}$, all the other $2F$ states with identical F but different M_F can be constructed by repeated application of the lowering operator

$$F^-|F, M_F^{\max}\rangle = c_-(F, M_F)|F, M_F^{\max} - 1\rangle \tag{A.10}$$

where the prefactor is given by $c_- \equiv c_-(F, M_F) = \sqrt{(F - M_F + 1)\,(F + M_F)}$. $F^\pm$ represent the raising $(+)$ and lowering $(-)$ operators of the coupled total angular momentum F.

Let $G(\omega)$ to be defined by

$$G(\omega) \equiv \big\langle F, M_F \big| T^\dagger (z - H_{\mathrm{Dy}})^{-1} T \big| F, M_F \big\rangle \tag{A.11}$$

with $z := \omega + \mathrm{i}\frac{\gamma}{2} + E_{\mathrm{Ho}}$. In this case $G(\omega)$ corresponds up to the neutrino phase-space factor to the part of differential decay rate (3.25) with poles at positive energies. After lowering the M_F component by one, the spectrum for the new state $\big|F, M_F - 1\big\rangle$ is given by

$$\begin{aligned} G'(\omega) &= \big\langle F, M_F - 1 \big| T^\dagger (z - H_{\mathrm{Dy}})^{-1} T \big| F, M_F - 1 \big\rangle \\ &= \frac{1}{c_-^2} \big\langle F, M_F \big| F^+ T^\dagger (z - H_{\mathrm{Dy}})^{-1} T F^- \big| F, M_F \big\rangle. \end{aligned} \tag{A.12}$$

The transition operator T commutes with the squared total angular momentum, i.e. $[T, F^2] = 0$ and $[T, F^\pm] = 0$. Since the total angular momentum F is conserved, it follows that $[H_{\mathrm{Dy}}, F^2] = 0$ and $[H_{\mathrm{Dy}}, F^\pm] = 0$. Consequently, also resolvent and ladder operators commute, i.e. $[(z - H_{\mathrm{Dy}})^{-1}, F^\pm] = 0$, such that $G'(\omega)$ can be written as

$$\begin{aligned} G'(\omega) &= \frac{1}{c_-^2} \big\langle F, M_F \big| F^+ T^\dagger (z - H_{\mathrm{Dy}})^{-1} T F^- \big| F, M_F \big\rangle \\ &= \frac{1}{c_-^2} \big\langle F, M_F \big| T^\dagger F^+ (z - H_{\mathrm{Dy}})^{-1} F^- T \big| F, M_F \big\rangle \\ &= \frac{1}{c_-^2} \big\langle F, M_F \big| T^\dagger (z - H_{\mathrm{Dy}})^{-1} F^+ F^- T \big| F, M_F \big\rangle \\ &= \big\langle F, M_F \big| T^\dagger (z - H_{\mathrm{Dy}})^{-1} T \big| F, M_F \big\rangle \\ &= G(\omega) \end{aligned} \tag{A.13}$$

whereby it is used that $F^+ F^- \big| F, M_F \big\rangle = c_-^2$. From (A.13) we can infer that the spectra for $\big|F, M_F\big\rangle$ and $\big|F, M_F - 1\big\rangle$ are identical which holds for all pairs of states

differing in M_F by ± 1. In consequence, all spectra calculated for states with identical F but different M_F are equal and thus, only one spectrum per F needs to be calculated which in the case of ^{163}Ho leads to a reduction from 136 to 8 different spectra.

Bibliography

[1] M. F. L'annunziata. *Radioactivity: introduction and history, from the quantum to quarks*. Elsevier, 2016.

[2] A. H. Bécquerel. "Sur les radiations invisibles émises par les corps phosphorescents". In: *CR Acad. Sci. Paris* 122 (1896), p. 501.

[3] C. Grupen and M. Rodgers. *Radioactivity and Radiation*. Springer, 2016.

[4] P. Bernhardt et al. "Low-energy electron emitters for targeted radiotherapy of small tumours". In: *Acta Oncologica* 40.5 (2001), pp. 602–608.

[5] B. Q. Lee et al. "Atomic radiations in the decay of medical radioisotopes: a physics perspective". In: *Computational and mathematical methods in medicine* 2012 (2012).

[6] S. M. Bilenky and S. T. Petcov. "Massive neutrinos and neutrino oscillations". In: *Reviews of Modern Physics* 59.3 (1987), p. 671.

[7] C. Giunti and A. Studenikin. "Neutrino electromagnetic interactions: a window to new physics". In: *Reviews of Modern Physics* 87.2 (2015), p. 531.

[8] M. Aker et al. "First direct neutrino-mass measurement with sub-eV sensitivity". In: *arXiv preprint arXiv:2105.08533* (2021).

[9] M. Braß et al. "Ab initio calculation of the calorimetric electron-capture spectrum of ^{163}Ho: Intra-atomic decay into bound states". In: *Phys. Rev. C* 97 (2018), p. 054620.

[10] C. Velte et al. "High-resolution and low-background ^{163}Ho spectrum: interpretation of the resonance tails". In: *The European Physical Journal C* 79.12 (2019), pp. 1–8.

[11] M. Braß and M. W. Haverkort. "*Ab initio* calculation of the electron capture spectrum of ^{163}Ho: Auger–Meitner decay into continuum states". In: *New Journal of Physics* 22.9 (2020), p. 093018.

[12] L. Meitner. "Über die Entstehung der β-Strahl-Spektren radioaktiver Substanzen". In: *Zeitschrift für Physik* 9.1 (1922), pp. 131–144.

[13] P. Auger. "Sur les rayons β secondaires produits dans un gaz par des rayons X." In: *CR Acad. Sci.(F)* 177 (1923), p. 169.

[14] J. Chadwick. "Intensitätsverteilung im magnetischen Spectrum der β-Strahlen von radium B + C". In: *Verhandl. Dtsc. Phys. Ges.* 16 (1914), p. 383.

[15] C.S. Wu. "History of beta decay". In: *Beiträge zur Physik und Chemie des 20. Jahrhunderts*. Springer, 1959, pp. 45–65.

[16] E. Fermi. "Versuch einer Theorie der β-Strahlen. I". In: *Zeitschrift für Physik* 88.3 (1934), pp. 161–177.

[17] C. L. Cowan Jr et al. "Detection of the free neutrino: a confirmation". In: *Science* 124.3212 (1956), pp. 103–104.

[18] B. T. Cleveland et al. "Measurement of the solar electron neutrino flux with the Homestake chlorine detector". In: *The Astrophysical Journal* 496.1 (1998), p. 505.

[19] R. Davis Jr, D. S. Harmer, and K. C. Hoffman. "Search for neutrinos from the sun". In: *Physical Review Letters* 20.21 (1968), p. 1205.

[20] J. N. Abdurashitov et al. "Results from SAGE (The Russian-American gallium solar neutrino experiment)". In: *Physics Letters B* 328.1-2 (1994), pp. 234–248.

[21] W. Hampel et al. "GALLEX solar neutrino observations: Results for GALLEX IV". In: *Physics Letters B* 447.1-2 (1999), pp. 127–133.

[22] S. Fukuda et al. "The super-kamiokande detector". In: *Nuclear Instruments and Methods in Physics Research Section A: Accelerators, Spectrometers, Detectors and Associated Equipment* 501.2-3 (2003), pp. 418–462.

[23] Q. R. Ahmad et al. "Direct evidence for neutrino flavor transformation from neutral-current interactions in the Sudbury Neutrino Observatory". In: *Physical review letters* 89.1 (2002), p. 011301.

[24] B. Pontecorvo. "Neutrino experiments and the problem of conservation of leptonic charge". In: *Sov. Phys. JETP* 26.984-988 (1968), p. 165.

[25] S. Eliseev et al. "Direct measurement of the mass difference of ^{163}Ho and ^{163}Dy solves the Q-value puzzle for the neutrino mass determination". In: *Physical review letters* 115.6 (2015), p. 062501.

[26] A. de Rújula and M. Lusignoli. "Calorimetric measurements of ^{163}Holmium decay as tools to determine the electron neutrino mass". In: *Physics Letters B* 118.4-6 (1982), pp. 429–434.

[27] C. Enss et al. "Metallic magnetic calorimeters for particle detection". In: *Journal of low temperature physics* 121.3 (2000), pp. 137–176.

[28] L. Gastaldo et al. "The electron capture in ^{163}Ho experiment–ECHo". In: *The European Physical Journal Special Topics* 226.8 (2017), pp. 1623–1694.

[29] B Alpert et al. "Holmes". In: *The European Physical Journal C* 75.3 (2015), pp. 1–11.

[30] M. P. Croce et al. "Integration of radioactive material with microcalorimeter detectors". In: *Journal of Low Temperature Physics* 176.5 (2014), pp. 1009–1014.

[31] R. W. Howell. "Auger processes in the 21st century". In: *International journal of radiation biology* 84.12 (2008), pp. 959–975.

[32] A. Ku et al. "Auger electrons for cancer therapy–a review". In: *EJNMMI radiopharmacy and chemistry* 4.1 (2019), pp. 1–36.

[33] N. Gracheva et al. "^{165}Er: A new candidate for Auger electron therapy and its possible cyclotron production from natural holmium targets". In: *Applied Radiation and Isotopes* 159 (2020), p. 109079.

[34] V. A. Sanders and C. S. Cutler. "Radioarsenic: A promising theragnostic candidate for nuclear medicine". In: *Nuclear Medicine and Biology* 92 (2021), pp. 184–201.

[35] B. M. Bavelaar et al. "Subcellular targeting of theranostic radionuclides". In: *Frontiers in Pharmacology* 9 (2018), p. 996.

[36] A. L. Nichols, S. M. Qaim, and R. C. Noy. "Technical meeting on intermediate–term nuclear data needs for medical applications: cross sections and decay data". In: *Summary Report INDC (NDS)-0596, INDC International Nuclear Data Committee* (2011).

[37] C. Lanczos. "An iteration method for the solution of the eigenvalue problem of linear differential and integral operators". In: (1950).

[38] E. Koch. "Exact Diagonalization and Lanczos Method". In: *Many-Body-Methods for Real Materials Modeling and Simulation* (2019).

[39] J. J. Rehr et al. "Ab initio theory and calculations of X-ray spectra". In: *Comptes Rendus Physique* 10.6 (2009), pp. 548–559.

[40] M. W. Haverkort, M. Zwierzycki, and O. K. Andersen. "Multiplet ligand-field theory using Wannier orbitals". In: *Physical Review B* 85.16 (2012).

[41] E. Engel and R. M. Dreizler. "Density functional theory". In: *Theoretical and mathematical physics* (2011).

[42] W. Kohn and L. J. Sham. "Self-consistent equations including exchange and correlation effects". In: *Physical review* 140.4A (1965), A1133.

[43] P. Hohenberg and W. Kohn. "Inhomogeneous electron gas". In: *Physical review* 136.3B (1964), B864.

[44] F. Finocchi. "Density Functional Theory for Beginners: Basic Principles and Practical Approaches". In: *Institut des NanoSciences de Paris (INSP) CNRS and University Pierre et Marie Curie, Paris* (2011).

[45] W. Greiner. *Relativistic quantum mechanics*. Vol. 2. Springer.

[46] W. R. Johnson. *Atomic Structure Theory: Lectures on Atomic Physics*. Springer-Verlag Berlin Heidelberg, 2007.

[47] D. A. Varshalovich, A. N. Moskalev, and V. K. Khersonskii. *Quantum Theory of Angular Momentum*. World Scientific, Singapore, 1988.

[48] K. Koepernik and H. Eschrig. "Full-potential nonorthogonal local-orbital minimum-basis band-structure scheme". In: *Phys. Rev. B* 59 (1999).

[49] W. R. Johnson, K. T. Cheng, and M. H. Chen. "Accurate relativistic calculations including QED contributions for few-electron systems". In: *Theoretical and Computational Chemistry*. Vol. 14. Elsevier, 2004, pp. 120–187.

[50] R. D. Cowan. *The theory of atomic structure and spectra*. Univ. of California Press, 1981.

[51] M. W. Haverkort et al. "Bands, resonances, edge singularities and excitons in core level spectroscopy investigated within the dynamical mean-field theory". In: *EPL (Europhysics Letters)* 108.5 (2014).

[52] M. W. Haverkort. "Quanty for core level spectroscopy - excitons, resonances and band excitations in time and frequency domain". In: *Journal of Physics: Conference Series* 712 (2016).

[53] M. Thomson. *Modern particle physics*. Cambridge University Press, 2013.

[54] J. Engel and J. Menéndez. "Status and future of nuclear matrix elements for neutrinoless double-beta decay: a review". In: *Reports on Progress in Physics* 80.4 (2017), p. 046301.

[55] M. Braß. "Ab initio calculations of the electron capture spectrum in ^{163}Ho". PhD thesis. 2021.

[56] W. Bambynek et al. "Orbital electron capture by the nucleus". In: *Rev. Mod. Phys.* 49 (1977).

[57] A. De Rújula and M. Lusignoli. "The calorimetric spectrum of the electron-capture decay of ^{163}Ho. The spectral endpoint region". In: *Journal of High Energy Physics* 2016.5 (2016), pp. 1–26.

[58] A. Faessler et al. "Determination of the neutrino mass by electron capture in Ho 163 and the role of the three-hole states in Dy 163". In: *Physical Review C* 91.6 (2015), p. 064302.

[59] A. Faessler and F. Šimkovic. "Improved description of one-and two-hole excitations after electron capture in Ho 163 and the determination of the neutrino mass". In: *Physical Review C* 91.4 (2015), p. 045505.

[60] A. Faessler, L. Gastaldo, and F. Šimkovic. "Neutrino mass, electron capture, and the shake-off contributions". In: *Physical Review C* 95.4 (2017), p. 045502.

[61] R. G. H. Robertson. "Examination of the calorimetric spectrum to determine the neutrino mass in low-energy electron capture decay". In: *Physical Review C* 91.3 (2015), p. 035504.

[62] R. D. Mattuck. *A guide to Feynman diagrams in the many-body problem*. Courier Corporation, 1992.

[63] R. W. Howell. "Radiation spectra for Auger-electron emitting radionuclides: report No. 2 of AAPM nuclear medicine task group No. 6". In: *Medical physics* 19.6 (1992), pp. 1371–1383.

[64] P. M. Fredericia et al. "Cs-131 as an experimental tool for the investigation and quantification of the radiotoxicity of intracellular Auger decays in vitro". In: *International Journal of Radiation Biology* (2020), pp. 1–14.

[65] P. C.-O. Ranitzsch et al. "MetroMMC: Electron-capture spectrometry with cryogenic calorimeters for science and technology". In: *Journal of Low Temperature Physics* 199.1 (2020), pp. 441–450.

[66] S. Y. F. Chu, L. P. Ekström, and R. B. Firestone. *The Lund/LBNL nuclear data search*. `http://nucleardata.nuclear.lu.se/toi/index.asp`. Accessed: 2022-05-11.

[67] Brookhaven National Laboratory. *National Nuclear Data Center*. `https://www.nndc.bnl.gov/nudat3/`. Accessed: 2022-04-17.

[68] G. T. Emery. "Perturbation of nuclear decay rates". In: *Annual Review of Nuclear Science* 22.1 (1972), pp. 165–202.

[69] E. Segre and C. E. Wiegand. "Experiments on the Effect of Atomic Electrons on the Decay Constant of Be^7". In: *Physical Review* 75.1 (1949), p. 39.

[70] R. Daudel, M. Jean, and M. Lecoin. "Sur la possibilité d'existence d'un type particulier de radioactivité phénomène de création e". In: *Journal de Physique et le Radium* 8.8 (1947), pp. 238–243.

[71] A. Ray et al. "Observation of large change of ^{7}Be decay rate in Au and Al_2O_3 and its implications". In: *Physics Letters B* 455.1-4 (1999), pp. 69–76.

[72] T. Ohtsuki et al. "Enhanced Electron-Capture Decay Rate of ^{7}Be Encapsulated in C_{60} Cages". In: *Physical review letters* 93.11 (2004), p. 112501.

[73] T. Ohtsuki et al. "Radioactive Decay Speedup at T= 5 K: Electron-Capture Decay Rate of ^{7}Be Encapsulated in C_{60}". In: *Physical review letters* 98.25 (2007), p. 252501.

[74] E. V. Tkalya, A. V. Bibikov, and I. V. Bodrenko. "Electron capture β decay of ^{7}Be encapsulated in C_{60}: Origin of increased electron density at the ^{7}Be nucleus". In: *Physical Review C* 81.2 (2010), p. 024610.

[75] L. M. Folan and V. I. Tsifrinovich. "Effects of the hyperfine interaction on orbital electron capture". In: *Physical review letters* 74.4 (1995), p. 499.

[76] Yu. A. Litvinov et al. "Measurement of the β+ and Orbital Electron-Capture Decay Rates in Fully Ionized, Hydrogenlike, and Heliumlike ^{140}Pr Ions". In: *Physical review letters* 99.26 (2007), p. 262501.

[77] Z. Patyk et al. "Orbital electron capture decay of hydrogen-and helium-like ions". In: *Physical Review C* 77.1 (2008), p. 014306.

[78] G. K. Woodgate. *Elementary Atomic Structure*. Oxford University Press, USA, 1980.

[79] G. D. Alkhazov et al. "Nuclear deformation of holmium isotopes". In: *Nuclear Physics A* 504.3 (1989), pp. 549–561.

[80] E. Arimondo, M. Inguscio, and P. Violino. "Experimental determinations of the hyperfine structure in the alkali atoms". In: *Reviews of Modern Physics* 49.1 (1977), p. 31.

[81] B. Singh and A. R. Farhan. "Nuclear data sheets for A= 163". In: *Nuclear Data Sheets* 89.1 (2000), pp. 1–212.

[82] N. W. Ashcroft and N. D. Mermin. *Solid state physics*. Holt, Rinehart and Winston, 1976.

[83] D. Khomskii. *Transition metal compounds*. Cambridge University Press, 2014.

[84] R. Eder. "Multiplets in transition metal ions". In: *Correlated Electrons: From Models to Materials. Modeling and Simulation; Pavarini, E., Koch, E., Anders, F., Jarrell, M., Eds* (2012).

[85] B. R. Judd and I. Lindgren. "Theory of zeeman effect in the ground multiplets of rare-earth atoms". In: *Physical Review* 122.6 (1961), p. 1802.

[86] S. Lebègue et al. "Multiplet effects in the electronic structure of light rare-earth metals". In: *Physical Review B* 74.4 (2006), p. 045114.

[87] S. Heinze. "Materialspecific Simulations of manybody Electron Dynamics". PhD thesis. 2021.

[88] C. J. Ballhausen. *Ligand Field Theory*. McGraw-Hill, New York, 1962.

[89] J. Mulak and Z. Gajek. *The Effective Crystal Field Potential*. Elsevier, Amsterdam, 2000.

[90] K. W. H. Stevens. "Matrix elements and operator equivalents connected with the magnetic properties of rare earth ions". In: *Proceedings of the Physical Society. Section A* 65.3 (1952), p. 209.

[91] K. R. Lea, M. J. M. Leask, and W. P. Wolf. "The raising of angular momentum degeneracy of f-electron terms by cubic crystal fields". In: *Journal of Physics and Chemistry of Solids* 23.10 (1962), pp. 1381–1405.

[92] A. P. Murani. "Magnetic susceptibility and electrical resistivity of some gold-rare-earth alloys". In: *Journal of Physics C: Solid State Physics* 3.2S (1970), S153.

[93] B. Bleaney. "Lanthanide ions in metallic gold-II. Terbium and holmium". In: *Proceedings of the Royal Society of London. A. Mathematical and Physical Sciences* 424.1867 (1989), pp. 299–306.

[94] P. C.-O. Ranitzsch et al. "Characterization of the ^{163}Ho Electron Capture Spectrum: A Step Towards the Electron Neutrino Mass Determination". In: *Physical review letters* 119.12 (2017), p. 122501.

[95] M. O. Krause. "Atomic radiative and radiationless yields for K and L shells". In: *Journal of physical and chemical reference data* 8.2 (1979), pp. 307–327.

[96] R. Broda, P. Cassette, and K. Kossert. "Radionuclide metrology using liquid scintillation counting". In: *Metrologia* 44.4 (2007), S36.

[97] S. Mukamel. *Principles of Nonlinear Optical Spectroscopy*. Oxford University Press, 1995.

[98] U. Fano. "Effects of configuration interaction on intensities and phase shifts". In: *Physical Review* 124.6 (1961), p. 1866.

[99] K. R. Waters, J. Mobley, and J. G. Miller. "Causality-imposed (Kramers-Kronig) relationships between attenuation and dispersion". In: *IEEE transactions on ultrasonics, ferroelectrics, and frequency control* 52.5 (2005), pp. 822–823.

[100] W. Schülke. *Electron Dynamics by Inelastic X-ray Scattering*. Oxford University Press Inc., 2007.

[101] P. Morrison and L. I. Schiff. "Radiative K capture". In: *Physical Review* 58.1 (1940), p. 24.

[102] R. J. Glauber and P. C. Martin. "Radiative capture of orbital electrons". In: *Physical Review* 104.1 (1956), p. 158.

[103] P. C. Martin and R. J. Glauber. "Relativistic theory of radiative orbital electron capture". In: *Physical Review* 109.4 (1958), p. 1307.

[104] J. H. Scofield. "Relativistic Hartree-Slater values for K and L X-ray emission rates". In: *Atomic Data and Nuclear Data Tables* 14.2 (1974), pp. 121–137.

[105] J. H. Scofield. "Exchange corrections of *K* X-ray emission rates". In: *Physical Review A* 9.3 (1974).

[106] M. C. P. Isaac, V. R. Vanin, and O. A. M. Helene. "The Internal Bremsstrahlung following the Electron Capture decay of ^{55}Fe". In: *Zeitschrift für Physik A Atomic Nuclei* 335.3 (1990), pp. 243–246.

[107] S. Aberg, H. Flocard, and W. Nazarewicz. "Nuclear shapes in mean field theory". In: *Annual Review of Nuclear and Particle Science* 40.1 (1990), pp. 439–528.

[108] M. Bender, P.-H. Heenen, and P.-G. Reinhard. "Self-consistent mean-field models for nuclear structure". In: *Reviews of Modern Physics* 75.1 (2003), p. 121.

[109] P. Gysbers et al. "Discrepancy between experimental and theoretical β-decay rates resolved from first principles". In: *Nature Physics* 15.5 (2019), pp. 428–431.

[110] J. D. Vergados, H. Ejiri, and F. Šimkovic. "Theory of neutrinoless double-beta decay". In: *Reports on Progress in Physics* 75.10 (2012), p. 106301.

[111] T. D. Morris et al. "Structure of the lightest tin isotopes". In: *Physical review letters* 120.15 (2018), p. 152503.

[112] J. Hoppe et al. "Natural orbitals for many-body expansion methods". In: *Physical Review C* 103.1 (2021), p. 014321.

[113] P. Navrátil, J. P. Vary, and B. R. Barrett. "Large-basis ab initio no-core shell model and its application to 12 C". In: *Physical Review C* 62.5 (2000), p. 054311.

[114] B. R. Barrett, P. Navrátil, and J. P. Vary. "Ab initio no core shell model". In: *Progress in Particle and Nuclear Physics* 69 (2013), pp. 131–181.

[115] A. Tichai et al. "Natural orbitals for ab initio no-core shell model calculations". In: *Physical Review C* 99.3 (2019), p. 034321.

[116] J. Suhonen. *From nucleons to nucleus: concepts of microscopic nuclear theory*. Springer Science & Business Media, 2007.

[117] M. V. Stoitsov, W. Nazarewicz, and S. Pittel. "New discrete basis for nuclear structure studies". In: *Physical Review C* 58.4 (1998), p. 2092.

[118] P. Fasano et al. "Natural orbitals for the ab initio no-core configuration interaction approach". In: *arXiv preprint arXiv:2112.04027* (2021).

[119] P.-O. Löwdin. "Quantum theory of many-particle systems. I. Physical interpretations by means of density matrices, natural spin-orbitals, and convergence problems in the method of configurational interaction". In: *Physical Review* 97.6 (1955), p. 1474.

[120] P.-O. Löwdin and H. Shull. "Natural orbitals in the quantum theory of two-electron systems". In: *Physical Review* 101.6 (1956), p. 1730.

[121] E. R. Davidson. "Properties and uses of natural orbitals". In: *Reviews of Modern Physics* 44.3 (1972), p. 451.

[122] I. Lindgren, J. Lindgren, and A.-M. Mårtensson. "Many-body calculations of the hyperfine interaction of some excited states of alkali atoms, using approximate Brueckner or natural orbitals". In: *Zeitschrift für Physik A Atoms and Nuclei* 279.2 (1976), pp. 113–125.

[123] Y. Lu et al. "Efficient real-frequency solver for dynamical mean-field theory". In: *Phys. Rev. B* 90 (8 2014), p. 085102.

[124] C. Constantinou et al. "Natural orbital description of the halo nucleus ^{6}He". In: *Nuclear Science and Techniques* 28.12 (2017), p. 179.

[125] P. J. Hay. "On the calculation of natural orbitals by perturbation theory". In: *The Journal of Chemical Physics* 59.5 (1973), pp. 2468–2476.

[126] B. Fromme. *Dd excitations in transition-metal oxides: a spin-polarized electron energy-loss spectroscopy (SPEELS) study*. Vol. 170. Springer, 2007.

[127] M. Moretti Sala et al. "Energy and symmetry of dd excitations in undoped layered cuprates measured by Cu L_3 resonant inelastic x-ray scattering". In: *New Journal of Physics* 13.4 (2011), p. 043026.

[128] M. W. Haverkort et al. "Nonresonant Inelastic X-Ray Scattering Involving Excitonic Excitations: The Examples of NiO and CoO". In: *Phys. Rev. Lett.* 99 (25 2007).

[129] B. C. Larson et al. "Nonresonant Inelastic X-Ray Scattering and Energy-Resolved Wannier Function Investigation of $d-d$ Excitations in NiO and CoO". In: *Phys. Rev. Lett.* 99 (2007).

[130] N. Hiraoka et al. "dd excitations in three-dimensional q-space: A nonresonant inelastic X-ray scattering study on NiO". In: *EPL (Europhysics Letters)* 96.3 (2011).

[131] W. B. Wu et al. "Effective orbital symmetry of CuO: Examination by nonresonant inelastic x-ray scattering". In: *Physical Review B* 88.20 (2013).

[132] S. Huotari et al. "Crystal-field excitations in NiO studied with hard x-ray resonant inelastic x-ray scattering at the Ni K edge". In: *Phys. Rev. B* 78 (2008).

[133] M. van Veenendaal et al. “Observation of *dd* excitations in NiO and $NiCl_2$ using *K*-edge resonant inelastic x-ray scattering”. In: *Phys. Rev. B* 83 (2011).

[134] Y.-P. Sun et al. “Interference between resonant and nonresonant inelastic x-ray scattering”. In: *Physical review letters* 110.22 (2013).

[135] S. Huotari. Private Communication. 2022.

[136] M. Sundermann. “f-electron charge densities probed using core level nonresonant inelastic x-ray scattering”. In: *arXiv preprint arXiv:1911.06901* (2019).

[137] H. Yavaş et al. “Direct imaging of orbitals in quantum materials”. In: *Nature Physics* 15.6 (2019).

[138] M. Sundermann et al. “4f Crystal Field Ground State of the Strongly Correlated Topological Insulator SmB_6”. In: *Physical review letters* 120.1 (2018).

[139] M. W. Haverkort. “Theory of Resonant Inelastic X-Ray Scattering by Collective Magnetic Excitations”. In: *Phys. Rev. Lett.* 105 (2010).

[140] G. Ghiringhelli et al. “Low Energy Electronic Excitations in the Layered Cuprates Studied by Copper L_3 Resonant Inelastic X-Ray Scattering”. In: *Physical review letters* 92.11 (2004).

[141] H. Yavaş et al. “Observation of phonons with resonant inelastic x-ray scattering”. In: *Journal of Physics: Condensed Matter* 22.48 (2010).

[142] L. J. P. Ament et al. “Resonant inelastic x-ray scattering studies of elementary excitations”. In: *Rev. Mod. Phys.* 83 (2011).

[143] J. van den Brink and M. van Veenendaal. “Correlation functions measured by indirect resonant inelastic X-ray scattering”. In: *Europhysics Letters (EPL)* 73.1 (2006).

[144] M. W. Haverkort. Private Communication. 2022.

[145] J. L. Campbell and T. Papp. “Widths of the atomic K–N7 levels”. In: *Atomic Data and Nuclear Data Tables* 77.1 (2001), pp. 1–56.

Acknowledgments

Diese Arbeit wäre ohne die großartige Unterstützung vieler Kollegen, Freunde und meiner Familie nicht möglich gewesen.

Besonderer Dank gilt meinem Betreuer Prof. Dr. Maurits W. Haverkort. Lieber Maurits, ich möchte mich für die Unterstützung, sowie für die zahlreichen Anregungen und Diskussionen in den vergangenen Jahren ganz herzlich bedanken. Deine intuitive und anschauliche Herangehensweise an die kompliziertesten Probleme sind wirklich beeindruckend und haben mein physikalisches Denken stark geprägt.

Des Weiteren möchte ich mich bei Prof. Dr. Christian Enss für die Übernahme des Zweigutachtens bedanken.

Ein ganz besonderer Dank gebührt Martin Braß. Lieber Martin, ich danke dir für deine Geduld meine unzähligen Fragen zu beantworten und insbesondere für die Unterstützung in der letzten Phase dieser Arbeit. Die Zusammenarbeit mit dir in den letzten Jahren war nicht nur sehr lehrreich, sondern hat mir auch sehr viel Freude bereitet.

Bei Simon Heinze und Michelangelo Tagliavini bedanke ich mich für die zahlreichen Diskussionen über Physik, die Unterstützung bei Software-Problemen und euer immer offenes Ohr. Darüber hinaus bedanke ich mich bei Nadejda Bouldi für die Diskussionen über den fluoreszenten Zerfall. Danken möchte ich auch allen ehemaligen Kollegen mit denen ich im Laufe der Jahre zusammenarbeiten und eine sehr schöne gemeinsame Zeit bei der Arbeit verbringen durfte.

Für das sorgfältige Korrekturlesen meiner Arbeit möchte ich Martin Braß, Simon Heinze, Michelangelo Tagliavini, Clemens Fruböse und Clemens Vittmann danken. Außerdem möchte ich an dieser Stelle Richard Teske meinen Dank für die Unterstützung mit dem Layout aussprechen.

Ganz besonders möchte ich mich bei meinen Großeltern, meiner Schwester und meinen Eltern für ihre andauernde Unterstützung in den vergangenen Jahren bedanken. Ohne euch würde es diese Arbeit nicht geben.

Zu guter Letzt danke ich Carina Dura für ihr Verständnis, ihre bedingungslose Unterstützung und ihr Vertrauen in mich.